

UNIVERSITÀ DEGLI STUDI ROMA 2

Dipartimento di Fisica

Dottorato di Ricerca in Fisica - XVII Ciclo

Origin and Propagation of Cosmic Rays

Vladimir Zdravković

Coordinatore

prof. Piergiorgio Picozza

Tutore

dr. Aldo Morselli

November 2004

Contents

Acknowledgments	3
Introduction	4
1 The Density/Destiny of the Universe	7
1.1 Dark Matter and Cosmological Constant	7
1.2 Dark Matter Candidates	9
1.3 Large Scale Measurements: The Cosmic Microwave Background	11
1.4 Small Scale Structure Formation: Dark Matter Halo Models .	14
1.4.1 Halo Centers	15
1.5 Relic Density of Weakly Interacting Particles	16
2 Supersymmetry	20
2.1 Introduction	20
2.2 The Minimal Supersymmetric Standard Model	21
3 Origin and Propagation of Cosmic Rays in the Framework of the Standard Model	29
3.1 Introduction	29
3.2 Introduction to the Production of the Primary and the Secondary Nuclei and Its Importance	30
3.3 The Most Elementary Results From the Physics of Plasma . .	33
3.3.1 Plasma Physics of Propagation	33
3.3.2 Some of the Methods for the Theoretical Study of the Dynamic of Plasma	34
3.3.3 Convective Effects in the Case of the Infinite Electro- conductivity of Plasma	37
3.3.4 Elementary Hydrodynamical Theory of Waves Propagation in Plasma	39
3.3.5 Second Order Fermi Acceleration Mechanism	48

3.4	Short History of Propagation Models and Basic Assumptions	
	About the Propagation Processes	51
3.4.1	Full Propagation Equation	56
3.5	Heliospheric Modulation of the Local Interstellar Spectra . . .	58
3.5.1	Solar Wind and Solar Modulation	58
3.5.2	Force Field Approximation	61
3.6	Propagation of the Background Component of Cosmic Rays	
	in the Milky Way and Its Uncertainties	63
4	Component of the Antiproton Spectra Induced by the Neu-	
	tralino Annihilations	79
4.1	Parameters at The Weak Energy Scale	79
4.2	Clumpy Halo Models	80
4.3	Propagation of the Neutralino Induced Component	81
4.4	Some Examples of the Primary	
	Component of the Antiproton Flux	82
5	Detection of Cosmic Ray Spectra	84
5.1	Introduction	84
5.2	The Second Generation Experiments	85
5.2.1	The MASS Apparatus	87
5.2.2	The Tramp-SI Apparatus (TS93)	89
5.2.3	The CAPRICE Apparatus	90
5.2.4	The BESS Experiment	92
5.2.5	The AMS Experiment	92
5.3	The Present Experimental Situation and the Future Experiments	93
5.4	Future Experiments: BESS Polar Flights	93
5.5	Future Experiments: PAMELA	94
5.5.1	PAMELA Scientific Objectives	94
5.5.2	The PAMELA Telescope	96
5.6	The Detection of the Secondary Components of the Positron	
	and the Antiproton Fluxes by PAMELA	98
5.7	The Possibility of Disentanglement of the	
	Neutralino Induced Component of the	
	Antiproton Flux With PAMELA	104
5.7.1	Results	104
6	Conclusions	112

Acknowledgments

I own special thank to dr Aldo Morselli who guided and supported me with care during my research.

My collaborators and friends Andrea Lionetto and Alessandro Cesarini helped me a lot during my doctorate and this is the right occasion to express my deepest gratefulness to them.

Introduction

The scope of this thesis is twofold: the first part of it is dedicated to analysis of the uncertainties of propagation of cosmic rays in the Milky Way; in the second part are studied possibilities of detection of eventual neutralino induced component of the antiproton spectra in the framework of minimal supergravity theory.

From the experimental detection of cosmic rays, their origin and transport through the Galaxy was widely treated subject. For example, many important results in theoretical physics of plasma were induced by the studies of production mechanisms of cosmic rays. A lot of subjects in experimental and theoretical nuclear physics are playing important role in cosmic rays propagation, also. The accuracy of nuclear physics knowledge is emphasized recently thanks to the studies of cosmic rays propagation. On the other side, just with the progress in computer science it was possible to check models for the dynamic of cosmic rays in the Galactic medium.

One could think that with the development of mentioned aspects of "standard physics" and computers it could be possible to explain the measured cosmic rays spectra. That is still not done, at least for all the cosmic rays spectra together in the framework of the same propagation model. The reasons are numerous. The first reason is that except nothing else but measurement of cosmic rays spectra there are no almost any other probes for magnetohydrodynamical parameters of the Galaxy that determine the propagation. Also, it is not sure how primary nuclei are formed. This emphasizes the importance of the future experiments for the measurement of cosmic rays spectra and distribution of supernovae and neutron stars as possible sources of primary cosmic rays, as well as the importance of the development of theory and simulations of generation of primaries by those objects. The most important reason is probably that we still do not know much about energy-matter content of the Universe. In fact, recent measurements of the Cosmic microwave background are strongly suggesting that Universe is euclidean, its density is equal to critical one, $\Omega \approx 1$; cosmological constant (**dark energy**) contribution is $\Omega_\Lambda \approx 0.7$, **dark matter** contribution is $\Omega_{DM} \approx 0.3$, barionic

matter part is of the order of just less than 5% and other contributions to the energy-mass density with respect to the critical mass due to photons ($400\frac{\gamma}{cm^3}$) and neutrinos ($\Omega_\nu \approx 0.001$) are negligible. Clearly, the presence of dark matter could influence the mechanisms of production and propagation of cosmic rays. One of the most important problems in today's theoretical as well as experimental physics is to understand the nature of dark matter and cosmological constant, with an intension to prove that the main dark component of galactic halos are exactly candidates suggested by supersymmetric theories.

To be able to make a statement, as example, like this one: "this part of the antiproton spectra is due to the Standard Model production, and that part is due to some other mechanism" or to give some bounds for some of the unknown parameters in the framework of the anyone of the new physical theories, first we should know the accuracy of standard calculations. In the case of antiprotons and supersymmetric candidate for dark matter we try to consider both of this problems. For the other species of cosmic rays we treated just the uncertainty of standard production, planning to do the complete analysis for the most important of them – positrons.

The plan of the thesis is the following:

In the first chapter is introduced the problem of dark matter and cosmological constant. The introduction is based on the standard arguments as measurements of the Galactic rotational curves and recent measurements Cosmic microwave background. There are also explained some of the models for the distribution of dark matter in our Galaxy that will be used in their more sophisticated variant in the fourth and sixth chapter, and will play important role for the analysis of the detectability of the eventual neutralino induced component of the antiproton spectra.

The Chapter 2 is entirely dedicated to supersymmetric theories in which framework it is found the candidate for dark matter in research on which this thesis is based – the lightest neutralino.

In Chapter 3 is treated the question of standard mechanisms of production and propagation of cosmic rays (background contribution). In the same chapter are presented the thesis results about the uncertainties of standard propagation due to the unknown geometrical and hydromagnetodynamical parameters of the Galaxy, uncertainties in measurements and parametrizations of nuclear cross sections and uncertainty of the helium to hydrogen ratio in the Galaxy.

In Chapter 4 is described creation and propagation of eventual neutralino induced component (signal contribution) and are given some examples of total spectra in comparison with existing experimental data.

Chapter 5 is dedicated to characteristics of PAMELA future experiment

for measurement of cosmic rays spectra and detection of theoretically predicted spectra from the previous chapters with this experiment. In this chapter is also given a review of previous experiments for the measurements of various cosmic rays spectra, from which experimental data are taken for the analysis done in the next chapter.

In Chapter 6 are presented results about possibility to disentangle the eventual signal component of the antiproton spectra. It is done in a clumpy halo scenario, and what was found finally are minimal values of clumpiness factors necessary to disentangle the signal from the background without violating the quality of fit of the existing data for antiproton spectra.

Chapter 7 contains brief review of the results with conclusions. One of the most important conclusions of this thesis is that, simply said, even for the diffusion and convection background models, that are already fitting the data good, PAMELA will be able to disentangle the eventual supersymmetric signal – and – to do so even for the small clumpiness factors.

Chapter 1

The Density/Destiny of the Universe

1.1 Dark Matter and Cosmological Constant

Here it will be given a very short introduction of a well known facts about standard cosmology models, as well as a brief review of recent measurement of the cosmological parameters. The presentation is based on standard literature, like the books of Weinberg [89] and Kolb and Turner [96], where interested reader can find all the details.

Cosmology studies the evolution of homogeneous medium of galaxies at the large scale of the Universe, taking into account the only one effective force at this scale – the force of gravity, supposing the exactness of Einstein Theory of General Relativity.

The Friedmann model describes the observed expanding Universe (see, for example, [89]), determined by the Hubble constant, $H_0 \approx 70 \frac{Km}{sMpc}$ [88]: the static Cosmos is impossible; but, there are three families of solutions – forever expanding, critical Universe and recollapsing one. In our, critical Universe (at least according to recent set of measurements of the Cosmic microwave background, as we will see soon), the kinetic energy of the expansion should be approximately equal to the gravitational energy of the Universe, or, its density should be equal to the critical one. The curvature is zero (parallel light rays will remain parallel). In the case of density bigger than the critical, expansion is infinite. The curvature is positive (parallel light rays will converge). The case of the Universe density smaller than the critical corresponds to the decelerating expansion followed by the collapse. The curvature is negative (parallel light rays will diverge).

Without entering in details about the Friedmann-Robertson-Waker met-

ric, first, we will estimate the critical density of the Universe using the Birkhoff theorem of the Theory of General Relativity and experimental facts about the expansion of the Universe (and principle of its homogeneity and isotropy, of course). A galaxy at distance r from the origin of the considered sphere of the same radius, filled with mass M , according to Hubble measurements, is moving with speed $H_0 r$ from the origin. So, the critical Universe is defined by the equation

$$\frac{1}{2}mv^2 = G\frac{Mm}{r}. \quad (1.1)$$

Using the critical density ρ_c and the fact of the expansion we have

$$\frac{1}{2}mH_0^2 r^2 = G\frac{\frac{4}{3}\pi\rho_c m}{r}. \quad (1.2)$$

So, critical density is

$$\rho_c = \frac{3H_0^2}{8\pi G} = 1.88 \cdot 10^{-26} h^2 \frac{Kg}{m^3}, \quad (1.3)$$

where it is useful to introduce the constant

$$h = \frac{H_0}{100 \frac{km}{sMpc}}. \quad (1.4)$$

Up to now, detected luminous (barionic) matter presents just

$$\Omega_b = \frac{\rho_{barionic}}{\rho_{critical}} < 5\%$$

of the critical density of the Universe [97], that is not negligible, but it is far from sufficient. From the theoretical point of view, Big Bang nucleosynthesis is giving the barion contribution to the total matter density of

$$0.02 < \Omega_b < 0.08,$$

see, for example [94].

This mass is not sufficient to explain the rotational curves of the galaxies. The needed mass of unknown not luminous matter is at least 20%, more preciously

$$0.2 < \Omega_{DM} < 0.3.$$

In figure 1.1, left panel, are presented few optical and radio rotational curves. All of them are showing liner rise of the rotational velocity in the centers of galaxies. This could be explained by the contribution due to the luminous galactic disk mass just up to $\approx 1Kpc$, for the typical spiral galaxy presented at 1.1, right panel. Those kinds of rotational curves have the sharp maximum and velocity is decreasing to a value of approximately $50\frac{Km}{s}$. Gas mass contribution to rotational curves are constantly rising, but they are small, and they don't pass the value of $\approx 30\frac{Km}{s}$!

To fill the gap, an extra amount of matter is needed. This is not the unique condition that unknown matter should satisfy. Indeed, it has to explain as well cosmological structure formation. For the more detailed discussions and further sources of references about barionic contribution to the Universe density, as well as many other similar questions, see, for example, [70].

1.2 Dark Matter Candidates

What dark matter is made of and what constraints should satisfy? The question of the nature of cosmological constant (if it is a constant, not a consequence of some unknown dynamic, see, for example [71], or some of the new results in string theory) we will not discuss in this thesis. Numerous particles were proposed, in the frameworks of various models, as candidates to fill the gap between the value of Ω_b and $\Omega_m = \Omega_b + \Omega_{DM}$ (see, for example, the discussions in [87] and [70]). Here, we will mention just the most common ideas.

The first candidate was, so called, hot dark matter. This because approximately one year after the Big Bang, when the horizon first encompassed the amount of matter in a large galaxy like Milky Way and the temperature was about 1KeV, neutrinos with masses in the eV range would have been highly relativistic. First, it was taught that electron neutrinos has the mass of about 20eV (experiments in Moscow), that was used to construct the hot dark matter theory with Ze'dovich spectrum of adiabatic primordial fluctuations

$$P_p(k) = Ak^n, \quad n = 1, \quad (1.5)$$

where k is the wavenumber. But, after the more precise experiments it was found that, in fact, the mass of electron neutrino has just the upper bound of $m_\nu < 3eV$. This changed the predictions of hot dark matter with Ze'dovich spectra to be completely inconsistent with the observed Universe.

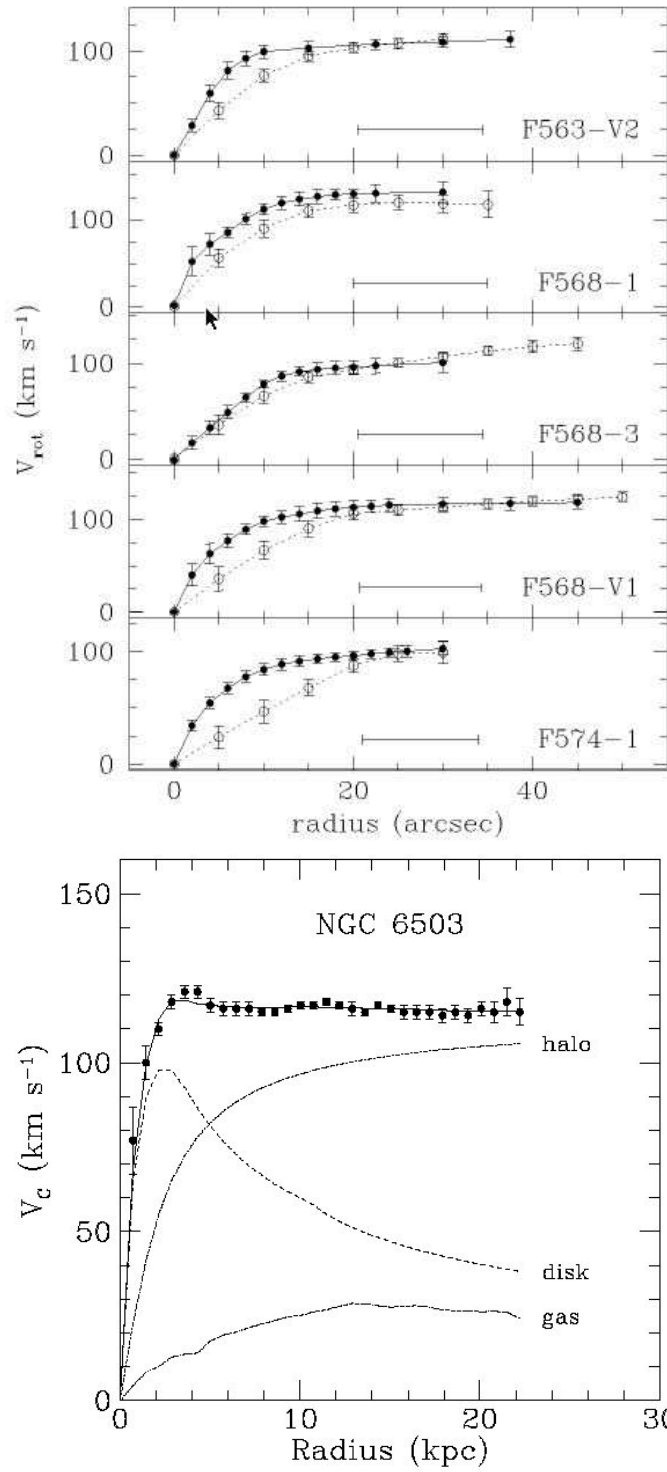


Figure 1.1: Figures are taken from [95] and [18].

As hot dark matter did not make success, the theory of cold dark matter was proposed [69, 68]. It is called "cold" because:

1) the dark matter particles are weakly interacting massive particles (WIMPs) among themselves and with other particles. This possibility will be treated extensively in this thesis later.

2) or because the dark matter particles thermal velocities were negligible in the early Universe,

3) or because, as in the case of axions, the dark matter particles are produced without a thermal distribution of velocities. Axions are dark matter candidates with the smallest mass of all. Their mass is of order $10^{-5}eV$. This subject is very large and has a long history. Interested reader can find more details in [91], for example, and references therein. (The biggest mass candidates are black holes.)

All of the mentioned ideas are taken seriously, not just from the theoretical point of view, but there are already also experiments for the examination of the parameter spaces for those theories. For axions see [92]; their detection is based on a particularly interesting effect of the resonant conversion of photons in a strong magnetic field. Possible detection (depending of the position in the parameter space of the theory) of WIMPs in the framework of supersymmetric theories (the lightest neutralino) with the future experiments is one of the subjects of this thesis (see the last chapter).

The most important variant of cold dark matter theory contains the cosmological constant separately, so this constant remains the problem, however. Cold dark matter seems to be in a good agreement with the data obtained by the observations on large scales of the Universe: the Cosmic microwave background measurements; as well as with smaller scales: dark matter halos and numbers of small satellites.

1.3 Large Scale Measurements: The Cosmic Microwave Background

To decide about the geometry of the Universe (is it euclidean or with positive or negative curvature), and consequently the density and all the Ω -s and Λ , we need a standard ruler on large scales to be able to measure angles and compare them with the results from differential geometry. For $\Omega > 1$ we will have larger angles (as on a sphere), while for $\Omega < 1$ the angles we expect are smaller (converging of light rays).

If we look enough far away – we will see the epoch when the Universe was

approximately as hot as the surface of the Sun! Plasma is opaque to light, and we can not see earlier periods. Due to the expansion of the Universe, the light that is coming from there is red shifted, and we see it as the Cosmic microwave background, detected as 2.73 K blackbody radiation. The end of the plasma era was when the temperature decreased below approximately 3000K. The Universe was 50000 times younger, 1000 times hotter and 10^9 times denser than today, at red shift 1000. The ionized Universe become transparent to light (recombination in plasma). After recombination, photons pressure become unimportant, and perturbations of the density could grow creating the structures that we see today.

Photon density fluctuations are affecting the matter density fluctuations $\frac{\Delta\rho}{\rho}$ (see [90] and references therein). Gravitational red shift of photons scattered in an overdensity or an underdensity with gravitational potential difference ϕ and Doppler effect produced by the proper motion with velocity \vec{v} of the electrons scattering the Cosmic microwave background photons are also influencing the picture of temperature fluctuations

$$\frac{\Delta T}{T} = \frac{\Delta T}{T}(\frac{\Delta\rho}{\rho}, \phi, \vec{v})$$

that we see today in the measured Cosmic microwave background picture. So, by measuring the Cosmic microwave background temperature fluctuations we are seeing, as it can be expected, the density fluctuations at recombination.

The velocity of sound in plasma before recombination (it was around $\frac{c}{3^{\frac{1}{2}}}$) is defining the characteristic scale in the Cosmic microwave background anisotropy at recombination by acoustic horizon at recombination that is defined by the distance that sound can travel since the Big Bang. Density perturbations start to oscillate when the acoustic horizon encompasses them. As long as they are larger than the acoustic horizon, they just follow the expansion without oscillating. The opposite edges of the perturbation start to oscillate when the acoustic horizon becomes larger than the density fluctuation. So, the size of the acoustic horizon at recombination separates perturbations that never start to oscillate from those that already started to oscillate. The density fluctuations that started to oscillate before the recombination so that will have time to fully compress will be seen as hotter domains. The dimensions of such a objects are of about $3 \cdot 10^5$ light years as the age of the Universe at recombination was of an order of $3 \cdot 10^5$ years. Density perturbations slightly larger or slightly smaller than those will not be fully compressed or fully rarefied, and will not be seen as coldest or hottest domains in the image of the Cosmic microwave background.

Now, having the standard ruler at the recombination and large distance between the recombination and us (order of the age of the Universe, $15 \cdot 10^9$ light years), we can say:

1) If the size of the characteristic domains in the temperature fluctuations corresponds to angles of about $\theta \approx \frac{10^3 \cdot 3 \cdot 10^5}{15 \cdot 10^9} \text{rad} \approx 1^0$ – we are living in euclidean Universe,

2) if we see them larger than one degree – we are in the Universe of the positive curvature ($\Omega > 1$),

3) if they are smaller – $\Omega < 1$, we will collapse together with the Universe.

The angular power spectrum

$$c_l = \langle |a_{l,m}|^2 \rangle$$

for the angular image of the Cosmic microwave background

$$\Delta T(\alpha, \delta) = \sum_{l,m} a_{l,m} Y_m^l(\alpha, \delta)$$

is computed for the results of various experiments. A peak at multipoles corresponding to an angular scale of an order of

$$1^0 \quad \text{i.e. for} \quad l \approx \frac{\pi}{\theta} \approx 200$$

was found. The position of the first peak l_{peak} is a function of Ω but also of Ω_m [81, 82, 83] so, that, for example for WMAP satellite data [72] are giving:

$$\begin{aligned} \Omega &= 1.03 \pm 0.02, \\ \Omega_m h^2 &= 0.135^{+0.008}_{-0.009}. \end{aligned}$$

For example, BOOMERanG [73] experiment is giving for the first peak:

$$l_1 = 213^{+10}_{-13}.$$

To find barionic, and consequently dark matter contribution, one need to include higher peaks [84]. For WMAP:

$$\Omega_b h^2 = 0.0224 \pm 0.0009.$$

There are also other measurements that confirm those results, see the review [87], for example, and references therein. This is one of the most important points: dark matter **has to be** made mainly of non-barionic matter!

But, this is not all that can be extracted from the measurements of the anisotropy of the Cosmic microwave background. Maybe hot dark matter theories were wrong, but nearly Ze'ldovich spectrum of adiabatic primordial fluctuations remained. This can be seen (see [84] for a recent review) by the analysis of the other peaks in the spectrum: from the ratio amplitudes of the peaks can be extracted the average density of barions in the Universe, Ω_b , as well as the exponent of the initial power spectrum of the density fluctuations, parametrized in a Ze'ldovich manner $P_p(k) = Ak^n$. For n , for example BOOMERanG, is giving

$$n = 0.96_{-0.09}^{+0.10}.$$

This is very important result as it is showing that the theory of Cosmic inflation in the very early Universe, that gives for the primordial density fluctuations Ze'ldovich spectrum with $n = 1$, should be correct. The problem of the nature of dark matter and the cosmological constant remains open, even if many candidates for dark matter exist and string cosmology is trying to resolve the problem of the cosmological constant. Cosmic inflation theory is solving also many other paradoxes as the flatness paradox and the paradox of horizons, or paradox of magnetic monopoles, see [96], for example.

Here we will just mention the fundamental idea of inflation theories, to be selfconsistent. It is introduced a, so called, inflaton scalar field, ϕ , with a potential, $V(\phi)$, that couples with gravity through energyimpulse tensor defined by the kinetic equation

$$p = -\rho, \tag{1.6}$$

where p and ρ are pressure and density of the scalar field. For the inflaton field is valid, so called, slow-roll condition that imply that potential $V(\phi)$ must be quasi-flat in relatively big domain. This model is giving the exponential expansion of the Cosmological scale factor in the Friedmann-Robertson-Walker metric.

1.4 Small Scale Structure Formation: Dark Matter Halo Models

Many authors were trying to find the best functional type to parametrize the dark matter halo, in order to reproduce the rotational curves of galaxies.

But, this can not be done without explaining why the halo of, say cold dark matter, should look like that? So, the dark matter candidate should cluster in the exactly that functional type of halo density.

It matters, as we see already that the main part of dark matter can not be barionic. But, to choose between the other dark matter candidates is the possibility of dark matter candidate to explain the clustering at the galaxy scale, at the first place, but also some other requirements.

For example, the galaxy clustering condition is not satisfied by hot dark matter [17, 96]; even in a very exotic extension of the Standard Model, where via the see-saw mechanism (see [15]) can be obtained a neutrino state of a big mass (for allowed mass range see [16]).

Cold dark matter with Cosmological constant explains this. Also many other observed phenomena as the distributions of stars in big and small galaxies, formation of groups and clusters of galaxies and the spatial distribution of galaxies, even with respect to internal rotational velocities could be explained quite well by cold dark matter.

1.4.1 Halo Centers

From the early 1990s it was already possible to simulate with a required accuracy cold dark matter galactic halos, so that the first results where showing

$$\rho_{halo} \propto \frac{1}{r^\alpha}, \quad (1.7)$$

with $\alpha \approx 1$, i.e. spherically symmetric distribution of cold dark matter in the halo. This was not in agreement with the differential rotation laws of galaxies, and also cold dark matter was in crisis. But, Navarro, Frenk and White found the new density profile of cold dark matter that was fitting good formed halos

$$\rho_{NFW} \propto \frac{1}{r} \frac{1}{(r + r_s)^2}, \quad (1.8)$$

and that was explaining very good the dynamic of the matter in the typical galaxy [135]. The only uncertain regions are the very galactic centers $- 0Kpc < r < 1Kpc$.

At the same time Moor's group proposed an alternative [6]

$$\rho_M \propto \frac{1}{r^{\frac{3}{2}}} \frac{1}{(r + r_M)^{\frac{3}{2}}}, \quad (1.9)$$

that is almost indistinguishable from ρ_{NFW} unless galaxies are probed at scales smaller than 1Kpc, which is difficult, even sometimes possible.

Optical rotational curves rise faster than radio curves (see figure 1.1) and this is more consistent with Navarro-Frenk-White density profile.

Some alternatives for dark matter are also, so called, warm dark matter and self-interacting dark matter (see [12], for example) but they are probably excluded from some theoretical reasons and also with the numerical studies of the number of small satellite galaxies (see [87] and references therein).

A small part of dark matter could be also barionic, or, generally speaking, not massive particles that interact weakly (WIMP). Examples are, the most important – black holes, that could evaporate and give a component in the antiparticles cosmic rays spectra, brown dwarfs of masses from approximately $1mM_{\odot}$ up to a Solar mass, in which did not start the nuclear fusion processes, than white dwarfs and neutron stars; there were also ideas of hydrogen composed halos, better to say parts of halos...

1.5 Relic Density of Weakly Interacting Particles

As we just saw that non barionic matter is forced as a dark matter candidate by the measurements of anisotropy of the Cosmic microwave background, now we will give an estimation of the relic cosmological abundance of these particles. Also, we will give one more reason, except their natural occurrence in the supersymmetric theories, why weakly interacting particles are privileged as a dark matter candidates.

Those particles were in thermal equilibrium and in a great quantity in the early phase of the Universe expansion, when the temperature was $T \gg m_{\chi}$, where $T = T(t)$ is the temperature of the Universe at a time t and m_{χ} is the WIMP mass ([70] and reference therein). The equilibrium abundance is maintained by annihilations of particles with their antiparticles $\bar{\chi}$ into a lighter couples of particle-antiparticle $l\bar{l}$, $\chi\bar{\chi} \rightarrow l\bar{l}$ (direct process; indirect process is $l\bar{l} \rightarrow \chi\bar{\chi}$).

In SUSY theories χ is a Majorana particle, so $\chi = \bar{\chi}$. As the Universe cools to the temperatures $T \ll m_{\chi}$ the equilibrium abundance drops exponentially until the rate of annihilation falls below the expansion rate of the Universe H . The interactions which maintains the thermal equilibrium don't work anymore, and the relic abundance remains constant (this is called freeze-in). In thermal equilibrium the number density of the χ particle is given by

$$n_{\chi}^{eq} = \frac{g}{(2\pi)^3} \int f(p) d^3p \quad (1.10)$$

where g is the number of degrees of freedom of the particle and $f(p)$ is Fermi-Dirac or Einstein-Bose distribution. For regimes of high and low temperatures

$$\begin{aligned} n_\chi^{eq} &\propto T^3 && \text{for } T \gg m_\chi \\ n_\chi^{eq} &\sim g \left(\frac{m_\chi T}{2\pi} \right)^{3/2} \exp\left(\frac{-m_\chi}{T} \right) && \text{for } T \ll m_\chi \end{aligned} \quad (1.11)$$

where in the last case we can see their density is Boltzmann suppressed. If the expansion of the Universe were so slow to maintain thermal equilibrium, the number of WIMPs today would be exponentially suppressed. In this case we would not have WIMPs at all. However we remind that the Universe is not static and so the thermodynamic equilibrium cannot be ensured during the whole evolution. In fact, at high temperatures, *i.e.* $T \gg m_\chi$, the χ particles are present with a great abundance and the annihilation process into lighter particles, as well the inverse process, goes on quickly. But when $T < m_\chi$ the number density n_χ^{eq} drops exponentially. The annihilation rate is

$$\Gamma = n_\chi \langle \sigma_{ann} v \rangle \quad (1.12)$$

where $\langle \sigma_{ann} v \rangle$ is the thermally averaged total annihilation cross section of $\chi\bar{\chi}$ into lighter particles times the relative velocity v . When Γ drops below the expansion rate $\Gamma \lesssim H$ there is a freeze-out condition for the WIMPs. In fact, the annihilation time scale given by Γ is less than the Hubble constant H , *i.e.* the time scale for the Universe expansion.

The simple scenario we have presented, can be quantitatively encoded into the Boltzmann equation, which describes the time evolution of the number density $n_\chi(t)$ of a generic WIMP

$$\frac{dn_\chi}{dt} + 3Hn_\chi = - \langle \sigma_{ann} v \rangle \left[(n_\chi)^2 - (n_\chi^{eq})^2 \right] \quad (1.13)$$

where H and $a = a(t)$ are, respectively, the Hubble constant and the scale factor. The second term on the left side of this equation accounts for the expansion of the Universe, being proportional to H . If there are no interactions that change the WIMP number, the right side is zero, and we recover the previous result where $n_\chi \propto a^{-3}$ (in this regime there are roughly as many χ particles as photons and $a \propto T^{-1}$ in the radiation dominated era). The two terms in brackets on the RHS of equation account for annihilation and creation of WIMPs in the direct and indirect channel. At the equilibrium this term is zero. The equation 1.13 describes both Dirac particles as well

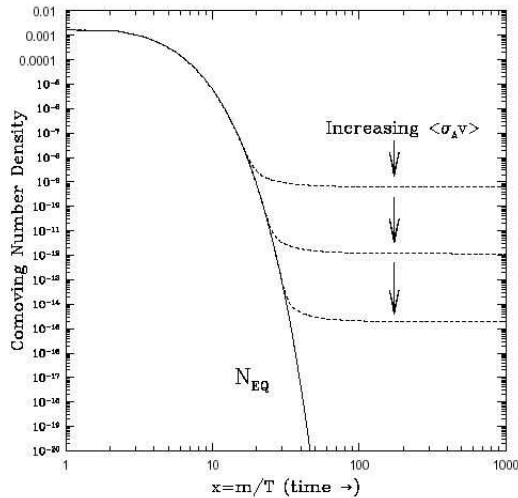


Figure 1.2: Comoving number density of a WIMP as a function of $x = m_\chi/T$. The dashed curve are the actual abundances for different thermal averaged annihilation cross sections while the solid curve is the equilibrium abundance [96].

as Majorana particles which are self annihilating, because, in this case, $\chi = \bar{\chi}$. However the two cases are distinct, because for Majorana particles, the annihilation rate is:

$$\frac{n_\chi^2}{2} \langle \sigma_{ann} v \rangle$$

In each annihilation two particles are involved, and so this cancels the factor 2 in the annihilation rate. For Dirac particles which have no particle-antiparticle asymmetry, $n_\chi = n_{\bar{\chi}}$, the Boltzmann equation 1.13 still holds. In this case the total number of particles plus antiparticle is now $2n_\chi$. In the case of particle-antiparticle asymmetry, the relic abundance is generally given by this asymmetry [85]. A typical example is given by the relic proton density that is essentially fixed by the proton-antiproton asymmetry, *i.e.* the baryon number of the Universe.

There is no known closed form solution for the Boltzmann equation, but it is possible to find an approximate solution for the case in which $\langle \sigma_{ann} v \rangle$ is weakly energy dependent. In this case the WIMP relic abundance is given by [70]

$$\Omega_\chi h^2 = \frac{m_\chi n_\chi}{\rho_c} \sim \left(\frac{3 \cdot 10^{-27} \text{ cm}^3 \text{ s}^{-1}}{\langle \sigma_{ann} v \rangle} \right) \quad (1.14)$$

There is no dependence from the WIMP mass, modulo logarithmic corrections, and it is inversely proportional to the annihilation cross section.

We show some examples of numerical solution of the Boltzmann equation in figure 1.2. The number density functions per comoving volume (dashed lines) are functions of $x \equiv m_\chi/T$ increasing with Cosmic time. The relation 1.14 shows that if a stable new particle exists with a weak scale interaction, *i.e.* with an annihilation cross section of the order of

$$\langle \sigma_{ann} v \rangle \sim 10^{-25} \text{ cm}^3 \text{ s}^{-1}, \quad (1.15)$$

then it will account for the right order of magnitude for the relic abundance. This is a quite interesting result because there is no a priori reason for the weak scale interaction to have something in common with the relic abundance, that is a Cosmological parameter. Hence, the most motivated candidate for the dark matter is a stable particle associated with new physics at the electroweak scale.

Chapter 2

Supersymmetry

2.1 Introduction

We saw in previous chapter that the most of the dark matter has to be non barionic; and that the most promising candidate for it are weakly interacting massive particles (framework of cold dark matter). Among them, the lightest supersymmetric particle – the lightest neutralino – is the best motivated candidate from the theoretical point of view. Supersymmetry naturally extends Standard Model (based on $SU(3) \otimes SU(2) \otimes U(1)$) of electroweak and strong hadron interactions above energy scale of order $E \approx 1TeV$, currently reached in the experiments (it is largely taught like that, at least) and it is low energy limit (supergravity) of very promising and/but very general string theories.

Even if Standard Model explains excellent all the experiments done up to now, it has a great number of problems from the theoretical point of view. At the first place, does not include the gravity and does not lead to the coupling unification at high energies. This is naturally solved in the framework of supergravity theories, as well as the following problems. Standard Model contains a great number of free parameters like the three coupling constants, the two Higgs potential parameters, the fermion masses, the angles and phases associated to the Cabibbo-Kobayashi-Maskawa matrix. It has common problem of all the gauge theories – radiative corrections to the scalar particle mass quadratically diverge due to fermion loops (this is solved in the framework of supersymmetric theories thanks to the opposite sign contributions to quadratic divergences due to supersymmetric partners). Then, the fine tuning problem and the hierarchy problem are present. Another problem that supersymmetry solves is cosmological problem of the missing matter, that we have to face of, too.

Here, we can not enter in all the details about the problems of the Standard Model and give a deserved introduction and complete treatment of supersymmetric theories, but we will rather mention some of the crucial points in order to be able formulate consistently the minimal supersymmetric extension of the Standard Model from its particle content point of view; we will also see its connection with minimal supergravity. Recommended references are [14, 70, 130], as well as many other well known books and reviews about the supersymmetric theories where interested reader can find the historical introduction, mathematical basis and step-by-step introduction in supergravity theories.

2.2 The Minimal Supersymmetric Standard Model

In this section we will introduce the supersymmetric model that has the minimal number of particles (the Standard Model fermions and gauge bosons, two Higgs doublets instead of one in the Standard Model and the corresponding superpartners) and is extension of the Standard Model. In the next section we will make a connection with minimal supergravity theory. In particular, this model contains four neutral spin 1/2 Majorana particles, the superpartners of the neutral gauge bosons \tilde{B} and \tilde{W}_3 and the neutral CP-even Higgsinos \tilde{H}_1^0 and \tilde{H}_2^0 . The four mass eigenstates obtained by diagonalizing the corresponding mass matrix are the four neutralinos. The lightest one is the ideal candidate for dark matter.

Once the concept of the "fermionic" extension of Poincare symmetry (or any Lie manifold) was known (see Appendix 1), it was possible to (try) construct the (realistic) theory that has also invariance with respect to some gauge group and to introduce some supersymmetry breaking mechanism. In order to construct this realistic theory we need to associate the particles to correct representations of supersymmetry and gauge group (see Appendix 1 for some basic representations of N=1 super-Poincare group). As the Standard Model fermions of a given chirality belong to the fundamental representation of the gauge group and standard vector bosons belong to the adjoint representation, it is not possible to put them together in the same supermultiplet. Fermions have to be inserted into a chiral supermultiplet while gauge vector bosons belong to a vector supermultiplet. Also, the Higgs bosons can not be inside the same chiral multiplet of the standard fermions because this does not allow the right fermionic mass spectrum [1]. The Standard Model (SM) left fermions transform differently under the gauge group than the right

fermions, so they must be accommodated in different chiral supermultiplet.

To every standard particle is associated a supersymmetric partner: scalar partners of quarks and leptons are called squarks and sleptons (scalar quarks and scalar leptons). Left and right pieces of quarks and leptons are separate Weyl fermions with different gauge transformation properties in the SM, so each must have its own complex scalar partner. Symbols for squarks and sleptons are the same as for the corresponding fermions with a tilde added. Superpartners of left and right parts of electron field are called left and right selectrons and are denoted \tilde{e}_L and \tilde{e}_R (left or right refer to the helicity of the superpartners of selectrons, of-course), for example; smuons and staus would be $\tilde{\mu}_L, \tilde{\mu}_R, \tilde{\tau}_L, \tilde{\tau}_R$. SM neutrinos are always left, so sneutrinos are denoted by $\tilde{\nu}_e, \tilde{\nu}_\mu, \tilde{\nu}_\tau$, with indication which lepton flavor they carry. Squarks are \tilde{q}_L, \tilde{q}_R with $q = u, d, s, c, b, t$. The gauge interactions of each of these squark and slepton fields are the same as those of the corresponding SM fermion: left squark like \tilde{u}_L will couple to W boson while \tilde{u}_R will not, for example. Higgs scalar should be in a chiral supermultiplet (due to its spin).

If there was only one Higgs chiral supermultiplet, it can be shown that the electroweak gauge symmetry would suffer a triangle gauge anomaly. This can be avoided if there are two Higgs supermultiplets, one with each of weak hypercharge $Y = \pm 1/2$. The $SU(2)$ doublet complex scalar fields corresponding to these two cases we denote H_u and H_d . The weak isospin components of H_u with $T_3 = (+1/2, -1/2)$ have electric charges 1 and 0, and are denoted (H_u^+, H_u^0) . Similarly, the $SU(2)$ doublet complex scalar H_d has $T_3 = (+1/2, -1/2)$ components (H_d^0, H_d^-) . The neutral scalar that corresponds to the physical SM Higgs boson is in a linear combination of H_u^0 and H_d^0 . The generic nomenclature for a spin-1/2 superpartner is to add the suffix "-ino" to the name of the SM particle, so the fermionic partners of the Higgs scalars are called higgsinos. They are denoted by \tilde{H}_u, \tilde{H}_d for the $SU(2)$ doublet left Weyl spinor fields, with weak isospin components $\tilde{H}_u^+, \tilde{H}_u^0$ and $\tilde{H}_d^0, \tilde{H}_d^-$.

The matter content of the theory is summarized in table 2.1, which gives the transformation properties of the SM fields with respect to the gauge group.

In the first row of table 2.1 we have put the chiral superfields that contain the component fields indicated in the other rows, $i = 1, 2, 3$ is a family index. We have followed the standard convention that all chiral supermultiplets are defined in terms of left Weyl spinors, so that in the table there are the conjugates of the right quarks and leptons.

The vector bosons of the SM clearly must reside in gauge supermultiplets. The fermionic superpartners are referred as gauginos. The $SU(3)$ color gauge interactions of QCD are mediated by the gluon g , denoted

Supermultiplet	spin 0	spin 1/2	$SU(3) \otimes SU(2) \otimes U(1)$
Q_i	$(\tilde{u}_L \tilde{d}_L)$	$(u_L d_L)$	$(\mathbf{3}, \mathbf{2}, 1/6)$
\bar{u}_i	\tilde{u}_R^*	u_R^\dagger	$(\bar{\mathbf{3}}, \mathbf{1}, -2/3)$
\bar{d}_i	\tilde{d}_R^*	d_R^\dagger	$(\bar{\mathbf{3}}, \mathbf{1}, 1/3)$
L_i	$(\tilde{\nu} \tilde{e}_L)$	(νe_L)	$(\mathbf{1}, \mathbf{2}, -1/2)$
\bar{e}_i	\tilde{e}_R^*	e_R^\dagger	$(\mathbf{1}, \mathbf{1}, 1)$
H_u	$(H_u^+ H_u^0)$	$(\tilde{H}_u^+ \tilde{H}_u^0)$	$(\mathbf{1}, \mathbf{2}, 1/2)$
H_d	$(H_d^0 H_d^-)$	$(\tilde{H}_d^0 \tilde{H}_d^-)$	$(\mathbf{1}, \mathbf{2}, -1/2)$

Table 2.1: Minimal supersymmetric standard model chiral supermultiplets

with \tilde{g} . The electroweak gauge symmetry $SU(2) \otimes U(1)$ possesses as gauge bosons W^+ , W^0 , W^- and B^0 . The corresponding spin 1/2 superpartners \tilde{W}^+ , \tilde{W}^0 , \tilde{W}^- and \tilde{B}^0 are called winos and bino. After electroweak symmetry breaking, the W^0 and B^0 gauge eigenstates mix to give mass eigenstates Z^0 and γ . The corresponding gaugino mixtures of \tilde{W}^0 and \tilde{B}^0 , denoted by \tilde{Z}^0 and $\tilde{\gamma}$, are called zino and photino: if supersymmetry were unbroken, they would be mass eigenstates with masses m_Z and 0.

In the table 2.2 we have summarized the gauge supermultiplets of the minimal supersymmetric standard model (MSSM).

Fields	spin 1/2	spin 1	$SU(3) \otimes SU(2) \otimes U(1)$
gluino, gluon	\tilde{g}	g	$(\mathbf{8}, \mathbf{1}, 0)$
winos, W bosons	$\tilde{W}^\pm \tilde{W}^0$	$W^\pm W^0$	$(\mathbf{1}, \mathbf{3}, 0)$
bino, B boson	\tilde{B}^0	B^0	$(\mathbf{1}, \mathbf{1}, 0)$

Table 2.2: MSSM gauge supermultiplets

The chiral and gauge supermultiplets appearing in tables 2.1 and 2.2 completely describe the particle content of the MSSM. In a renormalizable supersymmetric theory the interactions and masses of all particles are determined just by their gauge transformation properties (in the case of the MSSM are given by the $SU(3) \otimes SU(2) \otimes U(1)$ gauge group) and by the superpotential W , that appear in the most general $N = 1$ supersymmetric lagrangian.

The superpotential W is a function of chiral superfields only and it determines every non gauge interaction of the theory

$$W = \frac{1}{2}m_{ij}\Phi_i\Phi_j + \frac{1}{2}y_{ijk}\Phi_i\Phi_j\Phi_k. \quad (2.1)$$

The superpotential determines not only the scalar interactions but also the fermion masses and Yukawa couplings. Thus, once the supermultiplet content of theory is given, the form of the superpotential is constrained by gauge invariance, and so only a subset of the couplings m_{ij} and y_{ijk} are allowed to be non zero. For example the entries of the mass matrix m_{ij} can only be non zero for i and j such that the superfields Φ_i and Φ_j transform under the gauge group in representations that are conjugate of each other¹. Likewise, the Yukawa couplings y_{ijk} can only be non zero when Φ_i , Φ_j and Φ_k transform according to representations which can combine to form a singlet.

The superpotential for the MSSM is given by

$$W_{MSSM} = \mu H_u H_d + (y_u \bar{u} Q H_u - y_d \bar{d} Q H_d - y_e \bar{e} L H_d), \quad (2.2)$$

where the fields that appear in this equation are the chiral superfields defined in table 2.1 and where we have suppressed all the gauge and family indices. The dimensionless Yukawa couplings y_u , y_d and y_e are 3×3 matrices in family space. The first term in equation 2.2 is the " μ term", and it is the only allowed mass term. It is the supersymmetric analogue of the Higgs mass term, and it is essentially unique because terms like $H_u^* H_u$ or $H_d^* H_d$ are forbidden in the superpotential 2.2, which is an analytic function of chiral superfields. It can be written in terms of an $SU(2)$ doublet as

$$\mu H_u H_d = \mu \epsilon^{\alpha\beta} (H_u)_\alpha (H_d)_\beta, \quad (2.3)$$

where $\epsilon^{\alpha\beta}$ is the $SU(2)$ metric. In an analogous way the second term, that is a Yukawa type term, can be written as

$$y_u \bar{u} Q H_u = \epsilon^{\alpha\beta} \bar{u}_a^i (y_u)_i^j Q_{j\alpha}^a (H_u)_\beta, \quad (2.4)$$

where now we have explicitly written the family indices $i = 1, 2, 3$ and the $SU(3)$ gauge indices $a = 1, 2, 3$ of the fundamental representation $\mathbf{3}$.

The Yukawa matrices determine the masses and Cabibbo-Kobayashi-Maskawa mixing angles of the ordinary quarks and leptons after the neutral scalar components of H_u and H_d get VEVs. Since the top quark t , the bottom quark b and the τ lepton are the heaviest fermions in the SM, it is often

¹In the MSSM there is only one possible term of this type.

useful to make an approximation that only the (3, 3) family components of y_u , y_d and y_e are important

$$y_u \sim \begin{pmatrix} 0 & 0 & 0 \\ 0 & 0 & 0 \\ 0 & 0 & y_t \end{pmatrix} \quad y_d \sim \begin{pmatrix} 0 & 0 & 0 \\ 0 & 0 & 0 \\ 0 & 0 & y_b \end{pmatrix} \quad y_e \sim \begin{pmatrix} 0 & 0 & 0 \\ 0 & 0 & 0 \\ 0 & 0 & y_\tau \end{pmatrix} \quad (2.5)$$

In this limit only the third family and Higgs fields contribute to the MSSM superpotential. However, it is useful to remember that the dimensionless interactions determined by the superpotential 2.2 are often not the most important ones from the phenomenological point of view. In fact the Yukawa couplings are very small, except for those of the third family. Instead, the decay and production processes of superpartners in the MSSM are typically dominated by the supersymmetric interactions of gauge coupling strength. The couplings of the SM gauge bosons to the MSSM particles are completely determined by the gauge invariance of the kinetic terms in the lagrangian [75].

There are also various scalar quartic interactions in the MSSM which are uniquely determined by gauge invariance and supersymmetry. They are dictated by the scalar potential (here we can not enter in details, to interested reader is recommended to see the standard literature given at the beginning of this section). The dimensionful terms in the supersymmetric part of the MSSM lagrangian are all dependent on μ , that appears in the generalization of the Higgs mass term of the MSSM superpotential. We find that μ gives the higgsino mass terms in the MSSM lagrangian

$$\mathcal{L} \supset -\mu \left(\tilde{H}_u^+ \tilde{H}_d^- - \tilde{H}_u^0 \tilde{H}_d^0 \right) + c.c., \quad (2.6)$$

as well as Higgs mass square terms in the scalar potential

$$-\mathcal{L} \supset \mathcal{V} \supset |\mu|^2 (|H_u^0|^2 + |H_u^+|^2 + |H_d^0|^2 + |H_d^-|^2), \quad (2.7)$$

where \mathcal{V} is the scalar potential. Since the Higgs part of the scalar potential is positive definite, we cannot understand electroweak symmetry breaking without including soft supersymmetry breaking terms for the Higgs scalars, which can be negative. So, to complete the description of the MSSM, we need to specify the soft supersymmetry breaking. The soft breaking lagrangian can be written as [74]

$$\mathcal{L}_{soft}^{MSSM} = -\frac{1}{2} \left(M_3 \tilde{g}\tilde{g} + M_2 \tilde{W}\tilde{W} + M_1 \tilde{B}\tilde{B} \right) + c.c$$

$$\begin{aligned}
& - \left(\tilde{u} a_u \tilde{Q} H_u - \tilde{d} a_d \tilde{Q} H_d - \tilde{e} a_e \tilde{L} H_d \right) + c.c. \\
& - \tilde{Q}^\dagger m_Q^2 \tilde{Q} - \tilde{L}^\dagger m_L^2 \tilde{L} - \tilde{u} m_u^2 \tilde{u}^\dagger - \tilde{d} m_d^2 \tilde{d}^\dagger - \tilde{e} m_e^2 \tilde{e}^\dagger \\
& - m_{H_u}^2 H_u^* H_u - m_{H_d}^2 H_d^* H_d - (b H_u H_d + c.c.), \tag{2.8}
\end{aligned}$$

where M_1 , M_2 and M_3 are the bino, wino and gluino mass terms and we have suppressed all the gauge indices. The second line of equation 2.8 contains the trilinear scalar couplings. Each of a_u , a_d and a_e is a complex 3×3 matrix in family space, with mass dimension $d = 1$. These matrices are in one-to-one correspondence with the Yukawa coupling matrices that appear in the superpotential. The third line of the equation 2.8 contains the squark and slepton squared mass terms. Each of m_Q^2 , m_L^2 , m_u^2 , m_d^2 and m_e^2 is a 3×3 matrix in family space² which in general can have complex entries. Since the lagrangian must be real, these matrices are hermitian.

Finally the last line of equation 2.8 contains the supersymmetry breaking contributions to the Higgs potential: $m_{H_u}^2$, $m_{H_d}^2$ and b (usually indicated in the literature as $B\mu$) are the only squared mass terms that can occur in the MSSM.

To summarize this discussion about the soft supersymmetry breaking, we must show the order of magnitude of all these terms

$$M_1, M_2, M_3, a_u, a_d, a_e \sim m_{soft} \tag{2.9}$$

$$m_Q^2, m_L^2, m_u^2, m_d^2, m_e^2, m_{H_u}^2, m_{H_d}^2, b \sim m_{soft}^2 \tag{2.10}$$

where m_{soft} is the characteristic mass scale of supersymmetry breaking which is of the order ~ 1 TeV, in order to continue to solve the hierarchy problem [75]. The soft breaking lagrangian 2.8 has the most general form which is compatible with gauge invariance and with R-parity conservation.

The soft lagrangian 2.8 introduces many new parameters which were not present in the ordinary SM. A careful count (see [76]) reveals that in the MSSM lagrangian there are 105 new parameters, respect to the ordinary SM, that cannot be rotated away by redefining the phases and flavor basis for the quark and lepton supermultiplets. Thus, in principle, supersymmetry breaking introduces a huge arbitrariness in the lagrangian.

But we can reduce some of this arbitrariness because most of the new parameters can be constrained by the request that there is no flavor mixing or CP violation of the type which is already restricted by experiments [77].

²To avoid a heavy notation we have neglected the tilde over the name of the scalar fields, like, for example, Q .

This can be evaded assuming that supersymmetry breaking is "universal": the squark and slepton masses are flavor blind, so they should be each proportional to the the 3×3 identity matrix in family space

$$\begin{aligned} (m_Q^2)_i^j &= m_Q^2 \mathbf{1}_{3 \times 3} & (m_{\bar{u}}^2)_i^j &= m_{\bar{u}}^2 \mathbf{1}_{3 \times 3} & (m_{\bar{d}}^2)_i^j &= m_{\bar{d}}^2 \mathbf{1}_{3 \times 3} \\ (m_L^2)_i^j &= m_L^2 \mathbf{1}_{3 \times 3} & (m_{\bar{e}}^2)_i^j &= m_{\bar{e}}^2 \mathbf{1}_{3 \times 3}, \end{aligned} \quad (2.11)$$

where $i, j = 1, 2, 3$ are family indices. In this way all squark and slepton mixing angles are rendered trivial, because squarks and sleptons with the same electroweak quantum numbers will be degenerate in mass and can be rotated into each other. In such limit, supersymmetric contributions to flavor changing processes will therefore be very small.

Moreover, one can make the assumption that the trilinear scalar couplings are each proportional to the corresponding Yukawa couplings

$$a_u = A_{u0} y_u \quad a_d = A_{d0} y_d \quad a_e = A_{e0} y_e. \quad (2.12)$$

This ensures that only the squarks and sleptons of the third family can have large trilinear couplings. Finally, one can avoid disastrously large CP violating effects assuming that the soft parameters do not introduce new complex phases, *i.e.*

$$\arg(M_1), \arg(M_2), \arg(M_3), \arg(A_{u0}), \arg(A_{d0}), \arg(A_{e0}) = 0, \pi. \quad (2.13)$$

The only CP violating phase in the theory will be the ordinary Cabibbo-Kobayashi-Maskawa phase found in the ordinary Yukawa couplings. The relations 2.11, 2.12 and 2.13 make up the so called assumption of *soft breaking universality*.

The origin of the supersymmetry breaking terms and the soft breaking universality relations seems to require an underlying theory that must explain, in the end, the peculiar scale $m_{soft} \sim 1$ TeV. Moreover it remains to explain the origin of the μ term in the Higgs sector of the scalar potential that appears in the equation 2.7. In fact, we expect that μ should be roughly of the order of 10^2 or 10^3 GeV, in order to allow an Higgs VEV of order of 174 GeV without a fine tuning between $|\mu|^2$ and the negative mass squared terms in the last line of the soft lagrangian. The MSSM scalar potential seems to depend on two types of dimensionful parameters which are conceptually quite distinct, namely the supersymmetry respecting mass μ and the supersymmetry breaking soft mass term m_{soft} . The so called μ problem refers to the fact that this two unrelated parameters are of the same order of

magnitude. Several different solutions of the μ problem has been proposed [78] [79] [80]. From the phenomenological point of view we will treat μ as an independent parameter without asking his origin.

Neutralino is a linear combination of the higgsinos and electroweak gauginos. The neutral higgsinos, \widetilde{H}_u^0 and \widetilde{H}_d^0 , and the neutral gauginos \widetilde{W}^0 and \widetilde{B} combine to form four neutral mass eigenstates called neutralinos. We denote the neutralino mass eigenstates by $\widetilde{\chi}_i$, with $i = 1, 2, 3, 4$. By convention the masses are labelled in ascending order: $m_{\widetilde{\chi}_1} < m_{\widetilde{\chi}_2} < m_{\widetilde{\chi}_3} < m_{\widetilde{\chi}_4}$, so the lightest neutralino is the LSP (unless there is a lighter gravitino or if R-parity is not conserved). Introducing a gauge eigenstate basis it is possible to write the neutralino mass terms in the MSSM lagrangian as

$$\mathcal{L} \supset -\frac{1}{2} (\psi^0)^T M_{\widetilde{\chi}} \psi^0 + c.c. \quad (2.14)$$

where

$$\psi^0 = \left(\widetilde{B}, \widetilde{W}^0, \widetilde{H}_d^0, \widetilde{H}_u^0 \right) \quad (2.15)$$

and with the neutralino mass matrix given by

$$M_{\widetilde{\chi}} = \begin{pmatrix} M_1 & 0 & -c_\beta s_W m_Z & s_\beta s_W m_Z \\ 0 & M_2 & c_\beta c_W m_Z & -s_\beta c_W m_Z \\ -c_\beta s_W m_Z & c_\beta c_W m_Z & 0 & -\mu \\ s_\beta s_W m_Z & -s_\beta c_W m_Z & -\mu & 0 \end{pmatrix} \quad (2.16)$$

where the θ_W parameter is the Weinberg angle and where we have introduced the following notation: $s_\beta = \sin \beta$, $c_\beta = \cos \beta$, $s_W = \sin \theta_W$ and $c_W = \cos \theta_W$. Here, we can not enter in all the details, for more see [14, 70], for example. We just note, from now on, the mass of the lightest neutralino with $m_{\widetilde{\chi}} \equiv m_{\widetilde{\chi}_1}$ and we can express $\widetilde{\chi}$ in terms of the mixing diagonalizing matrix N_{ij} as

$$\widetilde{\chi} = N_{11} \widetilde{B} + N_{12} \widetilde{W}^0 + N_{13} \widetilde{H}_u^0 + N_{14} \widetilde{H}_d^0 \quad (2.17)$$

The neutralino composition can be described in terms of an other useful parameter, called gaugino fraction, that is defined in the following way

$$Z_g = |N_{11}|^2 + |N_{12}|^2 \quad (2.18)$$

If $Z_g > 0.5$ then the neutralino is primarily a gaugino, while if $Z_g < 0.5$ then the neutralino is primarily an higgsino.

Chapter 3

Origin and Propagation of Cosmic Rays in the Framework of the Standard Model

3.1 Introduction

Cosmic rays are relatively high energy particles that are coming in the Earth atmosphere, detected for first time by the famous V. Hess balloon experiment in 1912, in which he wanted to measure the ionization rate in the upper atmosphere. From this first detection, cosmic rays become one of the most important problems in the both – experimental and theoretical astrophysics, but their importance is putted at the right place just when the powerful calculators were built. Then, consequently, it was possible to solve, in the beginning relatively simple in comparison with today's models, various theoretical models supposed to give the right way of how cosmic rays are created in the our Galaxy and then transported through it to reach the Solar system. After, those "simple" models were evolving to become more and more complicated, when it was clear that in an easy way one can not reach the production of the spectra of all the cosmic rays together in accordance with more and more sophisticated experiments.

3.2 Introduction to the Production of the Primary and the Secondary Nuclei and Its Importance

Propagation of cosmic rays through the Milky Way is not purely plasma physics that includes diffusive processes in an unknown galactic magnetic fields, sources of primary nuclei of supposed functional type of the spectra with unknown constants and unknown various Galactic parameters. Even in that case, at the first place, the propagation equation would be relatively complicated and difficult to solve numerically due to the processes that require the calculation in the whole phase space (particle momentum as the kinematic variable greatly facilitates the inclusion of the diffusive reacceleration by the second order Fermi mechanism [99]). Second, all the unknown parameters are not measurable in the other ways – but must be constrained by the analysis of the fits of some of the measured spectra of cosmic rays. But, propagation equation also contains complicated nuclear physics processes. For the chains of nuclear reactions it is necessary to know accurately a lot of cross sections. Those cross sections are not measured always, but simulated or parametrized. After all, distributions of Galactic matter are not exactly known, even distributions of all the ionization types of hydrogen and helium (at least their ratio) as well as distribution of gamma rays and other cosmic rays sources.

On the other side, spectra of cosmic rays are the unique way we have to test the creation and propagation models for them done in the framework of Standard Model physics and consequently to check somehow also the Standard Model itself. This becomes more important with a development of Supersymmetry, at the first place, and other exotic physics, because all the models behind the Standard Model have more possibilities for creation of diverse cosmic rays in the plenty of new processes, studied more in details with the time passing (see [121, 91, 123, 7], for example). Here we will mention briefly some of the most important exotic mechanisms as examples.

At first place, in the framework of the Minimal Supersymmetric Standard Model there are new particles that could lead by their interactions to a fresh component for the total antiproton and positron spectra. Those components (often called signal or primary component), depending on the model parameters and the distribution of new particles in the Milky Way, could be also not small in the comparison with the standard production (background). Those models are also very attractive because they solve another very actual and fundamentally important problem of the missing matter in the Universe. As the characteristics of the movement of visible matter in our Galaxy (as ex-

ample) gives the only information about the distribution of Dark Matter, it is clear that new numerical simulations should be done (in fact they were done already, as this question was even before very actual, see [135, 6]) to discover the possible Dark Matter profiles – and this, of course, is taking with itself new undeterminances. Then, it is also not said that this type of Dark Matter is the only one candidate for it. Thus, in this type of calculations one need to check all the possibilities for the extremely big number of free parameters between diverse models included in the considerations. It is very difficult and requiring task in the sense of processor time (at least), even on the newest machines. So, neither Standard Model creation and propagation, neither one in the framework of Supersymmetric models, are still not giving final answer on the question of the origin of the cosmic rays spectra.

Evaporation of black holes also would lead directly to extra components in the antimatter particles spectra that in principle could be detected if one would be sure what part of the measured spectra is due to the standard production.

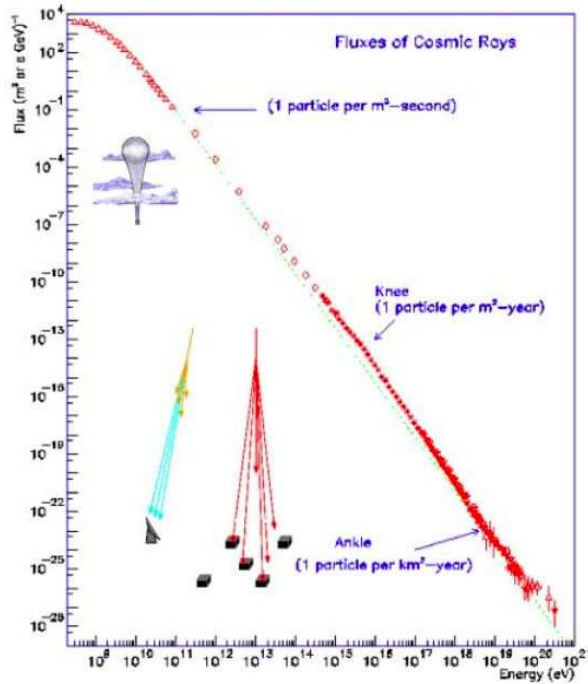
Always there is the problem of the uncertainty of the propagation of the Standard Model spectra. In fact, this is the central problem if one would like do disentangle the exotic contributions. This problem is one of the subjects treated in this thesis.

Other possibility to generate extra antimatter is to have other exotic particles, like axions [91, 92], that we noted in the first chapter already.

Some fundamentally new physics – noncommutative properties of space-time could be the reason also to have an effective permeability of the vacuum different from ϵ_0 and consequently we would receive a distorted γ ray spectra, principally detectable [7].

Even all the mentioned problems, essentially very simple behavior of cosmic rays spectra lead to conclusion that, at least, their production and propagation is lead by by the similar mechanisms over all the energy range; in fact, roughly speaking, all the cosmic rays spectra can be described (above the energies of 10 GeV) by the same functional types – power laws with index around -3 . The only structure appears around 10^{12} GeV! It is a simple "knee" (see figure 3.2), above which again there is no structure (at least up to the "ankle" around 10^{16} GeV), and everything seems to be working in some other unique way again. Unfortunately, at very high energies statistical errors of experimental data are enormous and it is not possible to use them for the propagation analysis: for example, around the "knee" we have a flux of an order of one particle per year per square meter!

What kind of information we can gain from the spectra of the cosmic rays? Different isotopes presented allows one to study acceleration and propagation in the interstellar medium: for example, stabile nuclei gives us parameters



that describe diffusive processes, often modeled as isotropic (diffusion tensor is taken to be proportional to identity operator) and about Galactic wind and the velocity of Alfvén perturbations. However, those assumptions are based on the studies of the spectra in one point in the Milky Way, with the supposition that the spectra are very similar everywhere.

How cosmic rays are produced? Measured X-ray and γ -ray spectra from the supernovae and supernovae remnants and pulsars are suggesting that in their vicinity there are strongly accelerated particles that after escaping are continuing to propagate through the interstellar medium changing their spectra by gaining and losing their energy in various processes. These objects practically act as natural accelerators and produced high energy particles have the potential to create in their collisions various secondary nuclei that are rare in the Universe, like antiprotons and pions that are decaying and producing positrons and electrons (so called secondaries) as well as diffusive γ rays, that are also produced via inverse Compton scattering and bremsstrahlung. So, as example, carefully analyzed, spectra of γ rays could give us the information about the spectra of nuclei and leptons. Synchrotron emitting electrons are accelerated with a second order Fermi mechanism (see later in the text).

Generally speaking, understanding the propagation would lead to very

rich knowledge of the magnetohydrodynamic properties of the our Galaxy as well as properties of its matter content. Even more, in principle, we would be able to detect eventually signs of new physics.

Is there any other classical important mechanism for the production of cosmic rays? The total energy of cosmic rays in the Galaxy may be estimated by multiplying their energy density ($1eV/cm^3$) by the volume of the Galaxy ($\pi(10kpc)^2 \cdot 300pc$). For the lifetime of 3 millions of years this energy would need to be supplied at the rate that only acceptable sources for it are supernova explosions, supposing that from one promile up to one percent of the energy would go to cosmic rays. This is in accordance with later theoretical models of Colgate and White where shock waves after the explosion are accelerated during they passage through the less and less dense upper layers of the presupernova star, taking with itself the mass fraction of the star and ejecting its small peace, finally, with a very high speed. Primary spectra expected from diffusive shock acceleration theories are power lows in impulses. There are also mechanisms based on electromagnetic field around the neutron stars.

3.3 The Most Elementary Results From the Physics of Plasma

3.3.1 Plasma Physics of Propagation

One of the fundamental questions of propagation of charged particles is how to treat their interaction with unknown Galactic chaotic magnetic field. Fermi [99] was the first to give a statistical treatment of the scattering of particles with a random magnetic field, while Chandrasekhar [66] showed that those processes could be treated exactly by the usage of random walk in the configurational space. This was even confirmed from the point of view of relativistic Boltzmann equation [67]. The question of eventual anisotropy of the diffusion tensor was also risen, but we will assume a simple isotropic diffusion (see later).

Generally speaking, various possibilities for the acceleration of charged cosmic rays particles exist [86, 172]. The two most important examples are by longitudinal waves and Fermi-type acceleration. First of all, even if is obvious, we would like to emphasize that any acceleration (here of importance) of a charge particle can be just due to the electric field, never due to magnetic one. Second, high energy particles have power low spectra, and consequently they could not be accelerated by the statical electric field, because in that case they would have very similar energies among themselves, i.e. their spec-

tra would be quasi monochromatic! So, remains stochastic acceleration in a random electric field. Why acceleration and not energy losses? The reason is simple, and essentially thermodynamical: the energy of the particles should tend towards the mean energy of the turbulent motions. For example, the average of the kinetic energy of any particle is extremely small in comparison with the mean kinetic energy of the interstellar clouds and consequently one should expect that in the collisions of cosmic rays with the interstellar clouds particles should increase their energies. Any energy exchanging mechanism between the particles and hydromagnetic turbulences should lead to the transfer of the energy from the turbulence to the particles. In time turbulences tend to loose their energy.

It could be assumed the existence of the convective, Galactic, wind that represents collective movement of the gaseous plasma and the trapped magnetic field outwards Galactic disk, and that could be responsible for the adiabatic losses of energy. The standard textbooks on plasma physics (see, for example, [86]) are treating convective terms as well as Alfvénic waves. Here, we will try to describe briefly those and some other physical processes in plasma following the magnetohydrodynamical approach.

3.3.2 Some of the Methods for the Theoretical Study of the Dynamic of Plasma

The most exact approach for the treatment of plasma is the *kinetical approach* [86], only one which can explain the existence of the effect of *Landau amortization*. This effect is known also as the *specific absorption, resonant absorption* or *inverse effect of Cherenkov*. The effect of Cherenkov is when charged particle which moves through some material medium with velocity bigger than the phase velocity of electromagnetic waves in that medium is emitting the electromagnetic waves (*Cherenkov emission*) and during that process, loosing the energy, starts to slow down till its velocity doesn't become equal to that of the electromagnetic waves in that medium. In the case of Landau's amortization the charged particle which was moving in the beginning with the velocity equal to the phase velocity of electromagnetic waves in the plasma, starts to absorb the energy of the electromagnetic waves and starts to accelerate due to that absorption. The kinetical approach is based on the *kinetical equations* that could be obtained by careful analysis of the collision processes

$$\frac{\partial f_\alpha}{\partial t} + \vec{v} \cdot \frac{\partial f_\alpha}{\partial \vec{r}} + \frac{\vec{F}_\alpha}{m_\alpha} \cdot \frac{\partial f_\alpha}{\partial \vec{v}} = I_\alpha, \quad (3.1)$$

that are entering through the collision integrals I_α , α is counting the types of the particles. From these equations it is possible to get the distribution functions f_α for every type of the particles. For the force density F_α the only one acceptable force to be taken into account is the Lorentz one.

Averaging of these equations over the velocities gives the *electromagnetohydrodynamical equations*. This averaging is a origin of the problems in explanation of Landau's amortization. In these equations enter beside the hydrodynamical quantities (density, pressure, velocity and temperature) also electrical and magnetic field while we deal with the "fluid" of charged particles. So, these equations are combination of hydrodynamical and Maxwell's equations. In hydrodynamical equations enters also Lorentz force through its density in the form $\rho_{el}\vec{E} + \vec{j} \times \vec{B}$, where \vec{j} is density of current and ρ_{el} the density of charge. In the same time, into Maxwell's equations enter the convective terms through which one's the motion of the fluid influences the electromagnetic field. That means that the electromagnetohydrodynamical equations are self-consistent equations of hydrodynamical and electromagnetic quantities. We have

$$\frac{\partial \rho}{\partial t} + \text{div}(\rho \vec{v}) = 0, \quad (3.2)$$

that is the equation of continuity,

$$\rho \frac{\partial \vec{v}}{\partial t} = \rho \vec{f} - \nabla p + \rho_{el} \vec{E} + \vec{j} \times \vec{B} + \mu \Delta \vec{v} + (\lambda + \frac{1}{3}\mu) \nabla(\nabla \cdot \vec{v}), \quad (3.3)$$

that is the Navier-Stokes equation where transport coefficients do not need to be constant,

$$p = F(\rho), \quad (3.4)$$

that is the characteristic equation of barotropic fluid,

$$\vec{j} = \sigma(\vec{E} + \vec{v} \times \vec{B}) + \rho_{el} \vec{v}, \quad (3.5)$$

that is the generalization of the Ohm's law in the non relativistic case, and

$$\text{div} \vec{E} = \frac{1}{\epsilon_0} \rho_{el}, \quad (3.6)$$

$$\text{div} \vec{B} = 0, \quad (3.7)$$

$$rot\vec{E} = -\frac{\partial\vec{B}}{\partial t}, \quad (3.8)$$

and

$$rot\vec{B} = \mu_0\vec{j}, \quad (3.9)$$

that are the Maxwell's equations.

In the case of *the high electroconductivity* of the fluid, that for plasma is satisfied, the system of electrohydrodynamical equations can be simplified in what is called magnetohydrodynamical approximation. First, in that case the interaction of fluid is interaction only with magnetic field, and also $\rho_{el} = 0$. The explanation of why it is possible to make this simplification is the following: if in the system the electroneutrality is broken, than in the system there are two parallel processes, electronic *plasma's oscillations* and *diffusion*. Then, $\rho_{el}(t) = \rho'_{el}(t) + \rho''_{el}(t)$, where ρ'_{el} is the consequence of diffusion and ρ''_{el} of plasma's oscillations. ρ'_{el} decreases slowly and monotonically with the time and on its behavior are superposed very fast oscillations of frequency ω_{pe} through ρ''_{el} . The amplitude of this part decreases with time due to the collisions in the plasma. If τ_{diff} and τ_{osc} are the characteristic times when the ρ'_{el} and ρ''_{el} decrease to zero (respectively), then ρ_{el} has very different form in two cases: when $\tau_{diff} \ll \tau_{osc}$ and when $\tau_{diff} \gg \tau_{osc}$.

We can estimate the order of these two times. If ν_e is the collision frequency of the electron, $\tau_e = \frac{1}{\nu_e}$ the collision time, then $\tau_{osc} \sim \tau_e$. The estimation of τ_{diff} is easily to get if we know the fact that the macroscopical (hydrodynamical) density of charge is ρ'_{el} . Then, from the continuity equation we get

$$\frac{\partial\rho_{el}}{\partial t} + div\vec{j} = 0, \quad \rho_{el} \approx \rho'_{el}, \quad \vec{j} \approx \sigma\vec{E}, \quad (3.10)$$

$$\frac{\partial\rho'_{el}}{\partial t} + \frac{\sigma}{\epsilon_0}\vec{E} = 0, \quad (3.11)$$

the solution of this equation is:

$$\rho'_{el}(t) = \rho'_{el}(0)\exp\left(-\frac{\sigma}{\epsilon_0}t\right), \quad (3.12)$$

from which we can see that the $\tau_{diff} \sim \frac{\epsilon_0}{\sigma}$. Using $\sigma = \frac{e^2 n_e}{m_e \nu_e}$ finally we get $\tau_{diff} \sim \frac{\epsilon_0 m_e}{n_e e^2} \frac{1}{\nu_e}$. From this equation it is obvious that in the case of the fluid with very high electroconductivity (as it is the plasma) τ_e is very big, and consequently τ_{diff} very small so that the space density of charge will be

macroscopically equal to zero ($\tau_{diff} \ll \tau_{osc}$). Then we saw that $\rho_{el} = 0$ is the consequence of the high electroconductivity of a fluid, and this assumption in the case of plasma is adequate.

Putting these approximation into equations (3.5) and (3.6) we get the equations of magneto-hydrodynamical approximation:

$$\frac{\partial \rho}{\partial t} + div(\rho \vec{v}) = 0, \quad (3.13)$$

$$\rho \frac{\partial \vec{v}}{\partial t} = \rho \vec{j} - \nabla p + \frac{1}{\mu_0} (rot \vec{B}) \times \vec{B} + \mu \Delta \vec{v} + (\lambda + \frac{1}{3} \mu) \nabla (\nabla \cdot \vec{v}), \quad (3.14)$$

this equation is now the combination of the Navier-Stoks equation and Ohm's low (where we put $\vec{j} = \frac{1}{\mu_0} rot \vec{B}$ and $\rho_{el} \approx 0$)

$$p = F(\rho), \quad (3.15)$$

that is the characteristic equation of barotropic fluid (if the fluid is not barotropic, it is needed to introduce also the temperature into this equation),

$$\vec{j} = \sigma (\vec{E} + \vec{v} \times \vec{B}) + \rho_{el} \vec{v}, \quad (3.16)$$

$$div \vec{B} = 0, \quad (3.17)$$

$$\frac{\partial \vec{B}}{\partial t} = rot(\vec{v} \times \vec{B}) + \nu_m \Delta \vec{B}, \quad (\nu_m = \frac{1}{\mu_0 \sigma}). \quad (3.18)$$

3.3.3 Convective Effects in the Case of the Infinite Electroconductivity of Plasma

The equation (3.18) says that the local change of magnetic field with time is a consequence of *convection* ($\vec{v} \times \vec{B}$) and *diffusion* ($\Delta \vec{B}$) of magnetic field. Convection means that every part of the fluid wants to remain unchanged all its characteristic quantities during the motion.

In the implementation of the plasma physics in astrophysics the analogy of this equation and the equation for the circulation vector $\vec{\omega} = \frac{1}{2} rot \vec{v}$ of the velocity field in the case of barotropic nonconductive fluid on which act only potential forces is very important. The motion of this fluid is described by the Helmholtz equation – of the same functional type as equation 3.18.

In the case of the fluid of infinity electroconductivity ($\frac{1}{\sigma} = 0$) equation 3.18 becomes

$$\frac{\partial \vec{B}}{\partial t} = \text{rot}(\vec{v} \times \vec{B}), \quad (3.19)$$

and the local changing of the magnetic field with the time is consequence only of the convection effects. As the magnetic field satisfies also Maxwell's equation $\text{div} \vec{B} = 0$ (and these two equations together are mathematically completely analogue to the equation for the $\vec{\omega} = \frac{1}{2} \text{rot} \vec{v}$ for the ideal barotropic fluid on which act only potential forces) it is expected that should be valid some magnetic analogy of the *Hemholtz theorems*. They can be formulate in the next way:

Flux of the magnetic field trough some bounded contour made of the same elements of the electroconducting fluid with an infinite electroconductivity doesn't change during the motion of that contour.

If this would not be hold, during the motion of the physical contour, would be induced infinite currents, which physically doesn't have any sense; so, the fluid should move so that the flux doesn't change.

The elements of the electroconducting fluid with infinite electroconductivity that were at one moment of time on the one line of the magnetic force will stay on the same line of the magnetic force at every moment of time during the motion.

This theorem says that the fluid moves so that its elements are fixed on the lines of the magnetic force, so this is called the *freezing of the lines of the magnetic force*.

There exist few confirmation of this theorem. We will give here one based on the vector's identity

$$\text{rot}(\vec{v} \times \vec{B}) = (\vec{B} \cdot \nabla) \vec{v} - (\vec{v} \cdot \nabla) \vec{B} - \vec{B} \text{div} \vec{v} + \vec{v} \text{div} \vec{B}. \quad (3.20)$$

Using also the equations $\text{div} \vec{B} = 0$ and $\frac{\partial \vec{B}}{\partial t} + (\vec{v} \cdot \nabla) \vec{B} = \frac{d\vec{B}}{dt}$ equation (3.19) becomes

$$\frac{d\vec{B}}{dt} = (\vec{B} \cdot \nabla) \vec{v} - \vec{B} \text{div} \vec{v}. \quad (3.21)$$

We will start explanation of the theorem looking at the element $d\vec{r}$ of the line made of the elements of the fluid of the density ρ . We can introduce the vector $\vec{C} = \vec{B} - k\rho d\vec{r}$, where k is a constant. We can suppose that in the initial moment element $d\vec{r}$ was in the same direction as the magnetic field \vec{B} , then we can find k so that at the initial moment was $\vec{C} = 0$. While

$$\frac{dk}{dt} = 0, \quad \frac{d\rho}{dt} = -\rho \operatorname{div} \vec{v}, \quad \frac{d}{dt}(d\vec{r}) = d\vec{v} = (d\vec{r} \cdot \nabla) \vec{v}, \quad (3.22)$$

we will have that the vector \vec{C} changes with time as

$$\frac{d\vec{C}}{dt} = \frac{d\vec{B}}{dt} - k \frac{d\rho}{dt} d\vec{r} - k \rho d\vec{v} = (\vec{B} \cdot \nabla) \vec{v} - \vec{B} \operatorname{div} \vec{v} + k \rho d\vec{r} \operatorname{div} \vec{v} - k \rho (d\vec{r} \cdot \nabla) \vec{v}, \quad (3.23)$$

and finally,

$$\frac{d\vec{C}}{dt} = (\vec{C} \cdot \nabla) \vec{v} - \vec{C} \operatorname{div} \vec{v}. \quad (3.24)$$

As we have that at the initial moment \vec{C} was equal to 0, then also $\frac{d\vec{C}}{dt}$ will be equal to zero, as also all differentials of the bigger order. That means that the vector \vec{C} will stay equal to zero whole the time during the motion, and that whole the time is valid relation $\vec{B} = k \rho d\vec{r}$ if that was valid at the initial moment. So during the motion the vectors \vec{B} and $d\vec{r}$ remain collinear and that is exactly what says the theorem of "freezing".

The proportionality $|\vec{B}| \sim \rho |d\vec{r}|$ is physically obvious if we look at the element of the fluid of the length dr and the cut dA . During the motion the mass of this element $\rho dA dr$ remains constant. And, in accordance with the theorem the magnetic flux $B dA$ through the base of the element remains also constant. That means that during the motions should be always $B \sim \rho dr$.

For the convection velocity field in the literature were assumed diverse functional types that we will treat after. We will emphasize now just that due to the reflection symmetry with respect to the Galactic plane it would be unnatural to assume velocity fields that are different from zero in the disk (i.e. in $z = 0^\pm$) and that would suffer a delta function jump in the Galactic plane.

3.3.4 Elementary Hydrodynamical Theory of Waves Propagation in Plasma

General Relations for the Plain Waves

The equations which describe the wave processes in some medium can be obtained from the basic dynamical equations for that medium applying on it *method of the perturbations*. For this method is characteristic that it is assumed that the medium is in the *stationary state* and that on that stationary state it is possible to superpose the perturbations of all relevant quantities.

Usually, after that it is needed to linearize these equations, and that means to restrict the description on the *small amplitudes*. It is assumed that the plasma in the stationary state is in the rest and that is homogenous. Then the equations for the perturbations are differential equations with constant coefficients. The solutions of these equations are *plain waves*.

If the medium in which the waves expand is infinite then the differential equations are homogenous and they don't have always solutions. The condition of compatibility of these equations is known as a *dispersion equation*, which makes connection between the frequency of wave's oscillations ω and wave's vector \vec{k} . This connection is in general very complicated and has a form

$$F(\omega, \vec{k}) \equiv F(\omega, k_x, k_y, k_z) = 0. \quad (3.25)$$

This equation can have in general many solutions over ω (we will see that in the plasma case the maximum number of solutions is four)

$$\omega_n = \omega_n(\vec{k}) = \omega_n(k_x, k_y, k_z), \quad (n = 1, 2, 3, \dots), \quad (3.26)$$

and every solution corresponds to the one type of the waves, i.e. *wave's mode*. This relation is *dispersion equation of a given wave's mode* and contains all information about characteristics of a given mode. We can see that from next reasoning: if the wave's vector \vec{k} is real, then (if we write $\omega_n = Re\omega_n + iIm\omega_n$) the plain wave has the form

$$Ae^{-\omega t + i\vec{k} \cdot \vec{r}} = [Ae^{(Im\omega_n)t}]e^{-i(Re\omega_n)t + i\vec{k} \cdot \vec{r}}. \quad (3.27)$$

This equation corresponds to the wave process with the frequency $Re\omega_n$, which amplitude increases or decreases depended on the sign of $Im\omega_n$, so that $Im\omega_n$ is exactly increment (decrement) of the amplitude

$$\omega = Re\omega_n \quad \gamma = Im\omega_n \quad (3.28)$$

First of these relations is *spectra* of a given mode, and from that equation it is possible get the *phase* and *group* velocity of the mode.

$$v_{ph} = \frac{\omega}{k} \quad \vec{v}_g = \frac{\partial \omega}{\partial \vec{k}} \quad (3.29)$$

First equation gives the velocity of the emerging of the phase of the wave (this is always in the direction of the vector \vec{k}), and second gives the direction of the transport of the energy through the wave (this a priori is not necessary to be in the direction of vector \vec{k}). Specially, if $\vec{v}_g = 0$ (the energy of the perturbation does not emerge from the place of appearance) then the perturbation is called *oscillation*; and $\vec{v}_g \neq 0$ it is *wave*.

Ideal Noncompressible Electroconductive Fluid: Alfaén and Modified Alfvén Wave

In the case of *ideal noncompressible electro-conductive fluid* the system of equations (3.13,3.14,3.15,3.16,3.17 and 3.18) becomes

$$\operatorname{div} \vec{v} = 0 \quad (3.30)$$

$$\rho \left[\frac{\partial \vec{v}}{\partial t} + (\vec{v} \cdot \nabla) \vec{v} \right] = -\nabla p + \frac{1}{\mu_0} (\operatorname{rot} \vec{B}) \times \vec{B} \quad (3.31)$$

$$\frac{\partial \vec{B}}{\partial t} = \operatorname{rot}(\vec{v} \times \vec{B}) \quad (3.32)$$

$$\operatorname{div} \vec{B} = 0 \quad (3.33)$$

We can label with $p = p_0$, $\rho = \rho_0$, $\vec{v} = \vec{v}_0 = 0$ and $\vec{B} = \vec{B}_0$ the characteristic quantities of the fluid in the stationary state, and with primes the perturbation of these quantities. If we put into the equations the values of the quantities in the stationary state the equations are identically satisfied, and if we put the perturbed quantities $p = p_0 + p'$, $\rho = \rho_0 + \rho'$, $\vec{v} = \vec{v}'$ and $\vec{B} = \vec{B}_0 + \vec{v}'$ we have

$$\operatorname{div} \vec{v}' = 0 \quad (3.34)$$

$$\rho_0 \left[\frac{\partial \vec{v}'}{\partial t} + (\vec{v}' \cdot \nabla) \vec{v}' \right] = -\nabla p' + \frac{1}{\mu_0} (\operatorname{rot} \vec{B}') \times (\vec{B}_0 + \vec{B}') \quad (3.35)$$

$$\frac{\partial \vec{B}'}{\partial t} = \operatorname{rot}[\vec{v}' \times (\vec{B}_0 + \vec{B}')] \quad (3.36)$$

$$\operatorname{div} \vec{B}' = 0 \quad (3.37)$$

We will choose the referent system so that the z axes is in the direction of wave vector \vec{k} , and the x axes choose on that way that vector of magnetic field lays in the xOz-plane. If we label with θ angle between \vec{v} and \vec{B}_0 we will have

$$\vec{k} = k \vec{e}_z, \quad (3.38)$$

$$\vec{B}_0 = B_0 (\sin \theta \vec{e}_x + \cos \theta \vec{e}_z), \quad (3.39)$$

$$e^{-i\omega t + i\vec{k}\cdot\vec{r}} = e^{-i\omega t + ikz} \quad (3.40)$$

Due to this choice of the coordinates the perturbations \vec{v}' , \vec{B}' , and p' depends only on z coordinate, so we can put $\frac{\partial}{\partial x} = \frac{\partial}{\partial y} = 0$. So from the equations (3.34) and (3.37) we have

$$\frac{\partial v'_z}{\partial z} = 0, \quad \frac{\partial B'_z}{\partial z} = 0 \quad (3.41)$$

That means that these perturbations don't change with, they have constant value, and if we choose the condition on the border (infinite system) so that the value of them are zero we have that

$$v'_z = 0 \quad B'_z = 0 \quad (3.42)$$

In the infinite noncompressible ideally electroconducting fluid the waves that emerge are purely transversal, in both sense, hydrodynamically ($v'_z = 0$) and electrodynamically ($B'_z = 0$).

Having this in mind, the equations (3.35) and (3.36) can be rewritten in the scalar form

$$\rho_0 \frac{\partial v'_x}{\partial t} = \frac{1}{\mu_0} B_0 \cos \theta \frac{\partial B'_x}{\partial z}, \quad (3.43)$$

$$\rho_0 \frac{\partial v'_y}{\partial t} = \frac{1}{\mu_0} B_0 \cos \theta \frac{\partial B'_y}{\partial z}, \quad (3.44)$$

$$0 = -\frac{\partial p'}{\partial z} - \frac{1}{\mu_0} (B'_x \frac{\partial B'_x}{\partial z} + B'_y \frac{\partial B'_y}{\partial z} + B_0 \sin \theta \frac{\partial B'_x}{\partial z}); \quad (3.45)$$

$$\frac{\partial B'_x}{\partial t} = B_0 \cos \theta \frac{\partial v'_x}{\partial z}, \quad (3.46)$$

$$\frac{\partial B'_y}{\partial t} = B_0 \cos \theta \frac{\partial v'_y}{\partial z}, \quad (3.47)$$

The equation (3.45) is possible to rewrite in the form

$$\frac{\partial}{\partial z} [p' + \frac{1}{2\mu_0} (B_x'^2 + B_y'^2) + \frac{1}{\mu_0} B_0 B'_x \sin \theta] = 0; \quad (3.48)$$

The last term is the scalar product of vectors $\vec{B}' = B'_x \vec{e}_x + B'_y \vec{e}_y$ and $\vec{B}_0 = B_0 \sin \theta \vec{e}_x + B_0 \cos \theta \vec{e}_z$. If we add constant term (which doesn't depend on z , so after derivation by z gives zero) $p_0 + \frac{1}{2\mu_0} B_0^2$ we have

$$\frac{\partial}{\partial z} [p' + p_0 + \frac{1}{2\mu_0} (\vec{B}'_0{}^2 + 2\vec{B}_0 \cdot \vec{B}' + \vec{B}'^2)] = 0; \quad (3.49)$$

$$\frac{\partial}{\partial z} (p + \frac{1}{2\mu_0} B^2) = 0. \quad (3.50)$$

The equation (3.45) from the upper system of equations determines the pressure in the fluid and gives that the sum of hydrodynamic and magnetic pressure in fluid in perturbed state doesn't depend on the z coordinate, i.e. in every moment of time has the same value in all points of fluid. Using the conditions on the border, where perturbation doesn't exist we can conclude that the pressure is equal to the unperturbed pressure $p_0 + \frac{1}{\mu_0} B_0^2$. So, the equations that determine characteristics of fluid rest equations for \vec{v}' and \vec{B}' . These equations are already *linear* in perturbation, so that *in the noncompressible fluid it is possible find the solutions of wave equations with arbitrary big amplitudes* (the linearizations, i.e. restriction to the behaviors with small amplitudes, it is not needed while the equations are already linear).

The remain four equations are not in fact four equations with four unknown functions v'_x, v'_y, B'_x and B'_y , but two independent systems of two equations with two unknown functions, one with v'_x and B'_x , and another with v'_y and B'_y , as the unknown functions. Physically, that means that in the noncompressible fluid can propagate two *independent* wave modes, one (with v'_y and B'_y) is wave in which both, the vector of hydrodynamical velocity of the fluid particles and the vector of the perturbation of the magnetic field are orthogonal to the both, the direction of the propagation of the wave (direction of the vector \vec{k}) and the direction of the external magnetic field (the vector \vec{B}_0 , in the xOz plane). This mode is called *Alfvén magnetohydrodynamical wave*. The second mode (with v'_x and B'_x) is the wave in which both, the vector of hydrodynamical velocity of the fluid particles and the vector of the perturbation of the magnetic field are orthogonal to the direction of the propagation of the wave (direction of the vector \vec{k}), but they are not orthogonal to the direction of the external magnetic field. This mode is called *modified Alfvén wave*.

In the case of the propagation of the wave along the direction of external magnetic field modified Alfvén wave has the same characteristics as Alfvén wave, so in that case we have two Alfvén waves with orthogonal direction of polarization, which means that the polarization can be arbitrary and will not be changed with the propagation. If $\theta \neq 0$ in the fluid there are Alfvén and modified Alfvén waves which are not polarized on the same way, and which are physically nonequivalent because of the different relations between \vec{v}' and \vec{B}_0 on one and \vec{B}' and \vec{B}_0 on the other side.

If we try to find the solution of the equations for the Alfvén and modified Alfvén wave in the form of plain waves, after cancelation of the exponential factors, we get the equations for the amplitudes of the waves

$$\begin{aligned} -i\omega\rho_0\hat{v} &= i\frac{1}{\mu_0}B_0\cos\theta k\hat{B} \\ -i\omega\hat{B} &= iB_0\cos\theta k\hat{v} \end{aligned} \quad (3.51)$$

This is the system of two homogeneous equations which has nontrivial solutions only if the determinant is equal to zero. That means

$$\omega^2 = k^2v_A^2\cos^2\theta \quad (3.52)$$

where v_A is *Alfvén velocity*. From this it is obvious that both, Alfvén and modified Alfvén waves have the same dispersion relation

$$\omega = \pm kv_A\cos\theta = \pm v_A\frac{\vec{k} \cdot \vec{B}}{B_0} \quad (3.53)$$

two signs represent two directions of the wave propagation correspond to direction of magnetic field.

From the dispersion relation we can find phase and group velocity

$$v_{ph} = \pm v_A\cos\theta, \quad \vec{v}_g = \pm v_A\frac{\vec{B}_0}{B_0} \quad (3.54)$$

From these equation it is easily to see that both, Alfvén and modified Alfvén waves can not propagate in the direction orthogonal to the direction of the magnetic field (the phase velocity becomes equal to zero when $\theta = \frac{\pi}{2}$), and that the group velocity of both waves is numerically equal to v_A and collinear to the magnetic field, doesn't matter what is the value of angle θ . This is the consequence of the fact that in the fluid of the infinitive electroconductivity lines of magnetic force are "frezed", i.e. that the elements of the fluid are stacked to them. While it is valid

$$\hat{v} = \pm\frac{v_A}{B_0}\hat{B} = \pm\frac{\hat{B}}{\sqrt{\mu_0\rho_0}}, \text{ and } v' = \pm\frac{v_A}{B_0}B' = \pm\frac{B'}{\sqrt{\mu_0\rho_0}} \quad (3.55)$$

we have that

$$\frac{1}{2}\rho_0v'^2 = \frac{1}{2\mu_0}B'^2, \quad (3.56)$$

ie. that the density of the kinetic energy of the fluid the the density of the energy of the magnetic field of the wave are equal (looking their amplitudes, but also the phases). The consequence of the previous equation is also relation

$$\left| \frac{v'}{v_A} \right| = \left| \frac{B'}{B_0} \right|, \quad (3.57)$$

If for the wave is valid $|v'| \gg v_A$, then also should be valid $|B'| \gg B_0$. This is very important property of Alfvén waves: *they can amplify incident magnetic field and transport it over the big distances.*

If the fluid that describes the plasma system is compressible in the system of equations that describes the non-compressible fluid we should add the equation which determines how the pressure change with the density, and modified first equation left it in the original form of the continuity equation

$$p = F(\rho), \quad (3.58)$$

$$\frac{\partial \rho}{\partial t} + \text{div}(\rho \vec{v}) = 0. \quad (3.59)$$

Also, for the perturbed case we have one equation more (dependance of the pressure on the density) and modified first equation

$$p' = F(\rho_0 + \rho') - F(\rho_0), \quad (3.60)$$

$$\frac{\partial \rho'}{\partial t} + \text{div}[(\rho_0 + \rho') \vec{v}'] = 0. \quad (3.61)$$

In the difference of the case of non-compressible fluid here it is not possible find the solution in the general case, it is needed first linearized the equation (i.e. restrict description on the waves of small amplitudes). Linearized equations are

$$\frac{\partial \rho'}{\partial t} + \rho_0 \text{div} \vec{v}' = 0, \quad (3.62)$$

$$\rho_0 \frac{\partial \vec{v}'}{\partial t} = -\nabla p' + \frac{1}{\mu_0} (\text{rot} \vec{B}') \times \vec{B}_0, \quad (3.63)$$

$$p' = a^2 \rho', \quad \left[a^2 = \left(\frac{\partial F}{\partial \rho} \right) \right], \quad (3.64)$$

$$\frac{\partial \vec{B}'}{\partial t} = \text{rot}(\vec{v}' \times \vec{B}_0), \quad (3.65)$$

$$.div\vec{B}' = 0 \quad (3.66)$$

In the third equation (characteristic fluid equation) a is the sound velocity. Writing the equation in the form of scalar projections in k -referent system, and looking the solution in the form of plain waves we get six scalar equation with the wave's amplitudes $\hat{\rho}$, \hat{v}_x , \hat{v}_y , \hat{v}_z , \hat{B}_x and \hat{B}_y (from equation (3.66) follows that $B'_z = 0$, which means that also in the compressible fluid the waves are transversal) are unknown. These six equations make two independent systems, one of two equations, where enter \hat{v}_y and \hat{B}_y , and second of four equations where enter the other four amplitudes as an unknown variables that should determine.

The sistem of equations

$$\begin{aligned} -\omega\hat{v}_y &= \frac{kB_0\cos\theta}{\mu_0\rho_0}\hat{B}_y \\ -\omega\hat{B}_y &= kB_0\cos\theta\hat{v}_y \end{aligned} \quad (3.67)$$

is identical to the system of equations (3.51) for the non-compressible fluid. Its solution is Alfvén wave with vectors \vec{v}' and \vec{B}' orthogonal to both, \vec{k} and \vec{B} vectors, and with phase velocity $v_{ph} = \pm v_A \cos\theta$.

The second system gives the solution for $\hat{\rho}$, \hat{v}_x , \hat{v}_z and \hat{B}_x ,

$$\begin{aligned} -\omega\hat{\rho} + \rho_0k\hat{v}_z &= 0 \\ -\omega\hat{v}_x &= \frac{kB_0\cos\theta}{\mu_0\rho_0}\hat{B}_x \\ -\omega\hat{v}_z &= -\frac{a^2}{\rho_0}k\hat{\rho} - \frac{kB_0\sin\theta}{\mu_0\rho_0}\hat{B}_x \\ -\omega\hat{B}_x &= kB_0\cos\theta\hat{v}_x - kB_0\sin\theta\hat{v}_z. \end{aligned} \quad (3.68)$$

After elimination of $\hat{\rho}$ from first and third equations from this system and after introducing the phase velocity $v_{ph} = \frac{\omega}{k}$ the system get form

$$\begin{aligned} v_{ph}\hat{v}_x + \frac{B_0\cos\theta}{\mu_0\rho_0}\hat{B}_x &= 0 \\ (v_{ph} - \frac{a^2}{v_{ph}})\hat{v}_z - \frac{B_0\sin\theta}{\mu_0\rho_0}\hat{B}_x &= 0 \\ v_{ph}\hat{B}_x &= -B_0\cos\theta\hat{v}_x + B_0\sin\theta\hat{v}_z \end{aligned} \quad (3.69)$$

The wave that is solution of this system is in the electrodynamical sense transversal wave, but in the hydrodynamical it is not neither pure transversal, neither pure longitudinal. Also, the propagation of this wave is followed by the perturbation of the density $\hat{\rho} = \rho_0 \frac{\hat{v}_z}{v_f}$, and that is in general one *compressional wave*.

First, we can look two special cases: *direct waves* that propagate in the direction of the external magnetic field, and the waves that propagate in the direction orthogonal to the direction of the external magnetic field.

In the case of the direct waves the equations become

$$\begin{aligned} v_{ph}\hat{v}_x + \frac{B_0}{\mu_0\rho_0}\hat{B}_x &= 0 \\ (v_{ph} - \frac{a^2}{v_{ph}})\hat{v}_z &= 0 \\ v_{ph}\hat{B}_x + B_0\hat{v}_x &= 0 \end{aligned} \quad (3.70)$$

The second equation is independent of the two others and describes the longitudinal wave which propagate with velocity $v_{ph} = a$, and which propagation is not followed by the perturbation of the magnetic field; that is simple *acoustic wave*. The two remain equation describe one Alfvén wave. The conclusion is that *in the direction of the external magnetic field through the infinite, compressible and ideal electroconductiong fluids propagate two Alfvén waves (which propagation is not followed by the changing in the fluid density) with independent polarization's directions and one longitudinal (compressional) acoustic wave*.

The case of the propagation in the direction orthogonal to the direction of the external magnetic field ($\theta = \frac{\pi}{2}$) is described by the equations

$$v_{ph}\hat{v}_x = 0, \quad (3.71)$$

$$(v_{ph} - \frac{a^2}{v_{ph}})\hat{v}_z - \frac{B_0}{\mu_0\rho_0}\hat{B}_x = 0, \quad (3.72)$$

$$v_{ph}\hat{B}_x - B_0\sin\theta\hat{v}_z = 0. \quad (3.73)$$

The solution is one compression wave (*normal magnetic sound*), hydrodynamically longitudinal, and electrodynamically transversal with the phase velocity $v_{ph}^2 = a^2 + v_A^2$.

Now we can look the general case: the system (3.69) has nontrivial solution only when the corresponding determinant is equal to zero. That condition gives equation

$$v_{ph}^4 - (a^2 + v_A^2)v_{ph}^2 + a^2v_A^2\cos^2\theta = 0. \quad (3.74)$$

The solutions of this fourth degree equation are

$$v_{ph}^{(+)} = \frac{1}{\sqrt{2}}\sqrt{(a^2 + v_A^2) + \sqrt{(a^2 + v_A^2)^2 - 4a^2v_A^2\cos^2\theta}} \quad (3.75)$$

and

$$v_{ph}^{(-)} = \frac{1}{\sqrt{2}}\sqrt{(a^2 + v_A^2) - \sqrt{(a^2 + v_A^2)^2 - 4a^2v_A^2\cos^2\theta}} \quad (3.76)$$

These two waves take the names *fast* and *slow magnetic sound*.

3.3.5 Second Order Fermi Acceleration Mechanism

The equations for the second order Fermi acceleration mechanism can be deduced in the framework of the *orbital method in the plasma dynamics*. In that approach is assumed that the set of the charged particles behave in the same way as the single particle (this assumption is valid in the case of diluted plasma, when it is possible to neglect microscopic electromagnetic field of any particle and it is possible assume that every particle moves independently of the others). It is assumed also that the $\vec{E}(\vec{r}, t)$, $\vec{B}(\vec{r}, t)$ and $\vec{\Phi}(\vec{r}, \dot{\vec{r}}, t)$ are known functions of its arguments and unknown function is $\vec{r}(t)$, the vector of position of the charged particle

$$m\ddot{\vec{r}} = e[\vec{E}(\vec{r}, t) + \dot{\vec{r}} \times \vec{B}(\vec{r}, t)] + \vec{\Phi}(\vec{r}, \dot{\vec{r}}, t). \quad (3.77)$$

This, main equation of the orbital method does not take into account the relativistic effects neither the dumped force of the radiation.

To Fermi acceleration we can come writing the equation for the changing of the kinetic energy of the particle in the laboratory referent system averaged over the ciclotronic rotation during the longitudinal moving

$$W = \frac{1}{2}mv^2 = \frac{1}{2}m(v_{\parallel}^2 + v_{\perp}^2). \quad (3.78)$$

In the description of the motion of the charged particles in the stationary and homogeneous magnetic field it is possible to find one referent system (not always inertial) in which the trajectory of the particle is a circle, i.e. in which its motion is seen as a pure cyclotron rotation; the centre of this system moves along the line of the magnetic force with the constant velocity (equal to the component of the velocity of the particle along the magnetic

line of force). The motions for which is possible find this kind of the referent system are called *drift motions* and the center of that system (the center of the cyclotron rotation at given moment) is called *leading center*. The velocity of the leading center in the laboratory referent system can be written as

$$\vec{V} = \vec{V}_{\parallel} + \vec{V}_{\perp}, \quad (3.79)$$

where $\vec{V}_{\parallel} = \vec{v}_{\parallel}$, the longitudinal component is equal to the longitudinal component of the particle velocity in the laboratory referent system, and $\vec{V}_{\perp} = \vec{V}_D$, the transversal component of its velocity is *the drift velocity*, the velocity with which the particle goes far from the magnetic line of force on which was staying previously. In the referent system connected to the leading centre the components of the particle velocity are

$$\vec{v}_{\parallel}^* = 0, \quad \vec{v}_{\perp}^* = \vec{v}_{\perp} - \vec{V}_D. \quad (3.80)$$

Using the referent system of leading center and averaging over the cyclotron rotation it is possible rewrite the kinetic energy as

$$\overline{W} = \frac{1}{2}m\overline{v_{\parallel}^2} + \overline{W_{\perp}^*} + \frac{1}{2}m\overline{V_D^2}, \quad (3.81)$$

where W_{\perp}^* is the kinetic energy in the referent system connected to the leading center ($\vec{v}_{\parallel}^* = 0$, then also longitudinal kinetic energy is zero. This kinetic energy changes with time due to the changing of the intensity of the magnetic field in the referent system connected to the leading center

$$\frac{dW_{\perp}^*}{dt} = M \frac{dB^*}{dt}, \quad (3.82)$$

$$\frac{dB^*}{dt} = \frac{dB}{dt} = \frac{\partial B}{\partial t} + (\vec{v} \cdot \nabla)B = \frac{\partial B}{\partial t} + (\vec{v}_{\perp} + \vec{V}_D) \cdot \nabla_{\perp} B + \vec{v}_{\parallel} \cdot \nabla_{\parallel} B. \quad (3.83)$$

After averaging over the cyclotron rotations the part with perpendicular velocity disappears and the changing of the complete kinetic energy with the time has following form

$$\frac{d\overline{W}}{dt} = \frac{d}{dt} \left(\frac{1}{2}m\overline{v_{\parallel}^2} \right) + \frac{d\overline{W_{\perp}^*}}{dt} + \frac{d}{dt} \left(\frac{1}{2}m\overline{V_D^2} \right). \quad (3.84)$$

Using the fact that the changing of the longitudinal velocity is [86]

$$m \frac{d\vec{V}_{\parallel}}{dt} = \vec{F}_{\parallel} - M \nabla_{\parallel} B + m \vec{V}_{\parallel} (\vec{V}_D \cdot \frac{\nabla_{\perp} B}{B}), \quad (3.85)$$

and that the changing with time of the general form of the drift velocity is

$$m \frac{d\vec{V}_D}{dt} = \vec{F}_\perp + e(\vec{V}_D \times \vec{B}) - M \nabla_\perp B - 2 \frac{W_\perp}{B} \nabla_\perp B, \quad (3.86)$$

and using the equations (3.82) and (3.83) the final equation for the changing of the kinetic energy (averaged over the cyclotron rotations) with the time is

$$\frac{d\bar{W}}{dt} = M \frac{\partial B}{\partial t} + \vec{v}_\parallel \cdot \vec{F}_\parallel + \vec{V}_D \cdot \vec{F}_\perp. \quad (3.87)$$

From this equation it is easily to see that the changing of the kinetic energy of the particle is due to the induction of the nonstationary magnetic field (betatronic acceleration) through first term and due to the power of all nonmagnetic forces during the drift motion of the particle (through the other terms).

The *Fermi acceleration* is special case of this general formula when the changing of the magnetic field is the consequence only of the *motion of the static configuration* of the magnetic field with respect to the laboratory referent system.

Second order Fermi mechanism could be explained equivalently using the Lorentz transformations explicitly and the fact that velocity of the particle in the rest frame of the cloud is unchanged. We will not write down now these relatively simple equations.

Once the energy changing is found, it is one step to construct the Fokker-Planck equation (see [172]). On the other side is not trivial to show that this equation can be seen as a isotropic diffusion equation in the momentum space (see [172] and references inside, specially the work of Tverskoi). This is the crucial result for the treatments of reacceleration usually done in the literature.

As we already emphasized in the introducing part of this chapter, thermodynamics imply that the energy of the particles should tend towards the mean energy of the turbulent motions in the interstellar clouds; in the average particles will be accelerated, as the detailed balance imply that there are more head-on collisions (where the energy of the particle is gained) with respect to overtaking ones (where the energy of the particle is lost). This gave rise to a remarkable conclusion that reacceleration by the Fermi mechanism could be regards as a simple diffusive process (even more – isotropic) in the phase space. The mathematics of the diffusion process in plasma is relatively complicated and any deduction would be very long to be putted in

this thesis. We will give in the next sections results, that could be found in standard textbooks, like [86, 172, 93, 137].

3.4 Short History of Propagation Models and Basic Assumptions About the Propagation Processes

Leaky Box Model

One of the first commonly used models for the cosmic rays propagation is the leaky box approximation [129] in which one the Galaxy is uniformly filled with energetic particles trapped for a long time. The escape of the particles from the Galaxy is determined mostly by diffusion (leakage). The escape probability is small, but different from zero. The propagation is defined by the single number, the mean of the path length distribution.

Secondary cosmic rays are produced when primary cosmic rays collide with interstellar matter as the primaries diffuse from their sources through the turbulent magnetic fields of the Galaxy. Their spectra near the Earth depend from the spectra of primary nuclei, following propagation processes in the Galaxy and, finally, from the heliospheric modulation. The propagation equation could be obtained from the stationary solution of the continuity equation. For general secondary density per unit of energy $N_s(E, \vec{r})$ we have

$$\begin{aligned} \frac{\partial N_s}{\partial t} &= 0 = Q_s(E, \vec{r}) \\ -\nabla \cdot [(\vec{u} - D\nabla)N_s(E, \vec{r})] &+ \frac{1}{\tau_i}N_s(E, \vec{r}) \\ &- \frac{\partial}{\partial E}[b(E)N_s(E, \vec{r})], \end{aligned} \quad (3.88)$$

where $Q_s(E, \vec{r})$ is the total production rate of secondary particles, and can be written as

$$Q_s(E, \vec{r}) = 4\pi \int \frac{d\sigma_{P \rightarrow s}(E, E')\rho(\vec{r})}{dE < m >} J_P(E', \vec{r})dE', \quad (3.89)$$

where $J_P(E, \vec{r})$ is the flux of primary nuclei at position \vec{r} in the Galaxy, frequently assumed to be uniform (for the mechanisms of the production of primaries see the previous section of this thesis). For the spatial part of the distribution there were assumed different models during the development of the field. In [117] and other earlier papers there were assumed homogeneous

spatial distributions of the primary nuclei, at least in the Galactic disk. Measurements of Galactic γ rays suggested the hypothesis of radial distribution of cosmic rays. This distribution is needed in order to be able to evaluate the resulting γ emissivity at different galatocentric locations [107, 169]. Also, knowing (at least the present picture is like that) the mechanisms of cosmic rays production and the distributions of supernovae and pulsars (there are roughly radial), it is easy to derive this conclusion. For the detailed discussion of the necessities for the specific distributions usage see [167, 168] as well as the further discussion in this thesis. The presence of the spiral arms in the Galaxy also induce the angular dependence of (the sources of) cosmic rays distribution. This is taught to produce a very small effect on the final spectra detected in the Solar system. This also could influence the Galactic magneto-hydrodynamic properties, another effect being neglected in all the studies done up to now.

On the other side, the interstellar matter density $\rho(\vec{r})$ drops off outside of the disk, and diffusion occurs in a region that includes both the gaseous disk and some part of the halo. Here it was roughly and schematically assumed $\langle m \rangle$ as the average of an interstellar atom mass. Naturally, hydrogen and helium nuclei are the most important part of the interstellar media. The incoming cosmic rays can interact with them. These nuclear reaction are often called spallations. Details about the interstellar matter distribution will be given further in the text when we will describe the models that we used, also for the distribution of cosmic rays.

The same $\rho(\vec{r})$ and $J_P(E, \vec{r})$ are used in the calculation of both secondary nuclei and antiproton spectra, with the main difference that for the secondary nuclei only the primaries with the atomic numbers greater than those of the relevant secondaries are used.

Reaction cross sections in the last equation are giving the probability that a primary nucleus of energy E undergoes a nuclear reaction with an interstellar nucleus from the Galactic gaseous disk. As a curiosity we will note that the rough estimation of the ratio of the hydrogen, helium, C,N,O and iron is: H : He : C N O : Fe \approx 10 : 1 : 0.1 : 0.01.

The second term in the equation 3.88 that contains diffusion coefficient D and convection velocity \vec{u} is the secondary loss rate due to the diffusive and convective flows out of the Galaxy. The fundamental characteristic of the leaky box model is that those two terms are replaced with

$$\frac{N_s(E)}{\tau_e}, \quad (3.90)$$

where the characteristic time τ_{escape} is the mean escape time from the "box" region, without taking care of the details of the movement of the

particles in the Galaxy.

The third term on the right-hand side of equation 3.88 represents the loss due to inelastic collisions with characteristic time $\tau_{inelastic}$. This gives rise to the so called tertiary contribution in the case of the antiproton spectra included only relatively recently, due to the relatively small distortion of the spectra that they produce. Tertiary contributions are not so important here due to the fact that residence time in the box τ_e is much smaller than the interaction time τ_i but they become important in the framework of closed Galaxy models (see later in the text). These processes are tending to flat the antiproton spectra transferring the high energy particles in the lower energy part of the spectra. This kind of cross sections are studied in [114].

Finally, the last term in equation 3.88 is the energy gain and loss term due to the plasma scattering, ionization and reacceleration. $b(E)$ is the average of rate of secondary' energy change at energy E . Reacceleration in the framework of various modifications of the leaky box model was often neglected. The first to point out its importance, or, better to say, to start to use earlier theoretical results in their own propagation models, were Simon, Heinbach and Koch [170] in 1987., see also in [104]. This opened a new era also because the more powerful computers were build in those years, and a calculation times, even for this kind of models with requesting-of-processor-time processes, were reduced to acceptable ones. The model from [104] we will treat soon, immediately after this section dedicated to "standard" leaky box model.

Antiproton spectra are specially interesting for the testing of the propagation models [117] and they are important for the study of the eventual exotic components, so it is not surprising that the number of authors where trying first to produce antiproton spectra in accordance with the data. For this purpose even the very simple models were satisfying. They were even giving a relatively good estimations for the spectra and ratios of some other nuclei. But, the necessity of producing as correct as it is possible all the components of the cosmic rays (also leptons and gamma) was forcing the development of various models and numerical algorithms implemented in various codes for the simulation of the propagation. For the moment let us concentrate to the simplest antiproton production.

Quasi steady state equilibrium equation in the framework of the leaky box model (see also [137, 114]) in the case of antiprotons is containing simply the escape mean length Λ_e , antiproton annihilation mean length $\Lambda_{\bar{p}}^{tot.inel.}$, ionization loss rate I and total production rate of antiprotons $Q_{\bar{p}}$, and it is of the form

$$\frac{N_{\bar{p}}}{\Lambda_e} + \frac{N_{\bar{p}}}{\Lambda_{\bar{p}}^{tot.incl.}} + \frac{d}{dE_{\bar{p}}}(IN_{\bar{p}}) = Q_{\bar{p}}. \quad (3.91)$$

For the calculation of the average of ionization loss rate see also [137] where the result is explicitly obtained.

The energy spectra of primaries are important for the production of the antiprotons. Even the small change of the primary proton spectra index could produce the significant uncertainty in the antiproton spectra as it is pointed out in [117]. But, at least, only the high energy protons can produce even low energy antiprotons, as the threshold energy is relatively high. So, significant contributions in the antiproton spectra are coming from the protons that have energies of about 10 GeV, where the primary spectra index in the power law is known well, and there are no significant uncertainties due to the Solar modulation. Another kinematic effect for the antiproton production is that there are a small fluxes of antiprotons at small energies [171]. In fact, it can be seen in figure 3.1, where the differential fraction of antiprotons at energy $E_{\bar{p}}$ produced by primary protons of kinetic energy E_p are shown in six cases, that as the energy $E_{\bar{p}}$ of the produced antiproton decreases below 1 GeV kinetic energy, the mean proton parent energy needed for the production of a antiproton of energy $E_{\bar{p}}$ increases.

The escape length that governs the propagation of secondary cosmic rays (also for nuclei) can be determined by fitting the measured secondary to primary ratios of nuclei, that are affected the most during the propagation and, consequently, are the most sensitive quantities on the variation of the model parameters (as example, B/C or subFe/Fe ratios). A good fit to the high energy secondary abundances could be obtained by describing the path length as a power law in rigidity. This is consistent with the diffusion approach of [162]. One example of parametrization is from [163]

$$\Lambda_e = \Lambda \left(\frac{1}{1 + \frac{R_0^2}{R}} \right)^{n/2} R^{-\delta}, \quad (3.92)$$

where R is the rigidity in GV of the particle, and other constants should be obtained by fitting the data. R_0 is specially important parameter, as at the low rigidities (less than approximately 4 GV) the path length decreases, and, consequently, the escape mechanism becomes more convection instead of diffusion at those rigidities. For example, authors of [163] used $R_0 = 1.88GV$. Similar considerations in the framework of Galprop code will be assumed for some models in our calculations later on. Those are about the break in the index of diffusion spectra, taken at 4 GV for the diffusion plus convection model. Since the relation between the rigidity and energy per nucleon differs

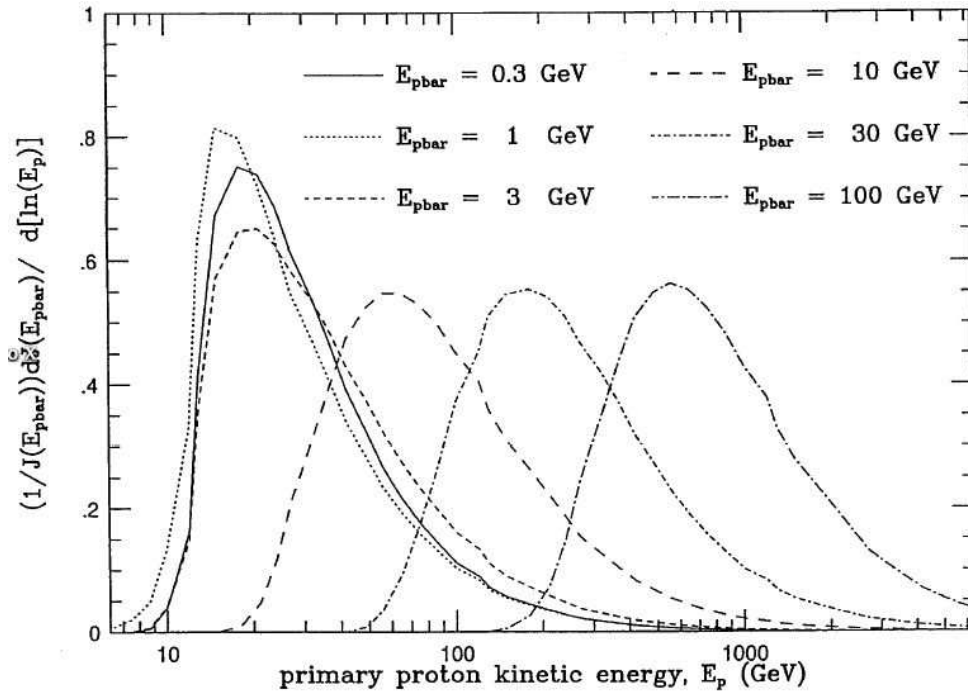


Figure 3.1: Fraction of antiprotons of energy $E_{\bar{p}}$ produced by primary protons of kinetic energy E_p . The threshold for antiproton production is apparent. Antiprotons with energies below 1 GeV must be produced with large backward momentum in the center of the momentum frame, and hence are mostly produced by high energy primaries. Figure is taken from [117].

significantly for secondary nuclei and particles with $Z = A$ (protons and antiprotons), while path length depends on rigidity, there must be introduced some corrections in the case of antiprotons (for details see [163])

$$\Lambda_e = \Lambda \left(\frac{\beta}{(4 - 3\beta^2)^{1/2}} \right)^n R^{-\delta}, \quad (3.93)$$

where β is velocity of the particle in the units of the speed of light. This correction is important just for the low energy particles, taking with itself the uncertainty of just less than 10% above 3GeV (see discussion in [117] and results of [165] and [163]). On the other side, at small energies it is hard to fit the data good due to the relatively big uncertainties of Solar modulation (see the section dedicated to Solar modulation in this thesis). For some earlier ideas of the same authors for this parametrization see [164]. In [117] the uncertainty of the antiproton production was estimated using the maximal uncertainty in average path lengths estimated as $\pm 35\%$ [166].

In the case of $\Lambda_e \rightarrow \infty$ we obtain the closed Galaxy model of [138]. Particularity of this case is that tertiary contributions become important due to the fact that residence time in the box τ_e is much bigger than the interaction time τ_i .

For the improvements of leaky box model see also [124]. For some latter works in its framework known as modified nested leaky box model or revised closed Galaxy model see [125, 126, 127, 128]. For the nonuniform Galactic disk model see [116]. For the leaky box model with reacceleration see [104].

3.4.1 Full Propagation Equation

Finally, we will write down the most complete equation for the propagation of cosmic rays that includes all the physical processes that were described in previous chapters:

$$\begin{aligned} \frac{\partial \psi(\mathbf{r}, p, t)}{\partial t} &= q(\mathbf{r}, p) + \nabla \cdot (D_{xx} \nabla \psi - \mathbf{V}_c \psi) + \frac{d}{dp} p^2 D_{pp} \frac{d}{dp} \frac{1}{p^2} \psi \\ &\quad - \frac{\partial}{\partial p} \left[\dot{p} \psi - \frac{p}{3} (\nabla \cdot \mathbf{V}_c) \psi \right] - \frac{1}{\tau_f} \psi - \frac{1}{\tau_r} \psi. \end{aligned} \quad (3.94)$$

where $\psi(\mathbf{r}, p, t)$ is the total phase space density. This equation is valid for all the types of particles. We will shortly repeat the main characteristics of the physical processes in this equation, also with some of the assumptions about them made in the literature or adopted in the propagation code Galprop that we were using (for more details about the code see the section 3.6).

Isotropic diffusion is defined by the coefficient that depends from rigidity (momentum per unit of charge, $\rho = \frac{p}{Z}$)

$$D_{xx} = \beta D_0 (\rho/\rho_0)^\delta, \quad (3.95)$$

inspired by the Kolmogorov spectrum ($\delta = 1/3$) of the weak magnetohydrodynamic turbulence. In [104] was first shown that the Kolmogorov spectrum best reproduces the sharp peak in B/C data. In some models we have used a break in the index δ at some rigidity ρ_0 , with a value $\delta_1 = 0$ below the reference rigidity ρ_0 (see the discussion about the path length as a power law in rigidity in the section about the leaky box model).

The convection velocity field \mathbf{V}_c , that corresponds to the Galactic wind, has a cylindrical symmetry. Its z-component is the only one different from zero. It increases linearly with the distance z from the Galactic plane ($V_c > 0$ for $z > 0$, $V_c < 0$ for $z < 0$ and $dV_c/dz > 0$ for all z). This is in agreement with magnetohydrodynamical models [101]. In the Galactic plane there should be no jump of the convection velocity and so we considered only $V_c(z = 0) = 0$.

Reacceleration is determined by the diffusion coefficient for the impulse space D_{pp} . D_{pp} is a function of the corresponding configuration space diffusion coefficient D_{xx} and of the Alfvén velocity V_A in the framework of quasi-linear MHD theory [99, 100, 93]

$$D_{pp}(D_{xx}, V_A) = \frac{4p^2 V_A^2}{3\delta(4 - \delta^2)(4 - \delta)w}, \quad (3.96)$$

where w characterizes the level of turbulence, and is equal to the ratio of MHD wave energy density to magnetic field energy density. $w = 1$ is assumed [100]; in any case, only the quantity V_A^2/w is relevant.

Ofcourse, Alfvén velocity and convection velocity gradient in Milky Way for reacceleration and convection terms are unknown parameters of propagation (there are no other sources of information from which we could extract them, except the spectra of cosmic rays) and their possible range will be constrained by the analysis of fits of suitable data. The same procedure is valid for constraining the height of the galactic halo and some of the other unknown parameters. This will be analyzed further in order to obtain all the possible spectra of antiprotons and positrons using the sets of the constrained parameters.

Injected spectra of all primary nuclei are power laws in impulse

$$dq(p)/dp \propto p^{-\gamma}, \quad (3.97)$$

where the value of γ can vary with species, in principle. This power law approximation has been shown to be allowed in the framework of diffusive shock acceleration models (see the section about the creation of cosmic rays), as well as a small break in the injection indexes γ [102, 106].

Source term $q(\mathbf{r}, p)$ for secondaries contains cross sections for their production from progenitors on H and He targets

$$q(\vec{r}, p) = \beta c \psi_p(\vec{r}, p) [\sigma_H^{ps}(p) n_H(\vec{r}) + \sigma_{He}^{ps}(p) n_{He}(\vec{r})], \quad (3.98)$$

where $\sigma_H^{ps}(p)$ and $\sigma_{He}^{ps}(p)$ are the production cross sections for the secondary from the progenitor on H and He targets, ψ_p is the progenitor density, and n_H, n_{He} are the interstellar hydrogen and helium number densities.

The last two terms in equation 3.94 are loss terms with characteristic times for fragmentation and radioactive decay.

For nucleon propagation in the interstellar matter the losses are mainly due to ionization, Coulomb scattering, fragmentation and radioactive decay. For electrons the important processes are ionization, Coulomb scattering, bremsstrahlung in the neutral and ionized medium, as well as Compton and synchrotron losses. These processes are well known and their description and the formulae can be found in the standard literature like [137] and [86] while very transparent review with the complete literature is given in [98], where also are given the references for the fragmentation cross sections.

3.5 Heliospheric Modulation of the Local Interstellar Spectra

The heliospheric modulation of the local interstellar spectra in the vicinity of the Earth and in the hole heliosphere has to be taken in account in order to obtain the realistic cosmic rays spectra in locations where they are/will be measured (balloon-born or satellite borne experiments). Also, the effect of the higher atmospheric layers should be included in the case of balloon-borne experiments, but this effect is out of the scope of this thesis, and it is small. Here, we will give the brief general treatment of the Solar modulation near the Earth and the treatment in the framework of the approximation that we were using.

3.5.1 Solar Wind and Solar Modulation

Strictly speaking, the phenomena of distortion of the interstellar spectra in the heliosphere could be treated as well as any other system in plasma physics

or, better to say, in high energy astrophysics – with a separate propagation equation that should contain parameters like the Solar magnetic field, fluxes of ejected particles, etc. This equation should describe the dynamic of all the charged particles in presented magnetic fields and it would be very difficult to solve it, even numerically (see, for example, [155, 109, 108, 110]).

First, let us consider for the moment the dynamic of charged particles in the fixed stationary dipolar magnetic field. This simple example is very instructive and important also for the study of the Solar wind and Solar modulation, due to the similar distribution of the magnetic field. Separately, it is important for the study of detection of cosmic rays at predefined or variable positions in the Earth's magnetic field. This case is much simpler from the case of the Solar wind, because magnetic field distribution is fixed and known to be, roughly speaking (see further), dipolar and there are no high energy ejected particles that would also produce their own magnetic field, influencing like that the external magnetic field, as well as the movement of all the presented particles, and so on and so forth, and implying like that the full selfconsistent hydrodynamical treatment of the plasma. Earth's magnetic field is influencing on the number of the particles coming at the defined geomagnetic latitude. So, at high latitudes (near the Earth's magnetic poles) one should expect higher fluxes, while near the geomagnetic equator the fluxes are lowered due to the fact that the particles have to pass transversally through the magnetic field lines, and so they can not simply drift along the lines, but they will have to deflect. For a review of this system see, for example, dedicated chapter in [155] and references therein, for drift approximation in general see [86] or any other standard textbook on plasma physics, like [137].

Now, one can extend spatially this system – here enters the effect of the Sun on the interstellar fluxes of incoming cosmic rays. This problem is often treated separately from the entering of the particles in the Earth's magnetic field neglecting the intermediate effects. The Earth's magnetic field is, unfortunately, dipolar just within a few Earth's diameters, and consequently the simple treatment of adiabatically separated dynamics of the incoming fluxes is valid just relatively near the Earth. Out of that region the magnetic field distribution is highly influenced by the outflow of the hot plasma from the Sun. This phenomena is known as the Solar modulation of incoming interstellar fluxes with Solar wind particles. It can be shown that this is of the big importance for the particles that are observed at the top of the atmosphere. The heating of the Solar coronal gas is probably driven by the hydromagnetic waves or shock waves. For the hot plasma in the gravitational field of the Sun it can be shown that there must be a general outflow of the material from the Sun – known as the Solar wind. Those calculations were done in

Table 3.1: Typical parameters of the Solar wind during the small Solar activity period

Average of the particles velocity	$350 \frac{km}{s}$
Particles flux	$1.5 \times 10^{12} \frac{1}{m^2 s}$
Particles concentration	$10^7 \frac{1}{m^3}$
Energy of single proton	500 eV
Energy density of protons	$4 \times 10^{-10} \frac{J}{m^3}$
Average temperature	10^6 K

the framework of the magnetohydrodynamical approach (see, for example, [86]). To demonstrate better the effects of these processes here we give the table 3.1 with some of the most important characteristics of the Solar wind fluxes.

Of course, these parameters can vary depending of the Solar activity. Years after the Solar wind is detected and theoretically predicted, it is still an open problem to make a model of Solar wind influence on the cosmic rays that are coming from the local interstellar regions that could give better results for the period of the maximal Solar activity. Even for the "small" Solar modulation, still there are debates about the models. One should also take into account the polarity of the Solar magnetic field during the 22 years long Solar cycle. The polarity reverses when the Solar activity is maximum; the positive and the negative particles drift in opposite directions, taking different routes to arrive at the Earth. These kind of improvements of standard calculations are out of the scope of this thesis. For detailed treatment of the both see recent article [110] as well as standard treatments [109, 108].

The phenomenon of Solar modulation could be illustrated the best by the inverse correlation between the intensity of the fluxes of the cosmic rays at the top of the atmosphere and the level of the Solar activity, that is measured by the number of the Sun spots observed between heliocentric latitudes of $\pm 45^\circ$. In addition to that, there is the total correlation between the relative Sun spot number and the local degree of turbulence in the geomagnetic field. The greater level of the Solar activity is, the Solar wind is more effectively preventing the interstellar fluxes of cosmic rays from reaching the Earth.

3.5.2 Force Field Approximation

We have made use of a widely used and tested model in which the transport equation is solved in the force field approximation [108, 109]. That equation describes diffusion processes in the heliosphere and includes effects of heliospheric magnetic field and Solar wind. In this case, Solar modulation is a function of just a single parameter that describes the strength of the modulation. All the dynamical processes are simulated with relatively simple changing of the interstellar spectra during the propagation inside the heliosphere, described by the formula

$$\frac{\Phi^{toa}(E^{toa})}{\Phi^{is}(E^{is})} = \left(\frac{p^{toa}}{p^{is}}\right)^2, \quad (3.99)$$

$$E^{is} - E^{toa} = |Ze|\phi, \quad (3.100)$$

where E and p are energies and impulses of the interstellar and top of the atmosphere fluxes and ϕ is the unique parameter that determines the Solar modulation.

In brief, one generalization of the above equation can be obtained from the transport equation (here written directly in coordinate-dependent form, in spherical coordinates) for the Galactic cosmic rays in the heliosphere (for the spherically symmetric steady state case)

$$\frac{1}{r^2} \frac{\partial}{\partial r} (r^2 \kappa \frac{\partial f}{\partial r}) - V \frac{\partial f}{\partial r} + \frac{1}{r^2} \frac{\partial}{\partial r} (r^2 V) \frac{P}{3} \frac{\partial f}{\partial P} = 0, \quad (3.101)$$

where f is the distribution function of particles in the phase space averaged over particles directions, P is rigidity, κ is the diffusion coefficient, r is the heliocentric radial distance and $V \approx 400 \frac{km}{s}$ is radial Solar wind velocity. A force field approximation would be

$$\frac{\partial f}{\partial r} + \frac{PV}{3\kappa} \frac{\partial f}{\partial P} = 0, \quad (3.102)$$

and it is argued in [108] that it is valid above high enough energies. This equation can be solved easily [173] in the framework of quasilinear theory for high energies where

$$\kappa = A\beta P, \quad (3.103)$$

for $P > P_c$ (see [118]) and also at low energies in which case by following the observations of Solar wind particles it is valid that

$$\kappa = A\beta P_c, \quad (3.104)$$

for $P > P_c$ (see [174]), where $P_c = 1GV$. The solution for $P_r < P_c$ is given by

$$E = P_c \ln \frac{P_r + E_r}{P_c + E_c} + E_c + \frac{(R - r)V}{3A}, \quad (3.105)$$

while for $P_r > P_c$ is given by

$$E = E_r + \frac{(R - r)V}{3A}, \quad (3.106)$$

and it is relating the total energy at the heliospheric boundary $E = (P^2 + T_0^2)^{0.5}$ with the energy E_r and rigidity at distance r (R is the distance of the heliospheric boundary). One can define the strength of the Solar modulation

$$\phi = \frac{(R - 1AU)V}{3A}, \quad (3.107)$$

here the unique parameter that is characterizing the Solar modulation of local interstellar spectra near the Earth.

The force field approximation works excellent, for example, for the antiproton energies above few hundreds of MeV and should be not used for the energies less than 100MeV. Frequently, for all the energies is used just the theoretically induced form of diffusion coefficient in the framework of quasi-linear modeling of plasma (for general discussions see the book [86]) due to the it's simplicity and not so big errors.

The uncertainties of this model [161] for the Solar modulation are not very big, even it's simplicity. In the domain from one to few hundreds of MeV the uncertainties are of the order of ten percent for antiprotons, for example, while their are decreasing rapidly for the higher energies. Additional uncertainties are coming from not calculated charged drift effect. This effect is the most evident during the period of the minimal Solar activity; modulation will be different for protons and antiprotons, for example (see [110, 2, 3, 4]). But, these errors, for example, for antiproton to proton ratio should be less than 10% around few hundreds of MeV, already (see [5]). These uncertainties are also decreasing with an increasing of the Solar modulation parameter.

3.6 Propagation of the Background Component of Cosmic Rays in the Milky Way and Its Uncertainties

We have chosen Galprop (see [98, 103, 105] and references therein) as a public code for the treatment of the propagation of the standardly produced parts of all cosmic rays together. In this public code there is a possibility to change the parameters for different models and, ofcourse, to add personal changes to the code. At the first place, our scope has been to determine the total uncertainties in the calculation of positron and antiproton top of the atmosphere spectra as the consequence of the uncertainties of geometrical and hydromagnetodynamical parameters of the Galaxy and nuclear cross sections, due to their importance in the search of the eventual signal in those antiparticles spectra, predicted in various theories, that could come from various dark matter candidates. Than, we wanted also to make the consistency check with the uncertainties of other cosmic rays species. First, we give a short description of Galprop code and models for primary sources, target densities of hydrogen and helium, method of numerical solving of the propagation equation and other most important characteristics of the code (based on [98], where all the details and other references can be found).

Galaxy is modeled as a three dimensional with cylindrical symmetry; coordinates are (R, z, p) , where R is Galactocentric radius, z is the distance from the Galactic plane, and p is the total particle momentum. The distance from the Sun to the Galactic centre is taken to be 8.5 Kpc. The propagation region is bounded by fixed $R_{max} \equiv R = 30$ Kpc and some $z_{max} \equiv z$ beyond which free escape is assumed. The range $z_{max} = 1 - 20$ Kpc can be considered since this is suggested by previous studies of radioactive nuclei [152] and the distribution of synchrotron radiation [154].

The atomic hydrogen distribution is given by

$$n_{HI}(R, z) = n_{HI}(R)e^{-\ln 2 \cdot (z/z_0)^2}, \quad (3.108)$$

where $n_{HI}(R)$ is taken from [10] and z_0 from [13]

$$z_0(R) = \begin{cases} 0.25 \text{ kpc}, & R \leq 10 \text{ kpc}; \\ 0.083 e^{0.11R} \text{ kpc}, & R > 10 \text{ kpc}. \end{cases} \quad (3.109)$$

The distribution of molecular hydrogen is taken from [9]

$$n_{H_2}(R, z) = n_{H_2}(R) e^{-\ln 2 \cdot (z/70 \text{ pc})^2}. \quad (3.110)$$

For the ionized gas is used the two component model from [11]

$$n_{HII} = 0.025 e^{-\frac{|z|}{1 \text{ kpc}} - \left(\frac{R}{20 \text{ kpc}}\right)^2} + 0.2 e^{-\frac{|z|}{0.15 \text{ kpc}} - \left(\frac{R}{2 \text{ kpc}} - 2\right)^2} \text{ cm}^{-3}, \quad (3.111)$$

where the first term represents the extensive warm ionized gas while the second one *HII* regions and is concentrated around $R = 4$ kpc. A temperature of 10^4 K is assumed to compute Coulomb energy losses in ionized gas.

In Galprop, the distribution of cosmic rays sources is chosen to reproduce (after propagation) the cosmic rays distribution determined by the analysis of EGRET gamma-ray data done in [107]

$$q(R, z) = q_0 \left(\frac{R}{R_\odot}\right)^\eta e^{-\xi \frac{R-R_\odot}{R_\odot} - \frac{|z|}{0.2 \text{ kpc}}}, \quad (3.112)$$

where q_0 is a normalization constant and η and ξ are parameters; the R -dependence has the same parameterization as that used for supernovae remnants in [156], but there are adopted different parameters in order to fit the gamma-ray gradient. A cutoff in the source distribution at $R = 20$ kpc is applied, since it is unlikely that significant sources are present at such large radii. The z -dependence of q reflects the assumed confinement of sources in the disk. In the code is assumed that the source distribution of all cosmic ray primaries is the same.

Code first compute propagation of primaries, giving the primary distribution as a function of (R, z, p) . Then, the secondary source function is obtained from the gas density and cross sections. Finally, the secondary propagation is computed.

For the numerical solution of the propagation equation is used Crank-Nicholson implicit method [157]. The diffusion, reacceleration, convection and loss terms are finite-differenced for each dimension (R, z, p) . The three spatial boundary conditions

$$\psi(R, z_{max}, p) = \psi(R, -z_{max}, p) = \psi(R_{max}, z, p) = 0 \quad (3.113)$$

are imposed at each iteration. No boundary conditions are imposed or required at $R = 0$ or in p . Grid intervals are typically $\Delta R = 1$ Kpc, $\Delta z = 0.1$ Kpc while for p a logarithmic scale with ratio typically 1.2 is used.

Processes included in Galprop code are all from the propagation equation 3.94, and it is possible to make the search in all the parameter space simultaneously. But, as we will see later, we will be constrained to turn off some of the physical processes during the propagation, by setting the constants that determine them to zero, obtaining like that two models of propagation, one without convection and other without reacceleration.

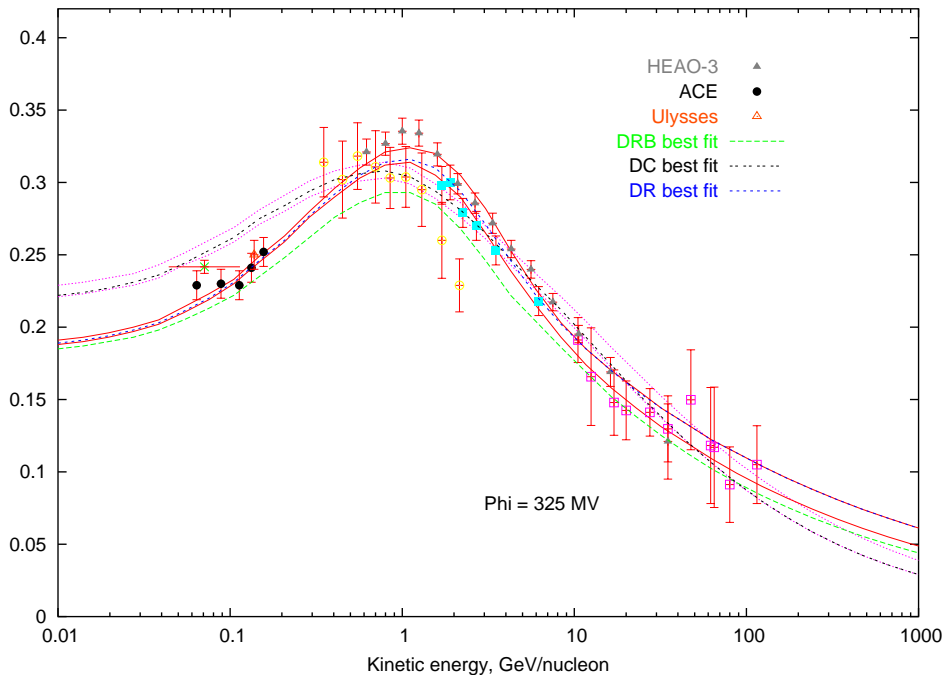


Figure 3.2: Propagation parameters uncertainty for B/C ratio: DR model is given with red solid lines, while DC model with violet dotted lines. The best fit for DR model is represented by blue dashed line, for DC model with black dashed line and for DR model with a break in the injection index for the primary spectra best fit is given with dashed green line. For the complete list of the experimental data see [147].

Many magnetohydrodynamical parameters in the propagation equation are free (they can not be extracted from the other sources) and must be constrained by the cosmic ray fluxes experimental data (that always take with themselves errors), as we already emphasized in previous sections: cosmic ray spectra are the only one probe for the magnetohydrodynamics of our Galaxy. As the first step in our work, we were interested to find the uncertainties of the propagation parameters due to this procedure of parameters determination and other reasons that we will present in this section.

The second source of the cosmic rays spectra uncertainties are the uncertainties of the nuclear cross sections. These we will include after, by seeing how the upper and the lower propagation parameters uncertainty bands are changing due to the cross sections uncertainties.

Some other not exactly known parameters in the Galaxy, that could be

estimated from the other sources than the spectra of cosmic rays, like the ratio of hydrogen and helium in the Galaxy, are also influencing on the propagation and are taking with themselves a part of the total uncertainty of cosmic rays spectra. Similar attempts for the determination of the uncertainties of the antiproton spectra were already done (see [27]).

As we already said in the beginning of this section, we were constrained to consider, for the final analysis, models with or without reacceleration or without convection. We tried a great number of times to obtain models that reasonably fit the experimental data with all the physical processes switched on, but the results were negative. We did search in a few attempts, for more than a month of processor time on a standard machine, and, unfortunately, we were forced to continue the work without both of the physical processes turned on simultaneously; even if that is theoretically expected, at least weak effects of any one of the processes. But, the answer could be that one of the processes is really so marginal in the Galaxy that data require just reacceleration or just convection to be fitted well. Until the cosmic ray spectra are the only one probe for the magnetohydrodynamics of the Galaxy, this will remain uncertain; at least with the present measurements energy ranges. So, we found the uncertainties of the two extreme cases of propagation models (see [98, 103]). In the first model are included diffusive and reacceleration effects (DR model, see previous sections and propagation equation in the Galaxy 3.94). The second model contains diffusion and convection terms from the same equation 3.94 (DC model). In this model are presented two breaks – in the index of the primary injection spectra (i.e. at some rigidity ρ^γ the index γ suffers a discontinuity, see equation 3.97), justified in [106], and break in the spectra of diffusion coefficient D_{xx} (i.e. at some rigidity ρ_0 the diffusion index δ suffers a discontinuity, see equation 3.95), see discussion in [103] and discussion in the section about the leaky box model. For DR model we considered two subcases: without the break in the index of primary injection spectra and with the break at the rigidity of ρ^γ (see [106]; this break is always present in the second model).

Secondary to primary CR ratios are the most sensitive quantities on variation of the propagation parameters. This is easy to verify directly, using any propagation code, but is also easy to understand. In fact, the primary to primary ratios are not so sensitive on changing of propagation parameters due to similar propagation mechanisms. The same is valid for secondary to secondary ratios. The most accurately measured secondary to primary ratio is boron to carbon ratio (B/C). B is secondary while, one of its progenitors, C is primary. The B/C data are used also because they have relatively well known cross sections. To estimate the quality of the data fit we have used a standard χ^2 test

Table 3.2: Allowed values for diffusion and reacceleration model propagation parameters.

par./val.	$z[Kpc]$	$D_0[cm^2s^{-1}]$	δ	γ	$v_A[Kms^{-1}]$
minimal	3.0	$5.2 \cdot 10^{28}$	0.25	2.35	22
best fit	4.0	$5.8 \cdot 10^{28}$	0.29	2.47	26
maximal	5.0	$6.7 \cdot 10^{28}$	0.36	2.52	35

$$\chi^2 = \sum_n \frac{1}{(\sigma_n^{B/C_{exp}})^2} (\Phi_n^{B/C_{exp}} - \Phi_n^{B/C_{teo}})^2. \quad (3.114)$$

For the analysis of the uncertainty in the Galprop generated cosmic ray spectra induced by propagation parameters uncertainties, first we treated DR model without the break in the index of the primary injection spectra. We have chosen just the most important geometrical and hydromagnetodynamical propagation parameters of this model to be varied: the height of the Galactic halo, z , constant in the diffusion coefficient from equation 3.95 D_0 , index of the diffusion coefficient from the same equation δ , primary spectra injection index for all the energies from the equation 3.97 γ and Alfvén velocity v_A that determines the strength of reacceleration. In principle, one could vary also some other parameters, but as Galprop code is relatively slow (due to the relatively complex content of the propagation equation 3.94), the time necessary for one set of varied parameters is relatively big (of the order of an hour), and the variation of bigger number of parameters would be very difficult. For the variation of the cited parameters of DR model we have required the reduced χ^2 less than 2 for the fit of the B/C experimental data from [147], see also figure 3.2. In that figure are presented the enveloping curves of all the good fits with solid red lines around the best fit line for the same model, that is represented with dashed blue line. We have taken the experimental data with relatively small Solar modulation parameter ϕ between 325 MV and 600 MV, where the force field approximation is better justified than for the high modulation parameters (see the section about the Solar modulation). The allowed ranges of varied propagation parameters of this model are given in the table 3.2.

Using the allowed parameters we found, at the first place, the enveloping curves of all the positron and antiproton spectra obtained with those sets of parameters. Those enveloping curves present the upper and the lower bounds of the uncertainty bands for positron and antiproton spectra due

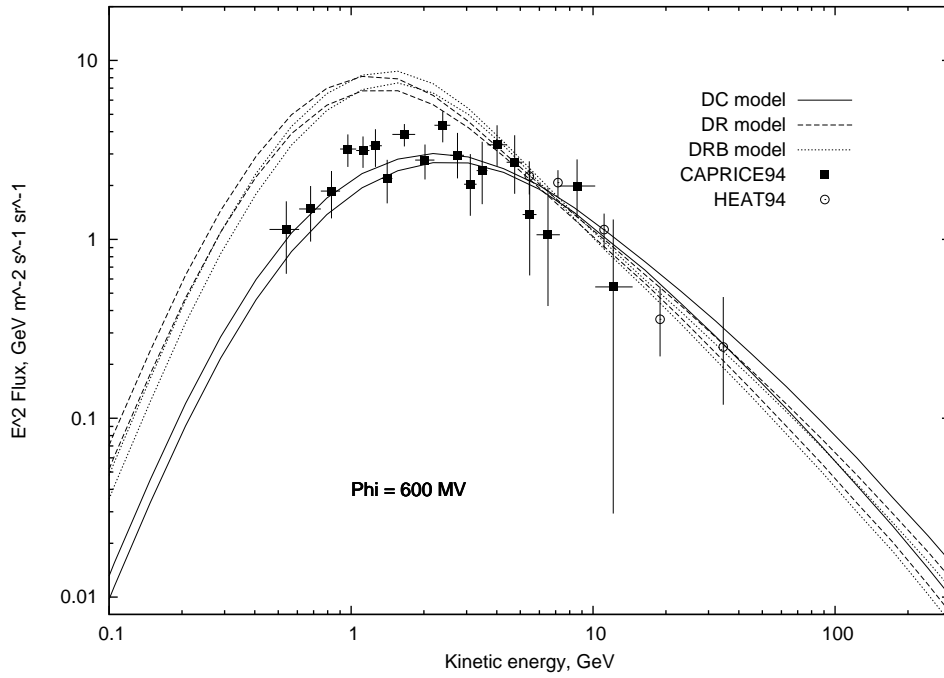


Figure 3.3: Upper and lower bounds of positron spectra due to the uncertainties of the propagation parameters for DC model are represented with solid lines, for DR model with dashed lines and for DRB model with dotted lines. The DR and DRB model uncertainties are very similar, but there is the slight improvement of the fit in the low energy part of the spectra in the case of DRB model. On the other side, around the maximum DRB model is overestimating the data slightly more than DR model. Experimental data are taken from [149].

Table 3.3: Allowed values for the propagation parameters for diffusion convection model.

par./val.	$z[Kpc]$	$D_0[\frac{cm^2}{s}]$	δ_2	$\frac{dV_C}{dz}[\frac{Km}{skpc}]$	γ_1	γ_2
minimal	3.0	$2.3 \cdot 10^{28}$	0.48	5.0	2.42	2.14
best fit	4.0	$2.5 \cdot 10^{28}$	0.55	6.0	2.48	2.20
maximal	5.0	$2.7 \cdot 10^{28}$	0.62	7.0	2.50	2.22

to the propagation parameters uncertainty, see figure 3.3 for the positron spectra uncertainty and figure 3.4 for the antiproton spectra uncertainty. The relative uncertainty is depending of the energy range of the spectra. For example, for positrons relative uncertainty is varying from 30% under 1 GeV to 15% around 10 GeV, increasing again after 10 GeV (figure 3.3) while for antiprotons is varying from about 10% up to about 15% (figure 3.4).

For better visibility all the black and white figures that contain positron and antiproton data will contain just the part of the experimental data chosen to cover more or less all the energy range reached in up to now experiments (see the Chapter 5 about the measurements of cosmic rays, where we will present also the experiments done up to now as well as the future experiment PAMELA and its expectations for the positron and antiproton background spectra), while all the data will be given at color figures. The data are taken from references [148, 149].

In the case of DC model, for the variation we have chosen parameters: D_0 , diffusion indexes δ_1 , below, and δ_2 , above the reference rigidity $\rho_0 = 4$ GV (all those parameters are from equation 3.95), halo size z , convection velocity V_c (from equation 3.94) and injection index for primary nuclei γ_1 below the reference rigidity $\rho_0^\gamma = 20$ GV and γ_2 above it (those parameters are from equation 3.97). Enveloping curves of B/C fits for the reduced χ^2 values less than 2.8 are given in figure 3.2. Positive variations around $\delta_1 = 0$ gave unsatisfactory fit. In order to take the smallest possible break of this index we have decided not to take negative δ_1 values. Allowed values for the propagation parameters can be found in table 3.3. Again, we used them to derive the uncertainties of positron and antiproton spectra. Relative uncertainty for positrons vary between 20% above the maximum and 30% below it (figure 3.3) while for antiprotons is about 20% around 20 MeV, 17% around the maximum and 25% around 20 GeV (figure 3.4).

We have found also the spectra that correspond to the parameters of the best fit of B/C data for subFe/Fe ratio (another important secondary to pri-

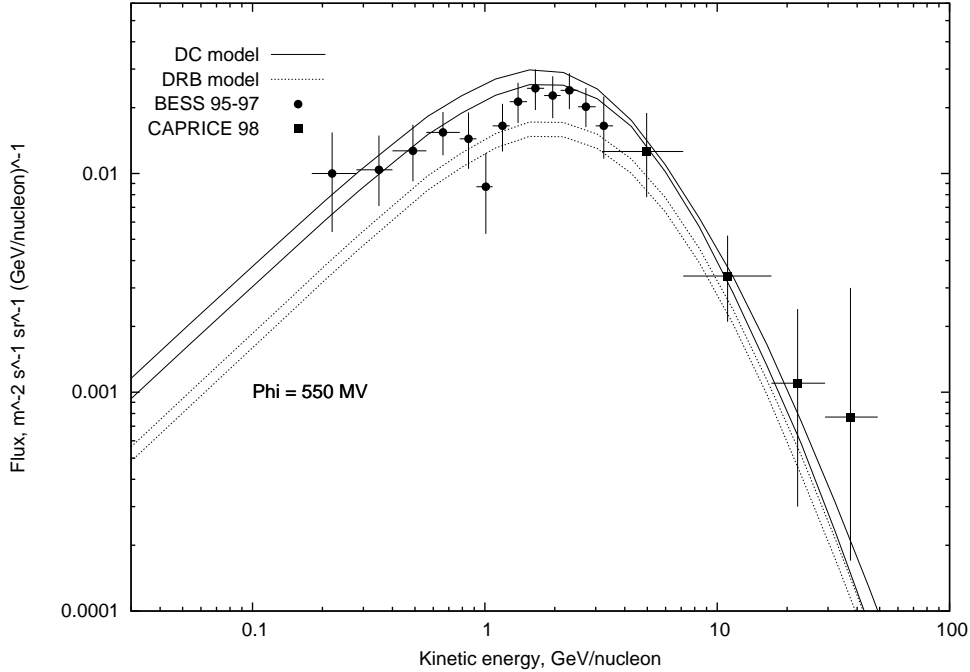


Figure 3.4: Upper and lower bounds of antiproton spectra due to the uncertainties of the propagation parameters for DC model (solid lines) and DRB model (dotted lines). The propagation parameters uncertainties for the DR model are almost the same as those of the DRB model (see the discussion later in the text), so we are not presenting them here to avoid the confusion. Experimental data are taken from [148].

Table 3.4: Allowed values for the propagation parameters for diffusion reacceleration model with break in the injection spectra of primary nuclei.

par./val.	$z[Kpc]$	$D_0[\frac{cm^2}{s}]$	δ	γ_1	γ_2	$v_A[\frac{Km}{s}]$
minimal	3.5	$5.9 \cdot 10^{28}$	0.28	1.88	2.36	25
best fit	4.0	$6.1 \cdot 10^{28}$	0.34	1.92	2.42	32
maximal	4.5	$6.3 \cdot 10^{28}$	0.36	2.02	2.50	33

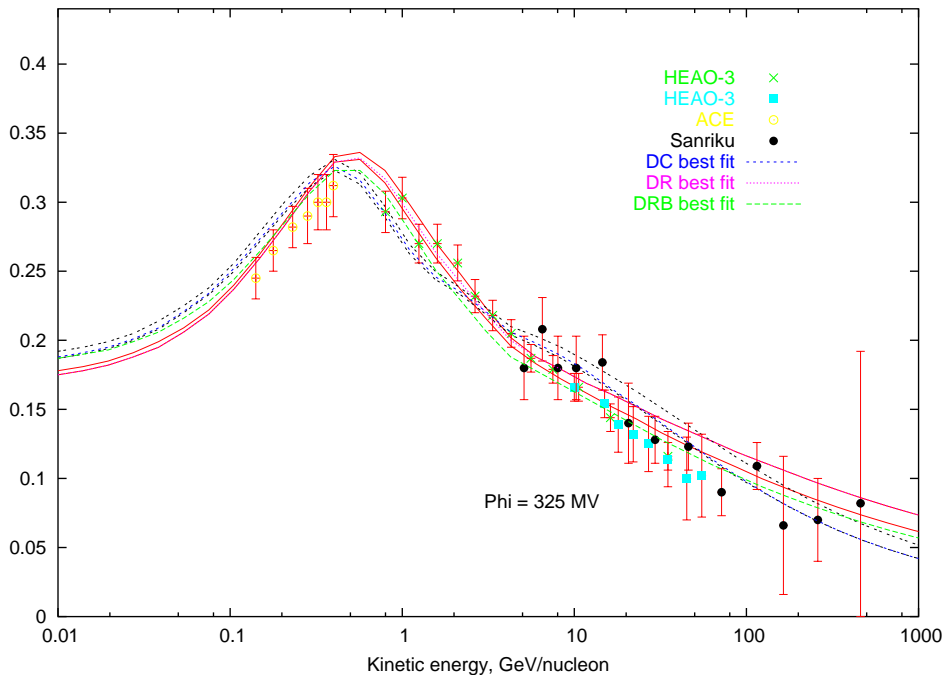


Figure 3.5: Ratios $(Sc+Ti+V)/Fe$ that correspond to the parameters of propagation for DC, DR and DRB model that gave the best fits of B/C data. The upper and the lower limits of all the graphics obtained with the parameters that give good fits of boron to carbon ratio are given for DC and DR model. Experimental data are taken from [151].

mary ratio for testing the parameters of the propagation models, figure 3.5), protons, helium and electrons as well as the corresponding propagation parameters uncertainties. For DC model fits are good, while DR overestimates protons (figure 3.9), helium (figure 3.8) and electrons (figure 3.6).

In order to improve those fits, we have considered also the DR model with a break in the injection index for the primary nuclei spectra taken at rigidity 10 GV [103, 106]. We determined the allowed values of the propagation parameters (table 3.4) demanding the same reduced $\chi^2=2$ as for DR model (see figure 3.2). The positron and antiproton uncertainties are presented in figures 3.3 and 3.4. Even if positrons are fitted a little bit better at low energies and also primary protons and helium are fitted better (see figure 3.9 and figure 3.8), all of them remain overestimated. The B/C fit is also disturbed a little. We would like to note here that some other reasons for errors in the B/C spectra (and for the problem with B/C ratio in the

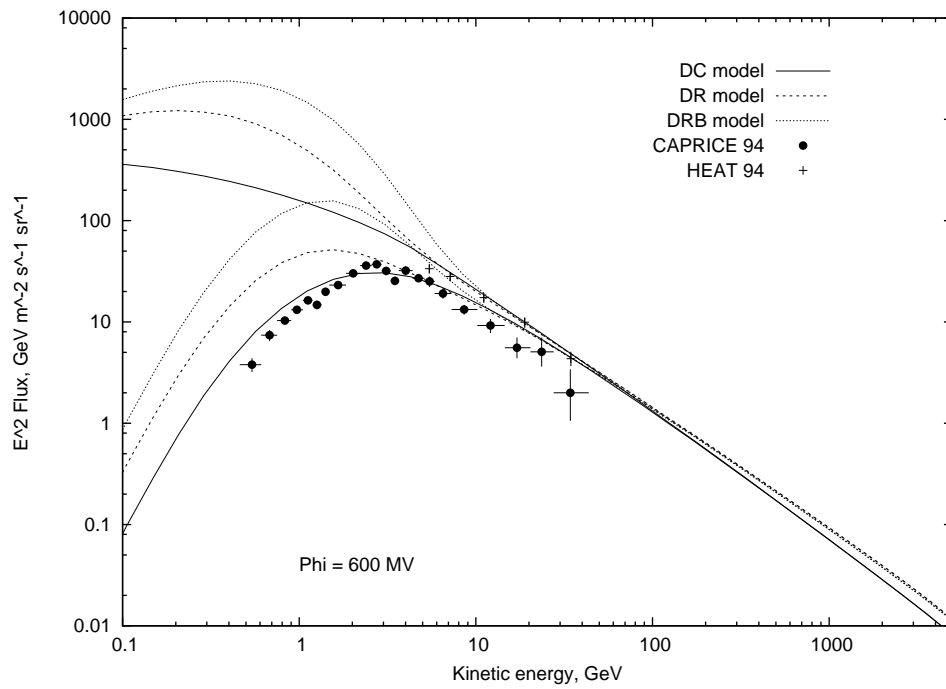


Figure 3.6: Top of the atmosphere spectra of electrons that correspond to the parameters of the best B/C fit are the lower curves: for DC model are given with solid line, for DR model with dashed line and for DRB model with dotted line. The local interstellar spectra are the upper curves; the three models are represented with the same types of lines. Experimental data are taken from [149].

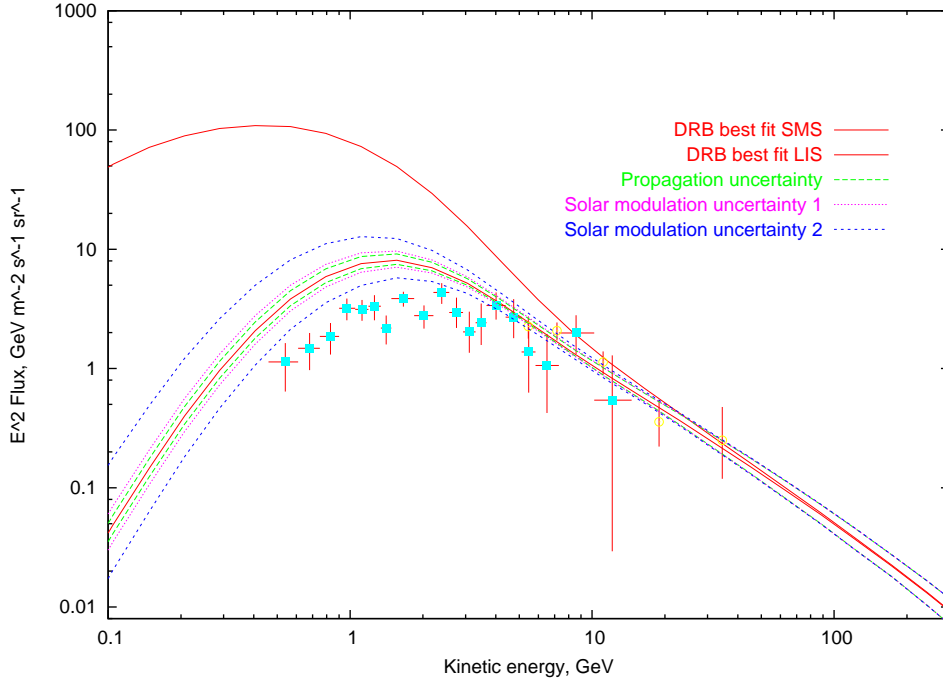


Figure 3.7: Top of the atmosphere (red lower curve) and local interstellar (red upper curve) spectra of positrons that correspond to the parameters of the best B/C fit for DRB model. Total uncertainties of positron fluxes are presented with green dashed lines around the best fit. Two enlargements of the propagation uncertainties due to two different Solar modulation uncertainties are presented with violet dotted and blue dashed lines (see the text for details). Experimental data are taken from [149].

case of DC model) could be presented also: due to the nuclear cross sections, the distribution of the gas in the Galaxy or due to the Solar modulation uncertainty. For example, for the computation of B/C ratio, Galprop uses only one principal progenitor and compute weighted cross sections based on the observed cosmic-ray abundances from [153]. For the case of Boron, the Nitrogen progenitor is secondary, but only accounts for $\approx 10\%$ of the total Boron production, so that the approximation of weighted cross sections was used. But, introducing the break in the index of primary injection spectra in DR model also make influence on electrons, that are now fitted even worst (see figure 3.6) than in the case without the break. On the other side, the antiproton spectra remain practically unchanged, still significantly and systematically underestimated in all the energy range.

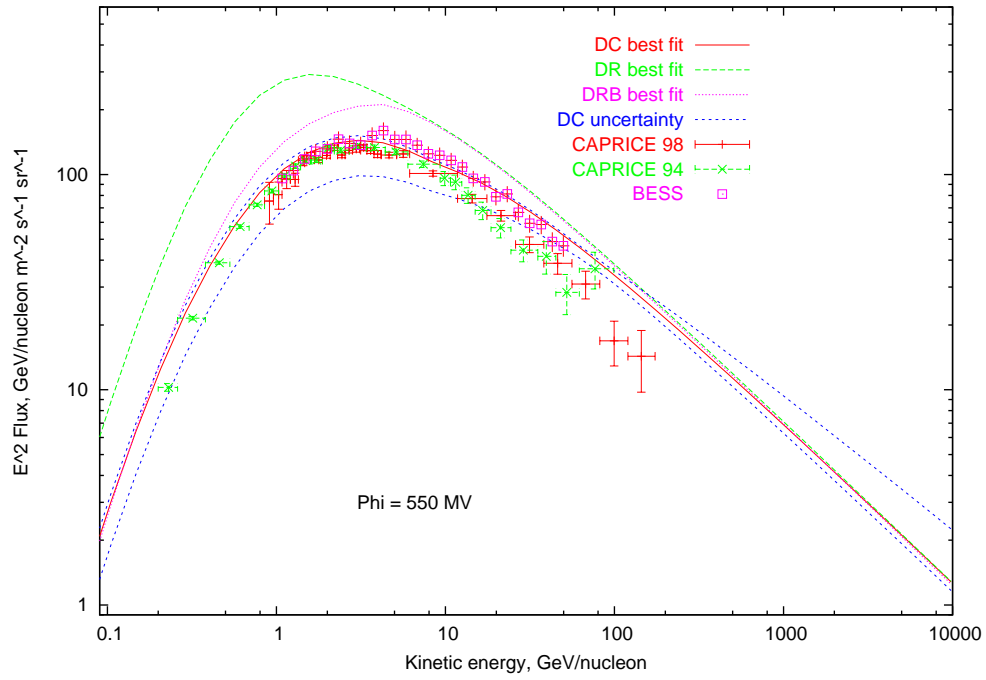


Figure 3.8: Upper and lower bounds of helium spectra due to the uncertainties of the propagation parameters for DC model are represented with dashed blue lines. Spectra that correspond to the parameters of the best B/C fit are given also for the other models: for DC model with red solid line, for DR model with green dashed line and for DRB model with violet dotted line. Experimental data are taken from [150].

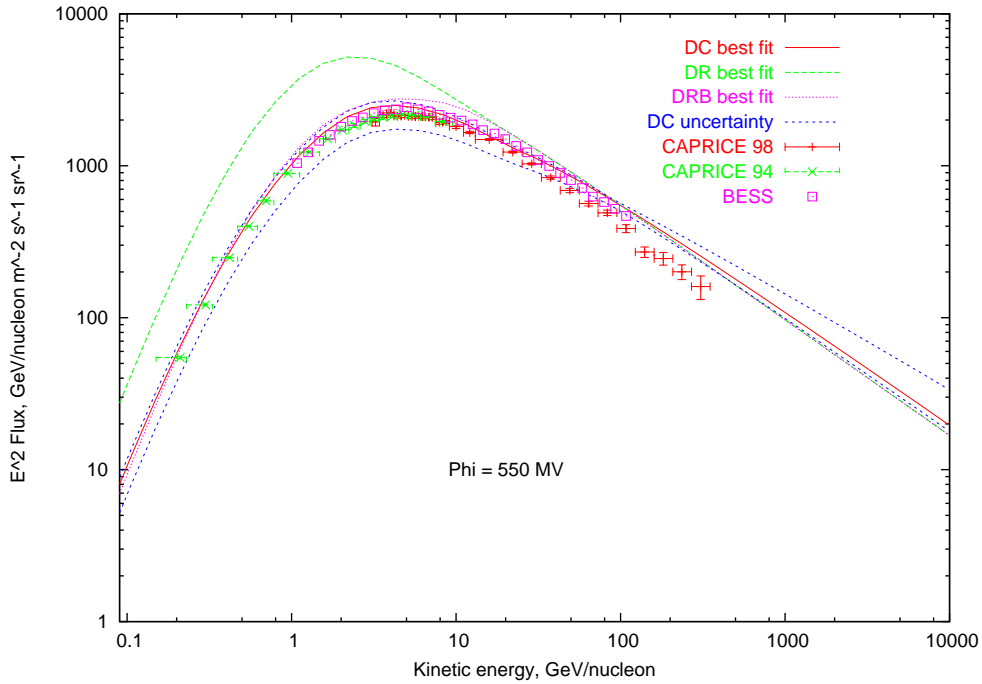


Figure 3.9: Upper and lower bounds of proton spectra due to the uncertainties of the propagation parameters for DC model are represented with dashed blue lines. Spectra that correspond to the parameters of the best B/C fit are given also for the other models. Experimental data are taken from [150].

We have also seen how the obtained antiproton spectra change on variation of the most important antiproton production cross sections. The most important are nuclear reactions that include hydrogen and helium. Antiprotons are created in the interactions of primary cosmic rays (protons and other nuclei) of sufficiently high energies with interstellar gas (see previous sections for some more details). Dominant processes are interactions of high energy primary protons with hydrogen, $p + p \rightarrow p + p + p + \bar{p}$. Parameterization of this cross section used in our version of Galprop code is given in [114]. Other cross sections, those of primary protons with other nuclei, are studied in reference [117]. From these, the most important are those that involve helium, as we already said, and they contribute less than 20% of the total production of all the antiprotons. All the heavier nuclei together give just a few percents of the total production.

Uncertainties of cross sections are influencing on the antiproton spectra uncertainties: simultaneous settings of all the production cross sections to

the maximum/minimum rise/lower the upper/lower propagation parameters uncertainty bounds (already found before). Errors obtained in this way give contributions to the total uncertainties: they are varying from 20% up to 25% in the case of DR model and, very similarly, from 20% up to 24% for DC model (depending of the energy range of the spectra). Non production cross sections, the so called tertiary component, correspond to inelastically scattered secondaries $\bar{p} + X \rightarrow \bar{p} + \tilde{X}$. Those processes tend to bring down the energies of the antiprotons of relatively high energies, flattening like that the spectra. But, even if their uncertainty is relatively big, this does not give relevant change of the antiproton spectra because tertiary contribution is very small. In fact, it has been included just recently in the studies (see [103] and leaky box model section).

The uncertainty in the measurements of helium to hydrogen ratio is bringing another component to the total uncertainty of the cosmic rays spectra. By changing of He/H ratio, in a reasonable range from 0.08 to 0.11 (see [158] and [159], for example) we obtained a relatively small contribution: it vary from 3% - 7% depending of the energy, for both – positron and antiproton flux uncertainty, and – for all of the models we considered, also.

Total uncertainties of positrons and antiprotons are presented in figure 3.10 and in figure 3.11 respectively. They vary from 35% up to 55% for antiprotons and from 20% up to 40% for positrons roughly, for both of the models in the current experimental data energy range.

Let us now look for the moment at plot 3.7. There are presented the two different uncertainties of the positron spectra due to the Solar modulation for the same DRB model (that is fitting the data better than DR model). The first uncertainty (violet dotted curves) is obtained Solar-modulating the lower propagation uncertainty band with 10% bigger ϕ than normal, while the upper one with 10% lower modulation parameter. This is taught to be very conservative error for the Solar modulation parameter. The spectra are still completely above the data. As we used the force field approximation for the Solar modulation, we tried also to change drastically the modulation parameter, with $\pm 50\%$. The resulting curves are represented with blue dashed lines on the plot, and are still completely above the data. As we deal with a medium Solar modulation ($\phi \approx 600MV$) for positron data (we are not near the Solar minimum) the sign-charge drift effect due to the Solar magnetic field polarity should be not very strong.

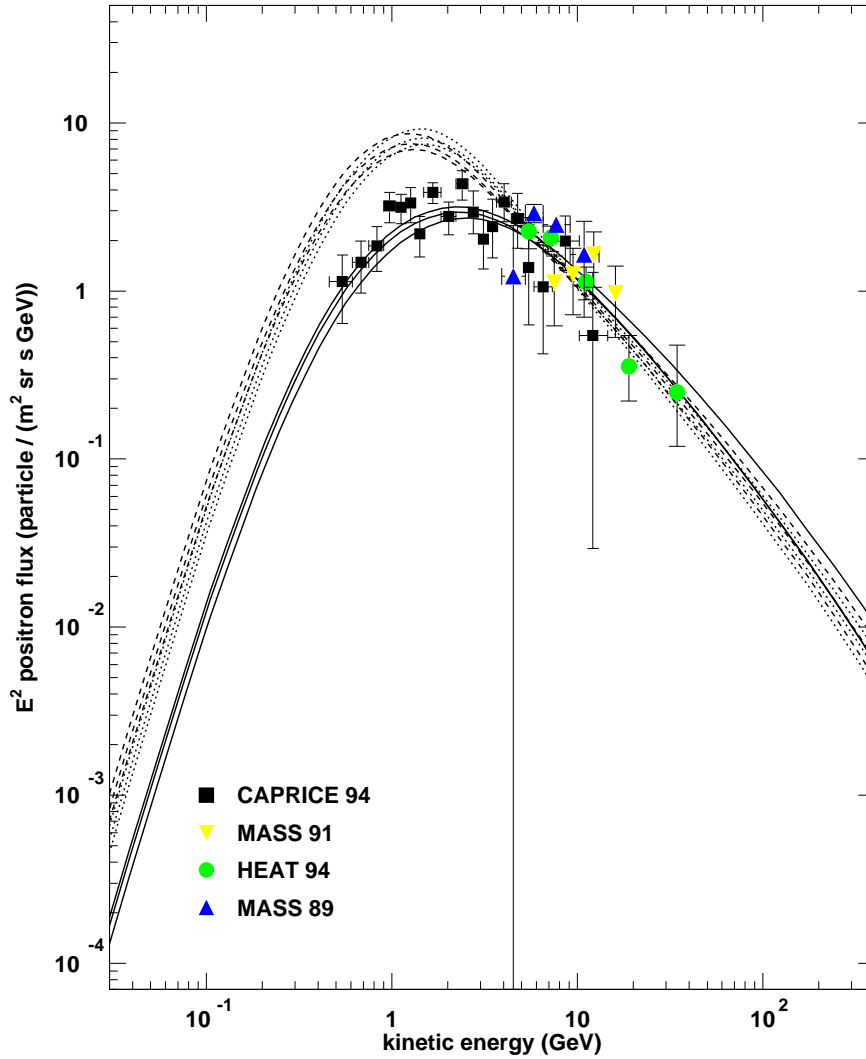


Figure 3.10: Total uncertainties of positron fluxes and spectra that correspond to the parameters of the best B/C fit for DC (solid lines around the best fit curve, also dashed), DR (dashed lines around the best fit curve, also dashed) and DRB model (dotted lines around the best fit curve, also dotted). Experimental data are taken from [149]

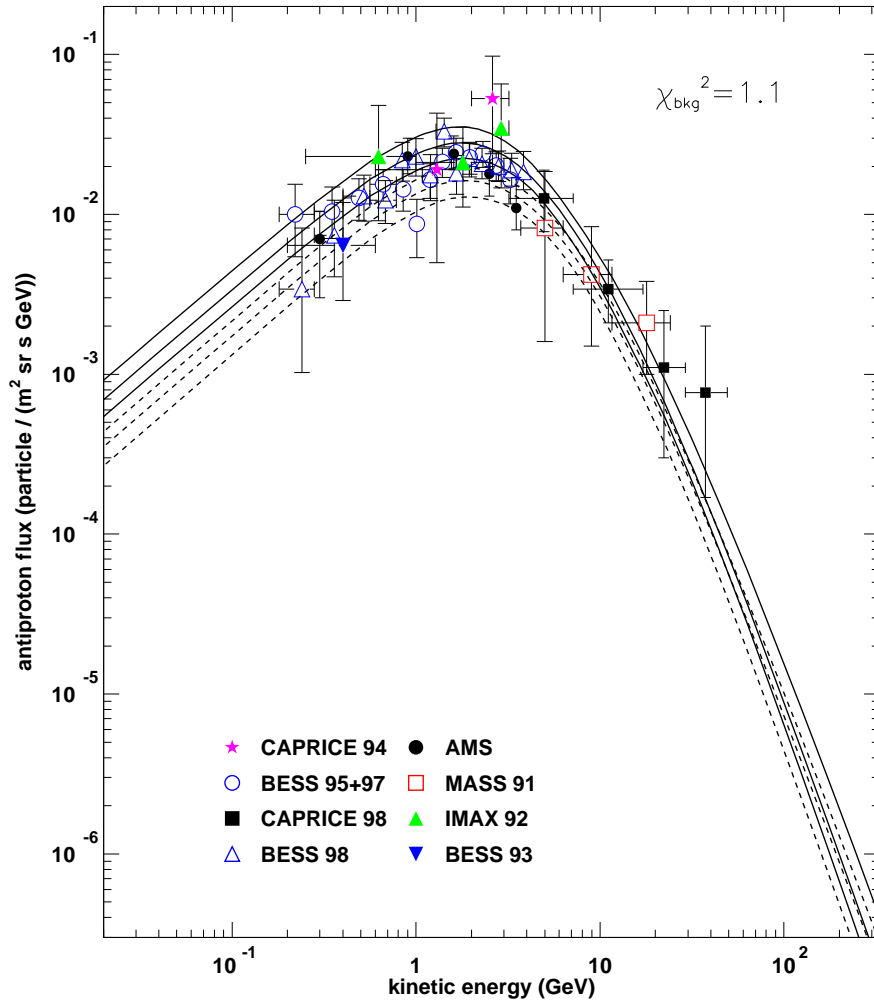


Figure 3.11: Total uncertainties of antiproton fluxes and spectra that correspond to the parameters of the best B/C fit for DC (solid lines around the best fit curve, also solid) and DRB model (dotted lines around the best fit curve, also dotted). Experimental data are taken from [148]

Chapter 4

Component of the Antiproton Spectra Induced by the Neutralino Annihilations

4.1 Parameters at The Weak Energy Scale

In this section we take into account the possibility of a neutralino induced component in the \bar{p} flux. Our analysis is performed in the well known mSUGRA framework [130] with the usual gaugino mass universality at the grand unification scale M_{GUT} .

In the general framework of the minimal supersymmetric extension of the Standard Model (MSSM), the lightest neutralino is the lightest mass eigenstate obtained from the superposition of four interaction eigenstates, the supersymmetric partners of the neutral gauge bosons (the bino and the wino) and Higgs bosons (two Higgsinos). Its mass, composition and couplings with Standard Model particles and other superpartners are a function of the several free parameters one needs to introduce to define such supersymmetric extension. In the mSUGRA model, universality at the grand unification scale is imposed. With this assumption the number of free parameters is limited to five

$$m_{1/2}, m_0, \text{sign}(\mu), A_0 \text{ and } \tan\beta,$$

where m_0 is the common scalar mass, $m_{1/2}$ is the common gaugino mass and A_0 is the proportionality factor between the supersymmetry breaking trilinear couplings and the Yukawa couplings. $\tan\beta$ denotes the ratio of the vacuum expectation values of the two neutral components of the SU(2) Higgs doublet, while the Higgs mixing μ is determined (up to a sign) by imposing the Electro-Weak Symmetry Breaking (EWSB) conditions at the weak

scale. In this context the MSSM can be regarded as an effective low energy theory. The parameters at the weak energy scale are determined by the evolution of those at the unification scale, according to the renormalization group equations (RGEs) [131].

For this purpose, we have made use of the ISASUGRA RGE package in the ISAJET 7.64 software [132]. After fixing the five mSUGRA parameters at the unification scale, we extract from the ISASUGRA output the weak-scale supersymmetric mass spectrum and the relative mixings. Cases in which the lightest neutralino is not the lightest supersymmetric particle or there is no radiative EWSB are disregarded.

The ISASUGRA output is then used as an input in the DarkSUSY package [119]. The latter is exploited to:

- reject models which violate limits recommended by the Particle Data Group 2002 (PDG) [160];
- compute the neutralino relic abundance, with full numerical solution of the density evolution equation including resonances, threshold effects and all possible coannihilation processes [120];
- compute the neutralino annihilation rate at zero temperature in all kinematically allowed tree-level final states (including fermions, gauge bosons and Higgs bosons);
- DarkSUSY estimate the induced antiproton yield

This setup as well as some other similar considerations were already considered in the context of dark matter detection and eventual improvements of the cosmic rays data fits (a list of references includes, for example, [141, 142, 143, 144, 145, 146, 122, 140, 139]), and therefore the comparison of our results with previous works and other complementary techniques should be transparent.

4.2 Clumpy Halo Models

In order to obtain more antiprotons also for higher neutralino masses we have assumed a small clump scenario [133] for the dark matter halo in our Galaxy. In fact, in equation 4.2 the dependence of the antiproton flux is $\propto \rho^2/m_\chi^2$: without increasing the total halo mass by increasing the average density, there can be assumed a local density enhancement, that will also lead to the increasing of the antiproton flux.

By hypothesis the clump is a spherical symmetric compact object with mass M_{cl} and some density profile

$$\rho_{cl}(\vec{r}_{cl}).$$

We denote with f the dark matter fraction concentrated in clumps and we introduce the dimensionless parameter d

$$d = \frac{1}{\rho_0} \frac{\int d^3 r_{cl} [\rho_{cl}(\vec{r}_{cl})]^2}{\int d^3 r_{cl} \rho_{cl}(\vec{r}_{cl})} \quad (4.1)$$

that gives the overdensity due to a clump with respect to the local halo density $\rho_0 = \rho(r_0)$, where r_0 is our distance from the Galactic center. In a smooth halo scenario the total neutralino induced \bar{p} flux calculated for $r = r_0$ is given by [134]

$$\Phi_{\bar{p}}(r_0, T) \equiv (\sigma_{\text{ann}} v) \sum_f \frac{dN^f}{dT} B^f \left(\frac{\rho_0}{m_{\tilde{\chi}}} \right)^2 C_{\text{prop}}(T). \quad (4.2)$$

where T is the \bar{p} kinetic energy, $\sigma_{\text{ann}} v$ is the total annihilation cross section times the relative velocity, $m_{\tilde{\chi}}$ is the neutralino mass, B^f and dN^f/dT , respectively, the branching ratio and the number of \bar{p} produced in each annihilation channel f per unit energy and $C_{\text{prop}}(T)$ is a function entirely determined by the propagation model.

In the presence of many small clumps the \bar{p} flux is given by

$$\Phi_{\bar{p}}^{\text{clumpy}}(r_0, T) = fd \cdot \Phi_{\bar{p}}(r_0, T) \quad (4.3)$$

For the smooth profile we have assumed a Navarro, Frenck and White profile (NFW) [135].

4.3 Propagation of the Neutralino Induced Component

The primary contribution to the antiproton flux has been computed using the public code DarkSUSY[136]. We have modified the antiproton propagation in order to be maximally consistent with the DC propagation model as implemented in Galprop code. We assumed diffusion coefficient spectra used in Galprop code with our best fit values for the diffusion constants D_0 and δ . In DarkSUSY, the convection velocity field is constant in the upper and the lower Galactic hemispheres (with opposite signs, and so it suffers unnatural

discontinuity in the Galactic plane), while Galprop uses magnetohydrodynamically induced model, in which one component of velocity field along the Galactic latitude (the only one that is different from zero) increases linearly with the Galactic latitude [101]. We have assumed an averaged convection velocity calculated from the Galactic plane up to the Galactic halo height z .

4.4 Some Examples of the Primary Component of the Antiproton Flux

In this section we present four different contributions to the antiproton flux induced by the annihilations of neutralinos. Fluxes are calculated for different neutralino masses (obtained from a particular choice of the five mSUGRA parameters) and for different clumpiness factors fd . Those fluxes are given here just as few examples, and as some our tests, or mean-results; we wanted to check is everything works correctly. All the minimal supergravity theory parameter space was not systematically scanned. This, detailed analysis is done in the last section of the fifth chapter.

Let us now briefly comment the behaviour of the obtained signal contribution to the antiproton flux. Higher neutralino masses produce primary contributions that improve high energy data fits, that is taught to be necessary for every background contribution. The price to be paid is that of the necessity of the increasing of the clumpiness factors to do so. This is because of the dependence from the inverse neutralino mass squared m_χ^{-2} in the primary antiproton flux formula 4.2.

On the other side, from the same reasons, small neutralino masses produce relatively high fluxes, but at small energies, where the data are already fitted well with a background contribution only. This problem finally leaves just a small part of the mSUGRA parameter space that will give the primary contributions that are satisfying experimental data fit, as we will see in the last section of the fifth chapter. We remark that for these models we have not computed the neutralino relic density.

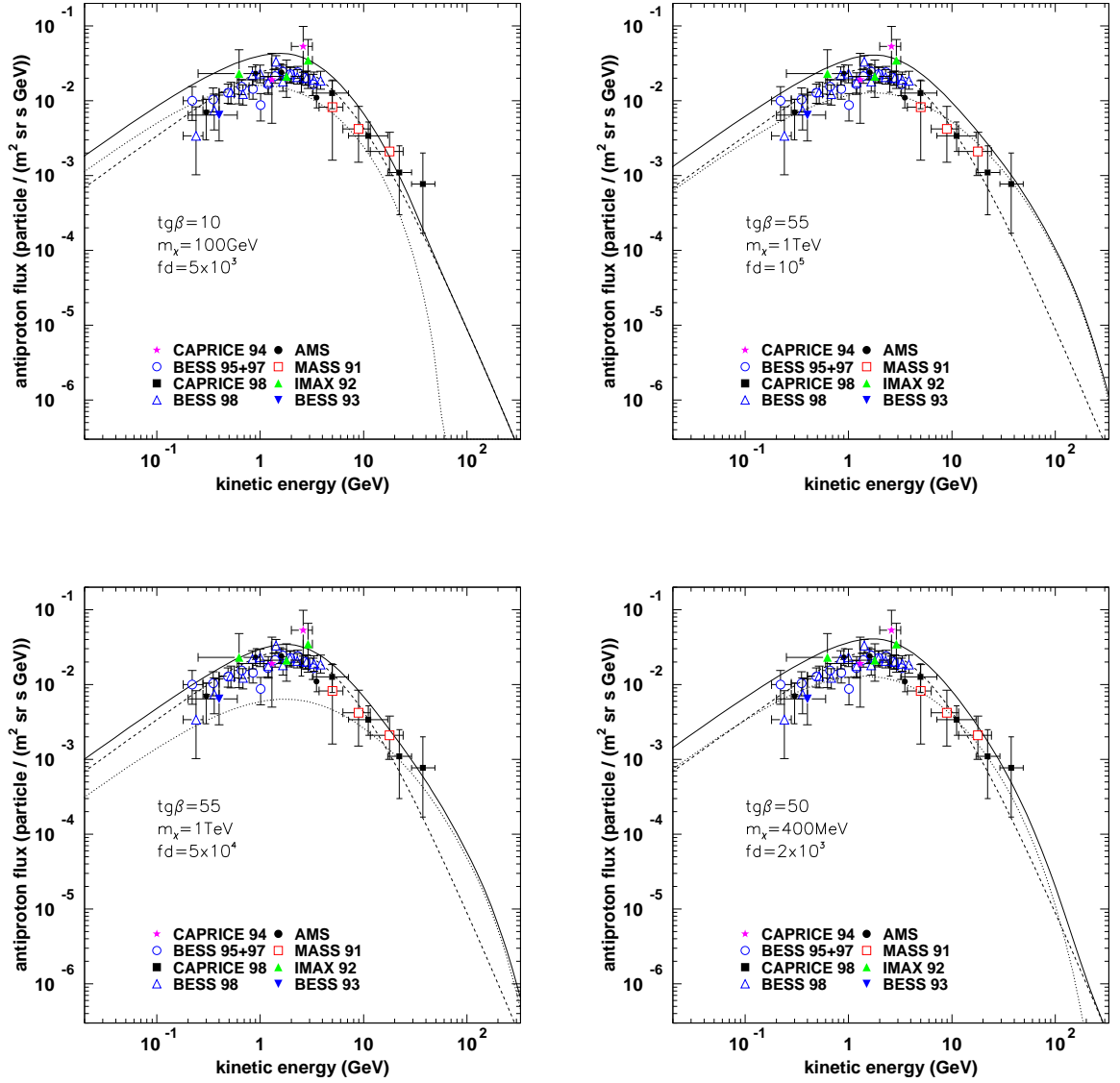


Figure 4.1: Different neutralino annihilations induced contributions to the total antiproton flux with the DC model background that corresponds to the propagation parameters of the best fit of the B/C data. The dashed lines correspond to the background contributions, the punctuated lines correspond to the neutralino induced contributions, while the solid lines correspond to total antiproton flux. For just the background flux the reduced χ^2 is 1.1, what means that just the background fits the experimental data excellent. Detailed χ^2 statistical study of all the considered total fluxes is done in the last section of the fifth chapter.

Chapter 5

Detection of Cosmic Ray Spectra

5.1 Introduction

The idea of exploiting cosmic antiprotons measurements to probe unconventional particle physics and astrophysics scenarios has a long history [1-10] and moved the cosmologists for several decades. Shortly after the discovery of the CP violation in the weak interactions in '64, Sakharov formulated his famous hypotheses that were assumed to be a reasonable starting point to explain the apparent contradiction between the fundamental laws of the nature and the observations. Several balloon borne experiments were dedicated to the search for antiparticles and antinuclei, and in the 70's the teams of R. Golden in USA [20] and of E. Bogomolov in Russia [21] identified the first antiprotons in cosmic rays (the positrons were discovered more than 40 years before by Anderson). Then, the antiproton spectrum was intensively studied for searching for signals exceeding the background of the antiprotons produced in the interactions of CR's with the interstellar matter.

In figure 5.2 (on the left) is shown the data on the antiproton/proton ratio before 1990. At that time the standard production models (black lines) [61] could not account for all the antiprotons measured by the Golden et al. and Buffington et al. [22] experiments, and this triggered the formulation of many exotic models ranging from antiprotons coming from antigalaxies [23] to annihilation of supersymmetric dark matter (gray curve) [19].

The reason why we should expect a rise with increasing energies of the antiproton/proton ratio in the case of the existence of antigalaxies is because we know that, due to the magnetic field in the galaxies, the extragalactic component of the cosmic rays that can reach the Earth increases at higher

Table 5.1: Second generation balloon flights (on the left the flights of the WiZard collaboration)

WiZard collaboration	
MASS -1,2 (89,91)	BESS (93, 95, 97, 98, 2000)
TrampSI (93)	Heat (94, 95, 2000)
CAPRICE (94, 97, 98)	IMAX (96)
μ Flight (2003)	BESS Long duration flight (2004)

energies and so also the antiproton component should increase.

Furthermore a bump in the antiproton flux in case of the existence of a dark halo in the galaxy made up of Weakly Interacting Massive Particles (WIMPs) is expected because, as in standard particle theories, the annihilation cross section is higher near the threshold of the process and, since the velocity of the WIMPs is trascurable in respect to the mass, a contribution to the antiproton spectrum is expected only up to the WIMP mass (we will discuss more precisely this point in paragraph 3).

In the same years the results of the positron ratio measurements were somewhat similar, with the experiments giving an higher flux of positron at energies greater than 10 GeV (see figure 5.2 on the right), explained only with some exotic production, like again the annihilation of WIMPs giving a contribution as shown by the gray curve in the figure 5.2 (from [29]).

Positrons and electrons are unique among cosmic rays because they are the lightest charged leptons. Due to their low mass, high-energy electrons and positrons undergo interactions with the ISM, which result in severe energy losses at high energies. While the most of the observed electrons are believed to be of primary origin, for positrons this is yet to be established. Positrons are even harder to observe than antiprotons due to the high flux of protons (more than 1000 times higher). All observations to date have suffered from the risk of subtracting significant background.

5.2 The Second Generation Experiments

In the last decade there has been an increase of experiments performed using novel techniques developed for accelerator physics. This has permitted

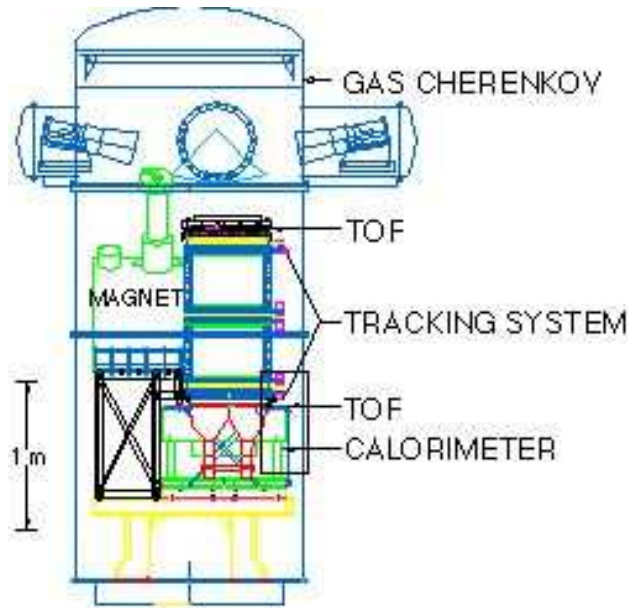


Figure 5.1: the MASS 89 balloon apparatus

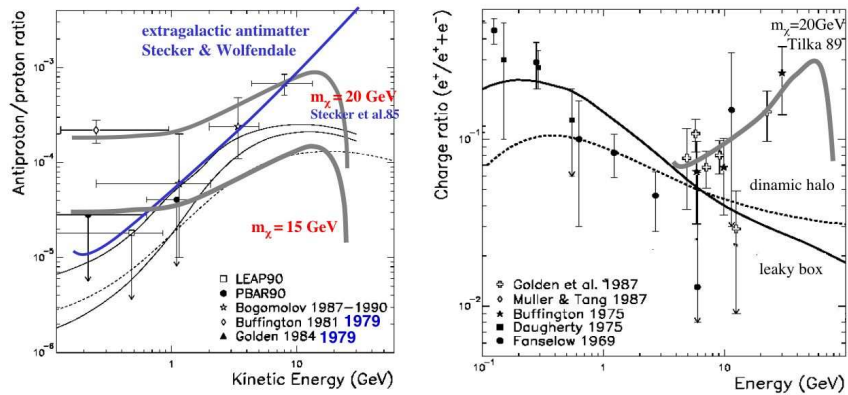


Figure 5.2: Antiproton/proton ratio experimental situation before 1990 (on the left). For the experimental data the references are: LEAP [24], PBAR [25], E. Bogomolov et al. [21], Buffington et al. [22], Golden et al. [20]. Positron fraction experimental situation before 1990 (on the right) compared with the foreseen secondary production in the interstellar medium and an exotic model. For the experimental data the references are: Golden et al. [30], Müller & Tang [31], Buffington et al. [32], Daugherty et al. [33], Fanselow et al. [34]

to improve the statistical and systematic significance of the experimental measurements.

The antiproton flux is less than 10^{-5} of the proton's one at 200 MeV, reaches 2×10^{-4} at 10 GeV, afterwards decreases to about 10^{-5} at 1 TeV and continues to decrease at higher energies. Because of these small ratios of the antiproton to proton fluxes, the identification of the antiprotons requires the use of a magnetic spectrometer for selecting the negatively charged particles, leaving antiprotons to be separated from electrons. Only in the Buffington experiment at low energies the identification of the antiprotons was obtained by the pattern of their annihilation in an imaging calorimeter without the help of a magnetic field. This experiment has been contradicted by all the following measurements, probably for the weakness in the identification of the antiprotons. As we said, these kind of measurements are quite challenging, antiprotons and positrons must be distinguished from a large background of protons and electrons. Moreover, products of interactions of cosmic rays in the atmosphere above the payload, such as muons and pions, are a significant background for measurements performed with balloon borne experiments. Furthermore, the data must be corrected for the secondary production in the overlying atmosphere, which becomes increasingly important for energies below about a few GeV. Hence, along with detectors which must provide a precise determination of the rigidity (momentum \times speed of light/charge) of the particles, other detectors are required to clearly identify the particles. The main goal of the experiments is to provide measurements of the fluxes of the cosmic-rays; hence precise determination of the efficiencies of the various detectors is needed. In the last decade, there has been an increase of experiments performed using novel techniques developed for accelerator physics. This has permitted to increase the statistical and systematic significance of the experimental measurements. A list of them is given in table 5.1

Beginning from 1995, the WiZard Collaboration and the AMS collaboration began to launch also space detectors. The list is given in table 5.2 together with other connected space experiments.

5.2.1 The MASS Apparatus

The MASS apparatus is shown in figure 5.1. The payload has twice flown on a balloon. The first flight took place from Prince Albert, Sask. on Sept 5, 1989, a second flight from Fort Sumner, New Mexico, on Sept 1991.

The main parts of the apparatus, are:

a) a spectrometer, composed by a superconducting magnet and a tracking system, consisting of 8 multi-wire proportional counter (MWPC) and two drift chamber each containing 10 layers of hexagonal drift cells (the drift

Table 5.2: Space experiments: Technology and Physics

*	Cosmic rays		
✓	SilEye-1	MIR	1995-1997
✓	SilEye-2	MIR	1997-2001
✓	AMS-01	Shuttle	1998
✓	NINA-1	Resurs	1998
✓	NINA-2	MITA	2000
✓	Alteino (SilEye-3)	ISS	2002 (April 25)
▷	PAMELA	ResursDK1	2005
▷	AMS-02	ISS	2008
*	Low energy gamma-ray		
✓	HETE-2	Pegasus	2002 (Jan 14)
✓	INTEGRAL	Proton	2002 (Oct 17)
▷	SWIFT	Delta II	2004
▷	AGILE	MITA	2005
▷	GLAST	Delta II	2007

chamber modules were added after the 1989 flight). Both system have spatial resolution better than $200 \mu m$. Details of the MPWC system can be found in [35]

b) a Freon 12 Cherenkov detector with a path length of $1 m$ viewed by four phototubes. The efficiency for muon detection above the threshold γ_{tr} is 98%, while the accidental rate is less then $5 \cdot 10^{-4}$ for low energy muons.

c) a scintillators system was used for the trigger, for Time Of Flight (TOF) measurements to determine the direction of travel and for charge analysis

The TOF time resolution is about $200 ps$, the time difference between downward and upward particles is at least 30 std.dev.

d) a calorimeter consisting of 40 layers (20 in each of two orthogonal view) of 64 brass streamer tubes for a total of 7.3 radiation lengths [36]. The special feature of the calorimeter is that it provides not only an energy resolution, but also an accurate reconstruction of the annihilation vertex and

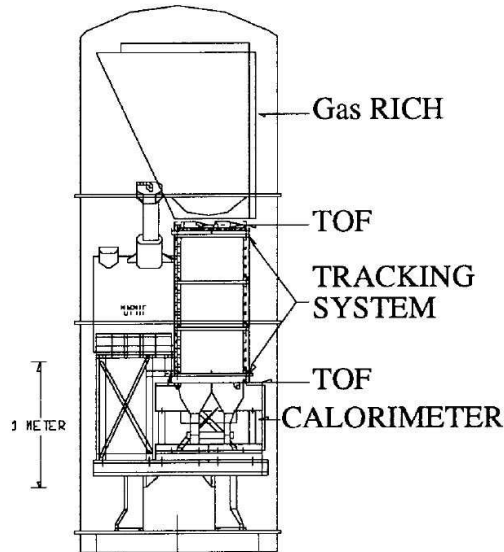


Figure 5.3: Schematic of the CAPRICE98 baseline instrument.

of the out coming tracks. This is particularly useful to discriminate between electromagnetic and hadronic showers since full containment of the particle is forbidden by the weight limitation of the payload.

5.2.2 The Tramp-SI Apparatus (TS93)

The MASS configuration limited to about 20 GeV the highest energy detected for positron observation because as the proton Cherenkov threshold. In order to increase this threshold, a Transition Radiation Detector (TRD) has been used in the 1993 flight (TS93 or Tramp-SI) for the observation of high energy positrons. The TRD uses carbon fibers to provide transition in refractive index. An extremely relativistic ($\gamma > 1000$) particle traversing these transition regions will emit x-rays of an energy that can be detected by an MWPC. Electrons and positrons with energies above 500 MeV satisfy this criterion, but protons must have an energy above 1 TeV to produce transition radiation. The TRD consist of 11 layers of carbon fibers each separated by a MWPC. This allow to falsely identify $4 \cdot 10^{-4}$ of the protons as positrons with an efficiency of 90% for the detection of positrons [37]. Positrons are especially difficult to identify because the e^+/p ratio is on the order of 10^{-3} at low energy, decreasing to 10^{-4} at high energies. Thus to measure positrons reliably, one would like to have a system which has a probability of misidentifying a proton as a positron which is 10^{-5} or better. To accomplish this

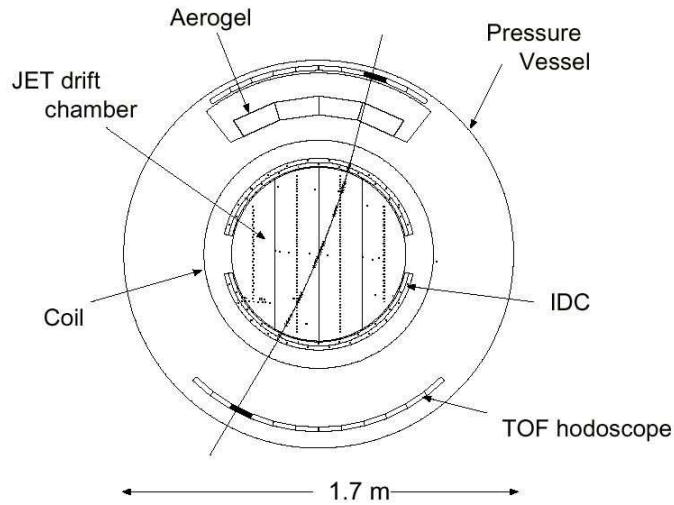


Figure 5.4: Schematic of the BESS baseline instrument.

a silicon imaging calorimeter is used in connection with the TRD. The silicon calorimeter offers significant improvement over the MASS streamer tube calorimeter in two areas: 1) it gives the measurement of energy release in each strip rather than "on / off" indication and this allows for a precise determination of the longitudinal and lateral profile of the shower and of the total energy released in the calorimeter 2) it decreases vertical height, thus allowing a greater geometrical factor. In the Tramp-SI configuration the calorimeter is formed by 5 layers of silicon detectors alternated with 1 radiation length of tungsten. A single layer is composed by a $8 \cdot 8$ matrix of sensitive modules and each module is formed by two silicon detectors, each having a total area of $6 \times 6 \text{ cm}^2$ and a thickness of $380 \mu\text{m}$; they are mounted back to back with perpendicular strips to give x and y coordinates. Each module has 16 strips 3.6 mm wide connected to the neighboring one to form single strips 50 cm long. Details of the silicon calorimeter design may be found in [38].

5.2.3 The CAPRICE Apparatus

The very low energy part of the positron and antiproton spectrum (below 5 GeV) was covered by the Cosmic AntiParticle Ring Imaging Cherenkov Experiment (CAPRICE) flights in 1994. The CAPRICE apparatus is composed by a solid Ring Imaging Cherenkov Detector (RICH) with the TOF system, the tracking system and a silicon calorimeter. The radiator of the RICH is 1 cm of NaF (refractive index=1.4 and a threshold Lorenz factor of

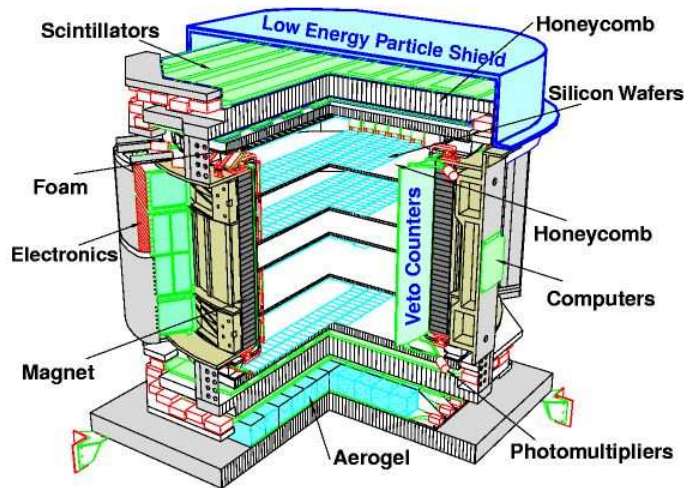


Figure 5.5: AMS on the Discovery STS 91 precursor flight, June 1998.

1.5). This is followed by a helium-filled space which allow the expansion of the Cherenkov disk and the formation of a ring of Cherenkov photons. The Cherenkov ring is then transmitted through a quartz window into an MWPC filled with methane, isobutane and TMAE (tetra-dimethyl-amine-ethylene). The MWPC utilizes a segmented cathode readout (8 mm squares) to record $x - y$ location of the particle passage and the conversion location for the Cherenkov photons. The magnet spectrometer had a superconducting magnet and a tracking device providing an average maximum detectable rigidity of 330 GV. The silicon-tungsten calorimeter was the same used for Tramp-SI with the addition of three planes for a total of 8 planes (7 radiation lengths, about 0.3 hadronic interaction lengths).

In the energy range 1-4 GeV the Cherenkov ring diameters of e^- and μ^- are separated more than 10 std.dev. from that of the antiprotons, consequently the separation of the background from antiprotons is assured using only the Rich. Above 4 GeV the ring diameters begin to converge, but at these energies the calorimeter has excellent rejection power against the electrons. The e^+ and e^- are separated from the μ with the request of electromagnetic cascade in the calorimeter. Details of CAPRICE94 apparatus may be found in [39].

In 1998 is launched from Fort Sumner CAPRICE98, shown in figure 5.3, with a new gas RICH detector with a threshold Lorenz factor of 19 and an angular resolution less than 2 mrad. The RICH consisted of a 1m tall box filled with the gas radiator: high-purity C_4F_{10} . Cherenkov photons are

reflected by a spherical mirror, placed on the bottom of the box, up to a MWPC, flushed with ethane gas saturated with TMAE vapours, where they are detected [40]. This new apparatus allowed us to mass resolve and, thus, to unambiguously identify cosmic-ray antiprotons, extending for the first time the measurement up to 50 GeV [46].

5.2.4 The BESS Experiment

In the mean time the BESS collaboration begin the construction of a different kind of apparatus, tuned for the very low energy part of the spectrum but with a very large geometric factor.

Figure 5.4 shows the schematic of the BESS apparatus [41] as it was employed in two balloon flights in 1997 and 1998. It included a superconducting magnet that produced an uniform field of 1 Tesla in which a tracking system of drift chambers was embedded. Two sets of scintillators were placed above and below the tracking system and a Cherenkov counter with a silica-aerogel radiator was installed below the upper scintillators. The tracking system was used to measured the deflection (1/rigidity) of the particles, while the scintillators provided measurements of dE/dx and time-of-flight. The Cherenkov was used to veto the electron and muon backgrounds. Antiprotons were selected requiring a single track fully contained in the tracking volume. Then, the ionization measurements in the scintillators and drift chamber were required to match the dependence on rigidity of the ionization losses for protons. The final selection was performed using the particle velocity (β) measured by the time-of-flight system (at high velocity also the Cherenkov was used in anticounter mode). BESS has been flown annually from 1993 with a constant upgrade of the detectors.

5.2.5 The AMS Experiment

The Alpha Magnetic Spectrometer (AMS) [42] was flown on the Space Shuttle Discovery during flight STS-91 (June 1998) in a 51.7 degree orbit at altitudes between 320 and 390 km. The apparatus, shown in figure 5.5, includes a permanent Magnet, Anticounter (ACC) and Time of Flight (ToF) scintillator systems, a large area Silicon Tracker and an Areogel Threshold Cherenkov counter. The magnet is a permanent Nd-Fe-B one with $BL^2 = 0.15Tm^2$ and a weigh of ~ 2 tons. A charged particle traversing the spectrometer triggers the experiment through the ToF system, which measures the particle velocity with a resolution of ~ 120 ps over a distance of ~ 1.4 m.

During the period june 2nd to june 12th, 1998 the Shuttle Discovery has performed 154 orbits at an inclination 51.7° and at an altitude varying be-

tween 390 to 350 *km*. During the mission AMS collected a total of about 100 Million triggers, at various Shuttle altitudes. A review of the results can be found in [43]. The results for the antiproton and positron spectra will be shown with the summary of the experimental situation up to now in the next paragraph.

5.3 The Present Experimental Situation and the Future Experiments

We have described most of the experiments, the others are the HEAT-pbar experiment [50], similar to TS93 in combining a transition radiation detector with an electromagnetic calorimeter for the measurement of antiprotons up to 50 GV and HEAT [45] that identified positrons up to 50 GeV, and IMAX92 [49]. The MASS91 data are from [47], the AMS98 antiproton data are from [43].

Positrons appear to be mainly from CR interactions in ISM but slight feature exists above ~ 7 GeV. This can be seen better looking at the experiments one by one; the new HEAT data are in [58], while the CAPRICE98 [51] and MASS91 data [57] are shown in figure 5.6.

None of the existing primary astrophysical e^+ models were explaining the structure well [59], except now Galprop in the framework of DC model. Feature (amplitude, shape and location) could be reproduced with a number of realistic SUSY models that are allowed by current accelerator limits (supposing various backgrounds that are not fitting the data well).

5.4 Future Experiments: BESS Polar Flights

Three major experiments are being prepared for the future: a new polar BESS instrument, the satellite PAMELA experiment, and AMS on the International Space Station.

The Polar BESS long duration experiment features a reduced instrument (see figure 5.7) on the top of a payload with big omnidirectional solar panels (see figure 5.8) in order to have enough power during the scheduled \sim two weeks flight. Polar BESS will have a good sensitivity to the lower energy part of the CR spectrum and will perform a precise measurement of low energy antiprotons. The first flight is scheduled for 2004.

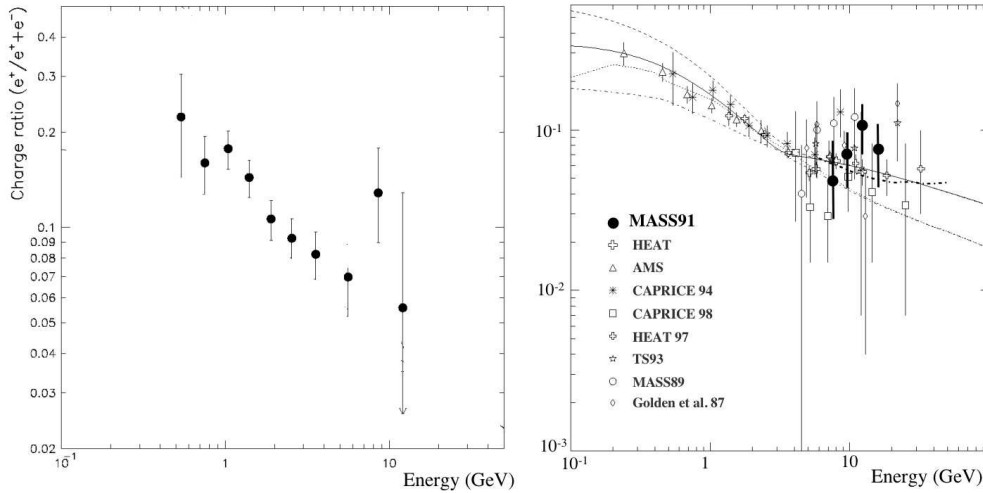


Figure 5.6: Positrons fraction as seen by CAPRICE98 [51] and MASS91 [57].

5.5 Future Experiments: PAMELA

The PAMELA instrument, shown in figure 5.9, is a satellite-borne apparatus built by the WiZard-PAMELA collaboration [63]. It will be installed on-board of the RESURS-DK1 satellite to be launched in 2003 for a mission at least three years long.

The list of the people and the Institution involved in the collaboration together with the on-line status of the project is available at <http://wizard.roma2.infn.it/>.

5.5.1 PAMELA Scientific Objectives

The PAMELA Scientific Primary goals are the search for heavy nuclei and non baryonic particles outside the Standard Model, for the understanding of the formation and evolution of our Galaxy and the Universe and for the exploring of the cycles of matter and energy in the Universe.

Additional objectives of PAMELA are the study of galactic cosmic rays in the heliosphere, Solar flares, distribution and acceleration of solar cosmic rays (SCR's) in the internal heliosphere, magnetosphere and magnetic field of the Earth, stationary and disturbed fluxes of high energy particles in the Earth's magnetosphere and anomalous component of cosmic rays.

The PAMELA observations will extend the results of balloon-borne experiments over an unexplored range of energies with unprecedented statistics

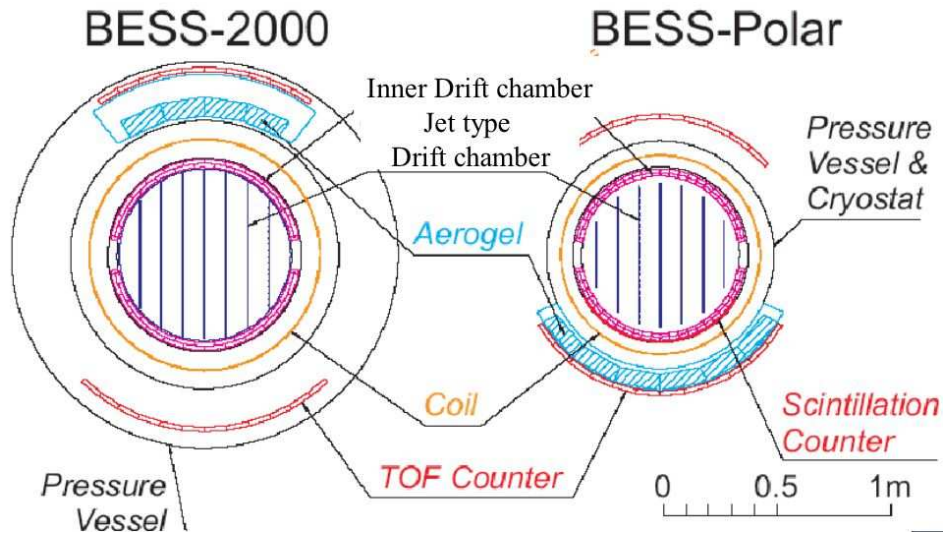


Figure 5.7: Comparison between BESS and Polar BESS instruments.

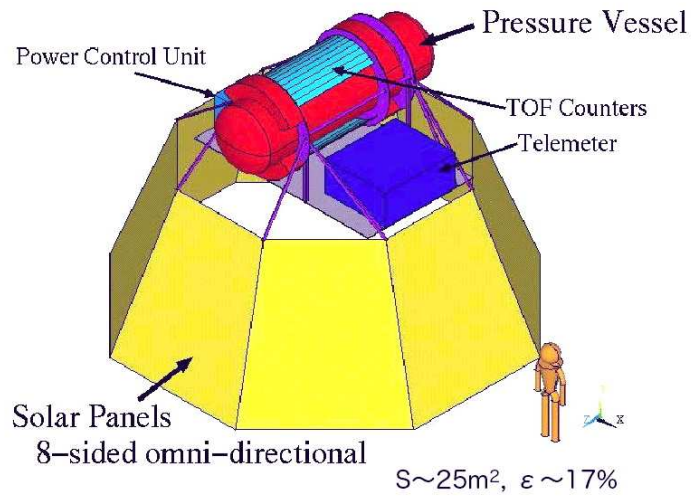


Figure 5.8: Schematic of the Polar BESS payload.

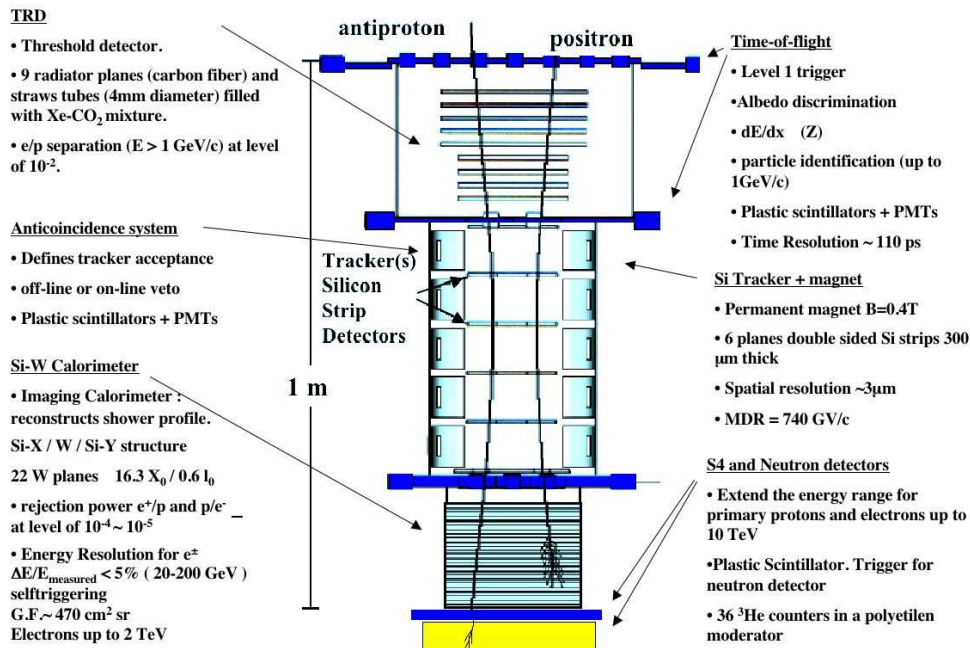


Figure 5.9: Schematic of the PAMELA baseline instrument.

and will complement information gathered from Great Space Observatories.

More precisely, during its three years of planned operation, PAMELA will measure with very high statistics:

- Positron flux from 50 MeV to 270 GeV (present limits 0.7 - 30 GeV)
- Antiproton flux from 80 MeV to 190 GeV (present limits 0.4 - 50 GeV)
- Limit on antinuclei $\sim 10^{-8}(\overline{He}/He)$ (present limit about 10^{-6})
- Electron flux from 50 MeV to 3TeV
- Proton flux from 80 MeV to 700 GeV
- Light nuclei flux (up to oxygen) from 100 MeV/n to 200 GeV/n
- Electron and proton components up to 10 TeV
- Continuous monitoring of the cosmic rays Solar modulation

Examples of the expected data from the experiment PAMELA for the background fluxes and in the neutralino annihilations scenario for three years of operation will be shown in the next section.

5.5.2 The PAMELA Telescope

The PAMELA telescope, based on the experience obtained in the WiZard balloon flights and in the proposed WIZARD [64] on ASTROMAG and Mass-

Sat [65] proposals, is composed by:

1. A magnetic spectrometer to determine the sign of the electric charge with a very high confidence degree and to measure the momentum of the particles. The magnetic system is composed by five permanent magnet of Nd-Fe-B, each 8 cm high, that provide a field inside the tracking volume of about 0.4 T. There are six planes of silicon micro-strip detectors for tracks reconstruction with a spatial resolution of $3 \mu\text{m}$ in the bending view giving a Maximum Detectable Rigidity (MDR) of 740 GV/c.

- A Transition Radiation Detector (TRD) for distinguishing at the level of 10^{-2} between electromagnetic and hadronic showers from 1 GeV to about 1 TeV; the TRD is based on small diameter straw tubes filled with Xe-CO₂ mixtures and arranged in double layer planes interleaved by carbon fiber radiator.

2. A $16X_0$ silicon imaging calorimeter to discriminate at the level of $10^{-4} - 10^{-5}$ between electromagnetic and hadronic showers. It is composed by silicon strip sensors, interleaved with tungsten plates as converter. The energy resolution for positrons is of the order of $15\% / E^{1/2}$. In self triggering mode the calorimeter geometric factor is about $470 \text{ cm}^2 \text{ sr}$, allowing the measuring with useful statistics of the electron flux up to 2 TeV.

- Six scintillation counter hodoscopes (each 7 mm thick) for the event trigger and TOF measurements with a time resolution of $\sim 110 \text{ ps}$ that provides albedo discrimination and particle identification up to 3 GeV/c.

- An additional plastic scintillator S4 and a neutron detector composed by 36 ³He counters in a polyethilen moderator allow, together with the imaging calorimeter, to extend the energy range for primary protons and electrons up to 10 TeV.

- A set of scintillation counters covering the top edge and the sides of the magnetic spectrometer and the bottom part of the calorimeter completes the telescope, for a further labeling of contaminating events.

Others characteristics of the PAMELA instrument are:

1. An acceptance (geometrical factor) of $20.5 \text{ cm}^2 \text{ sr}$;
2. A total volume of $120 \times 40 \times 45 \text{ cm}^3$;
3. A total mass of 470 kg;
4. A power consumption of 360 W.

The PAMELA instrument will be installed onboard the russian RESURS-DK1 satellite, built by TsSKB-Progress. It will be launched from Baikonur with a Soyuz TM rocket and placed on an elliptic orbit at altitude 300-600

Km and an inclination of 70.4° .

Averaging on the Solar activity of the first three years foreseen for the PAMELA flight (2003-2006) we expect to collect in 10^8 s the following approximate numbers for particles, antiparticles and some nuclei:

protons	$3 \cdot 10^8$	anti-protons	$3 \cdot 10^4$
electrons	$3 \cdot 10^6$	positrons	$1 \cdot 10^5$
He nuclei	$4 \cdot 10^7$	Be nuclei	$4 \cdot 10^4$
C nuclei	$4 \cdot 10^5$	anti-nuclei limit	$6 \cdot 10^{-8}$ (90% C.L.)

5.6 The Detection of the Secondary Components of the Positron and the Antiproton Fluxes by PAMELA

In this section we will present graphically the results of the calculated statistical errors for PAMELA experiment (in further text simply expectations) for the positron and the antiproton background spectra calculated with Galprop propagation code. The calculation is done for the three years mission in which PAMELA will measure with high statistics various cosmic rays spectra, as we saw in the previous sections.

This was done, at the first palce, for the background components for various propagation models, for the fluxes that correspond to the propagation parameters of the best B/C data fit, only. But, also in this section, as an example, we will give the results for PAMELA's expectations for the total flux in the case of DC model background. This model we choose for the further study of detectability by PAMELA of the supersymmetry induced signal component in the antiproton flux, that will be reported in details in the next section.

For the calculations we used PAMELA's geometrical factor (or acceptance, $G = 20.5 \text{ cm}^2 \text{ sr}$) explained in the previous section and detector characteristic (see [111, 113, 112], for example). This characteristic is given by the results of the test measurements of the simultaneous (effective) triggering of the first and the last detector in the apparatus. The results of the measurements are graphically represented in figure 5.10.

We extrapolated this data points from the figure 5.10, and used that extrapolation as the percent of the simultaneous triggering for the calculation of the statistical errors.

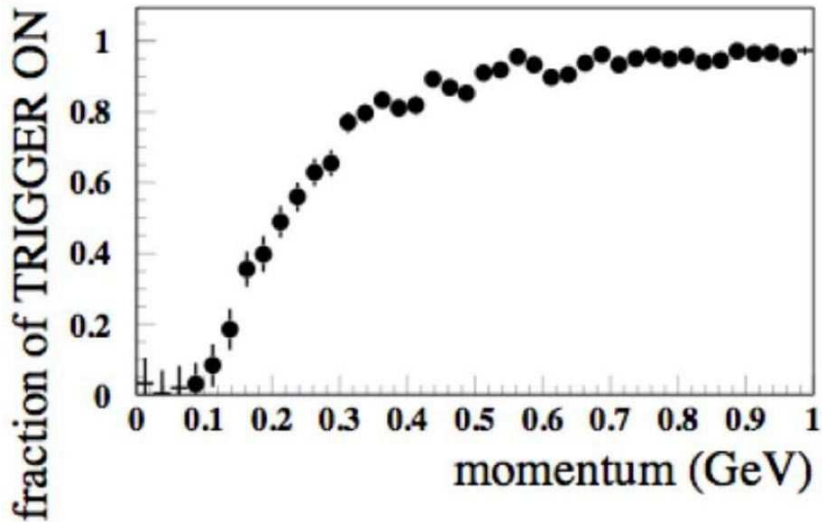


Figure 5.10: The percent of the simultaneous triggering of the first and the third detector of PAMELA.

PAMELA's statistical errors for positrons and antiprotons for DC model background flux components only are given in figure 5.11 and in figure 5.12. For antiprotons we are presenting also the expectations for DRB propagation model in the figure 5.13 for completeness. We don't present PAMELA's expectations for antiprotons for DR model, as DR model flux that correspond to the best B/C fit propagation parameters is almost identical with that of DRB model. For more details about the presented fluxes see the captures of the figures.

As an example, in this section we show (figure 5.14) also the PAMELA's expectations for the total flux

$$\phi_{tot} = \phi_{bkg} + \phi_{susy}.$$

This flux is defined by the background flux, ϕ_{bkg} , given by DC model antiproton flux that correspond to the best fit of the B/C data and the component induced by the neutralino annihilations, ϕ_{susy} , that correspond to the most interesting, third, mSUGRA model (i.e. point in the mSUGRA parameters space) from the figure 4.1. PAMELA's statistical errors for the total flux are confronted with PAMELA's statistical errors in the case of just the DC model background, experimental data from [148] and the total propagation uncertainty of the background component of the total flux.

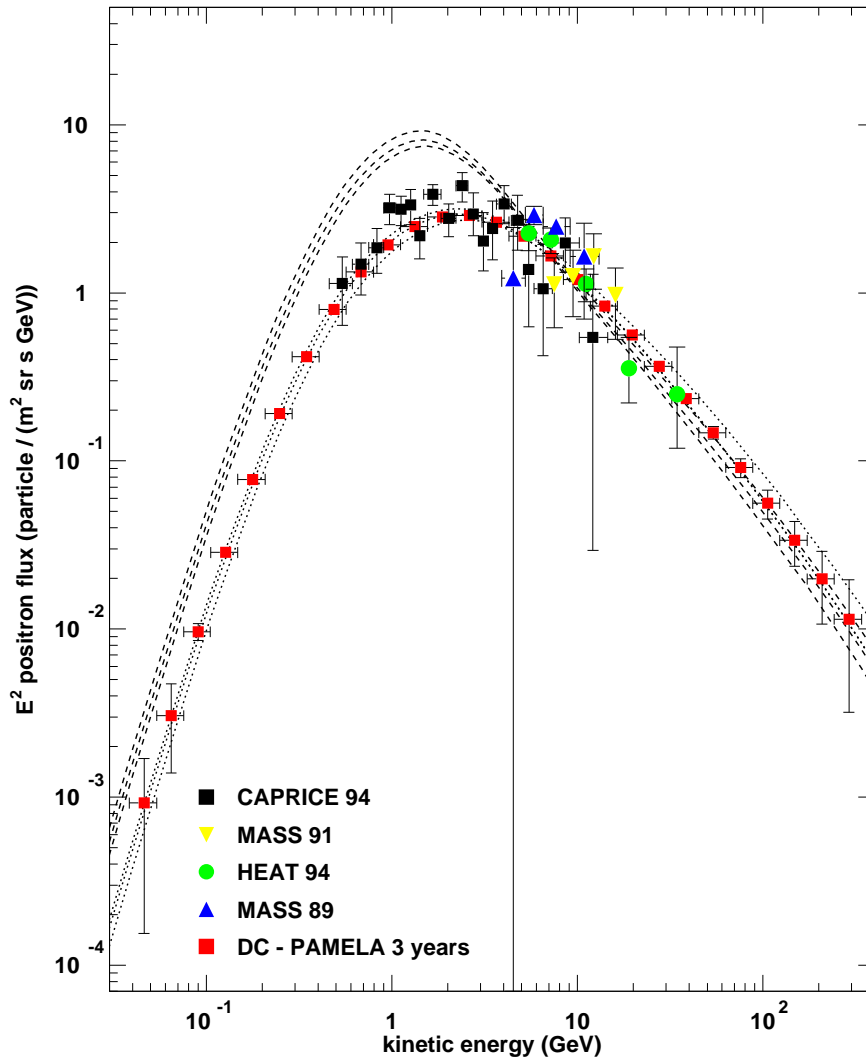


Figure 5.11: Experimental data (from [149]) confronted with PAMELA's expectations for positrons for DC model background. Total uncertainties of positron fluxes with the spectra that correspond to the parameters of the best B/C fit in the middle are given for better confrontation: for DC model are represented with dotted lines while for DRB model with dashed lines. DR and DRB model background PAMELA predictions for positron fluxes are not given because those fluxes are largely overestimating the experimental data at low energies.

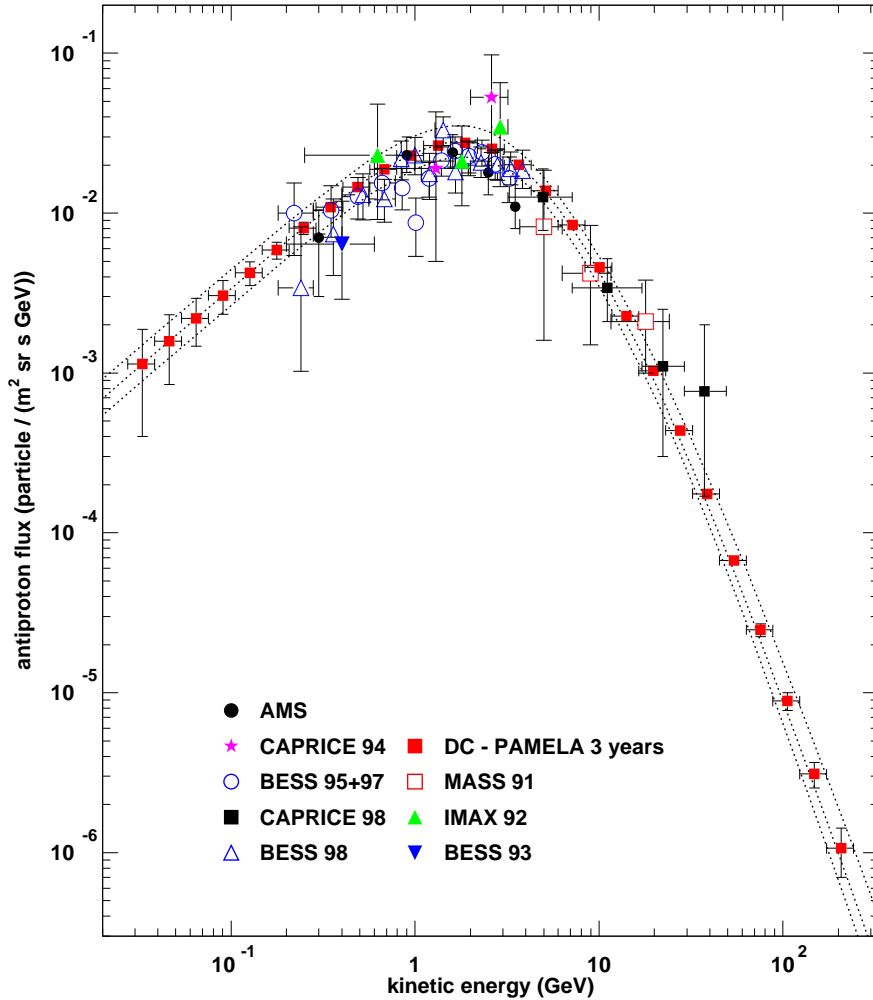


Figure 5.12: Experimental data (from [148]) confronted with PAMELA's expectations for antiprotons for DC model background. Total uncertainty of the DC model antiproton background flux with the spectra that corresponds to the parameters of the best B/C fit in the middle are given for better confrontation; they are represented with dotted lines. The reduced χ^2 is 1.1, what means that just the background fits the experimental data excellent. For better visibility we present in the next figure 5.13 PAMELA's expectations for antiprotons for DRB model. To avoid confusion we don't present PAMELA's expectations for antiprotons for DR model, as DR model flux that correspond to the best B/C fit propagation parameters is almost identical with that of DRB model.

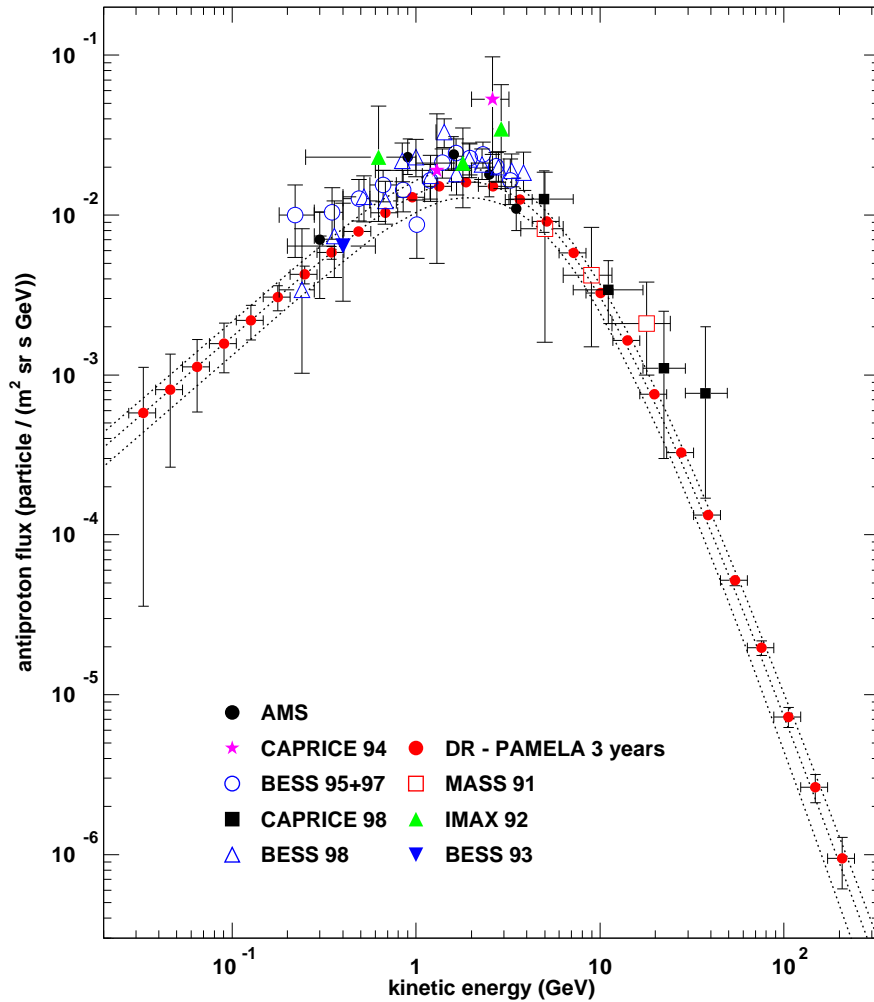


Figure 5.13: Experimental data (from [148]) confronted with PAMELA's expectations for antiprotons for DRB model background. Total uncertainty of the DRB model antiproton background flux with the spectra that corresponds to the parameters of the best B/C fit in the middle are given for better confrontation; they are represented with dotted lines. We don't present PAMELA's expectations for antiprotons for DR model, as DR model flux that correspond to the best B/C fit propagation parameters is almost identical with that of DRB model.

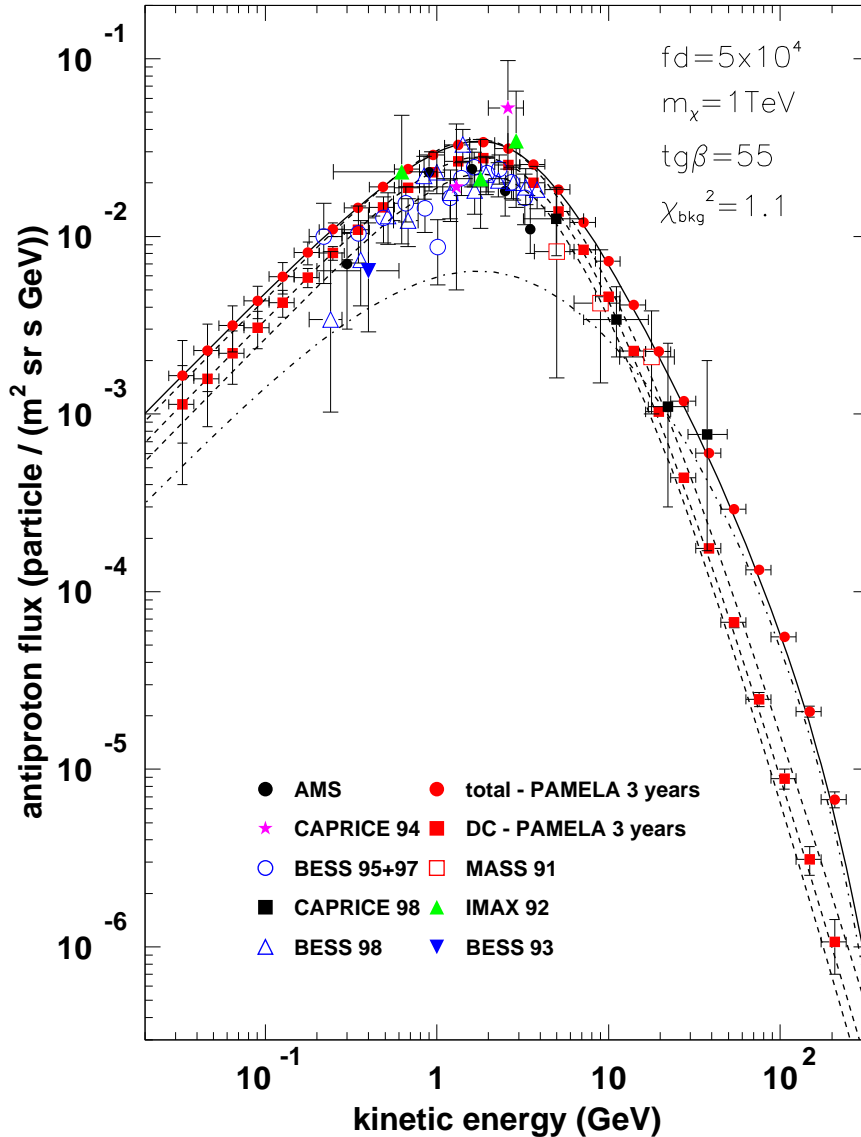


Figure 5.14: Experimental data (from [148]) and PAMELAS’s expectations for DC model background that corresponds to the best B/C data fit propagation parameters (red squares) confronted with PAMELA’s expectations for the total flux (red circles) determined by the same DC model background summed with the third mSUGRA model signal component from figure 4.1. Total uncertainty of the antiproton DC model background flux with the background flux in the middle are given for better confrontation; they are represented with dashed lines. The mSUGRA third model induced component of the total flux is represented with a dashed-dotted line. The total flux is represented with solid line.

5.7 The Possibility of Disentanglement of the Neutralino Induced Component of the Antiproton Flux With PAMELA

In this section we will find the minimal values of the clumpiness factors needed to disentangle a neutralino induced component of the antiproton flux with PAMELA experiment. We computed this factor as a function on the mSUGRA parameter space, fixing A_0 , $\tan\beta$ (we will consider the few most important values) and the sign of μ to $+1$. Like that, the clumpiness factor become a function of m_0 and $m_{1/2}$ parameters. Similar considerations were already made in the literature (see, for example, [122, 140, 139]).

For discrimination we requested the next two conditions:

1. The total antiproton flux $\phi_{tot} = \phi_{bkg} + \phi_{susy}$ gives a good fit of the experimental data.
2. Difference between ϕ_{tot} and DC model ϕ_{bkg} is visible by PAMELA.

The first condition is satisfied if

$$\chi_{fit}^2 = \frac{1}{N-1} \sum_n \frac{(\Phi_n^{exp} - \Phi_n^{tot})^2}{(\sigma_n^{exp})^2} \quad (5.1)$$

is less than the $\chi_{fit,0}^2 = 1.7$, for $N = 40$ experimental points.

The second condition is satisfied if

$$\chi_{discr}^2 = \frac{1}{M-1} \sum_m \frac{(\Phi_m^{bkg} - \Phi_m^{tot})^2}{(\sigma_m^{P,bkg})^2} \quad (5.2)$$

is bigger than the $\chi_{discr,0}^2 = 1.8$, for $M = 29$ points, where $\sigma_m^{P,bkg}$ are the PAMELA statistical errors associated to the background flux (those presented in plot 5.12).

We will note here one more time that the reduced χ_{fit}^2 for the case of just the background flux is $\chi_{fit}^2 = 1.1$, what means that just the background fits the experimental data good.

5.7.1 Results

For each model we found the minimal value of the clumpiness factor fd needed to satisfy the both conditions. As the clumpiness factor is a function of m_0 and $m_{1/2}$ parameters, in order to have a better visualization, we made

a contour plots: equi-clumpiness factors lines are calculated. The calculation is done for the 50 by 50 lattice in the masses. First, we present the "rough" results for different values of $\tan\beta$ in figures 5.15 and 5.16. With black color in all the figures are represented the regions in parameter space that are excluded either by accelerator bounds or because electroweak symmetry breaking is not achieved or because the neutralino is not the lightest supersymmetric particle. Red color indicates the $(m_0, m_{1/2})$ domains with Ωh^2 in the WMAP region $0.09 < \Omega h^2 < 0.13$ (see the first chapter some more details). With green color we represented the parameter space regions with values of $0.13 < \Omega h^2 < 0.3$. Equi-clumpiness factors lines are given with black solid lines; beside every line it is indicated the value of the clumpiness factor. On some plots equi-clumpiness factor $fd = 1$ line is indicated with an arrow for the better visibility. This line is important, because it indicates where in the parameter space is possible to have the conditions from equations 5.1 and 5.2 both satisfied: in fact, under that line there are no models that satisfy the both conditions. As an example for this, we give in figure 5.17, lower pannel, a plot with that region colored in blue for one of the "zooming" we did for some interesting portions of the parameter space that we will soon treat. Sometimes, we give the same plots twice: the repeated plots contain the equi-neutralino mass lines given with black solid lines also; beside every line there is the value of the neutralino mass in GeV.

It can be seen that for disentanglement with PAMELA are sufficient even the relatively small clumpiness factors, maximally of the order of 10. This is very important, because, even if we consider a DC model as the background flux (that alone already fits well the experimental data, in contrast with DR models for the standard propagation that systematically underestimate the data for an order of tens of percents) it is still possible to disentangle the supersymmetric component for a "large portion" of the parameter space (in comparison with the WMAP allowed zone, for example) see 5.15, especially in the case of the $\tan\beta = 55$.

Then, we concentrated to some particularly interested regions found in "rough plots", namely those inside the Cosmologically allowed zone. One of them is for the model with $\tan\beta = 50$ and it is presented in the figure 5.17. We can see that in this case the region in the parameter space that corresponds to the satisfied conditions 5.1 and 5.2 and correct Ω , i.e. the intersection between the red zone and over-the- $fd = 1$ line zone, is not very big with respect to the Cosmologically allowed red zone, but conditions are satisfied in the red zone even without the clumpiness and in the biggest part of the intersection the minimal disentangling clumpiness factors are very small, less than 20.

We can see that in the case of $\tan\beta = 55$ there are the maximally ex-

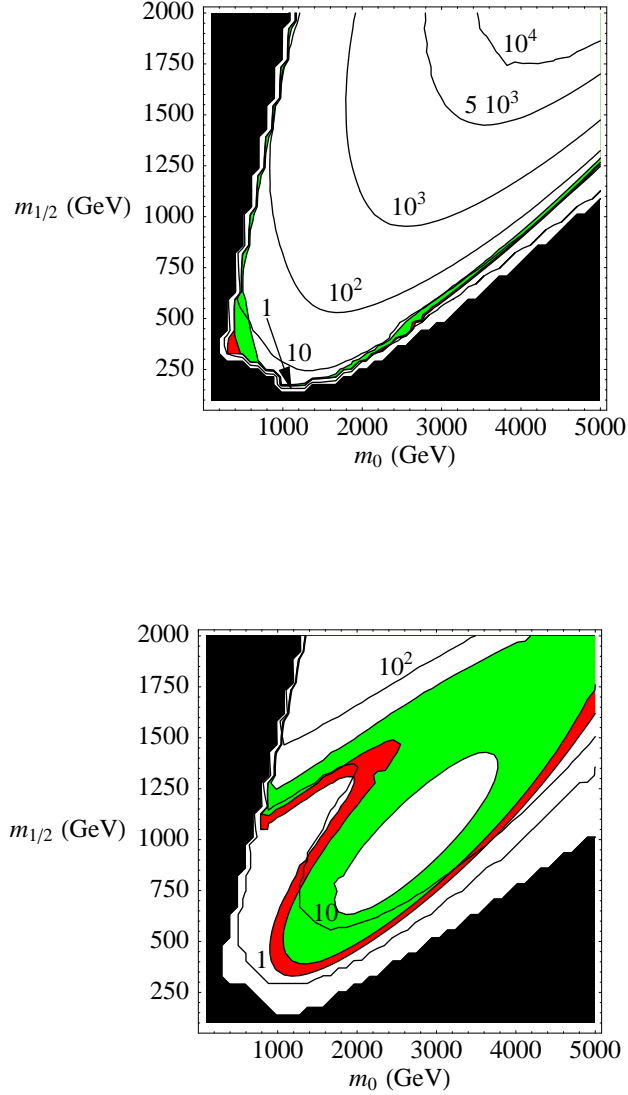


Figure 5.15: The equi-clumpiness factors lines (with the values of the factors beside) as functions on 50×50 lattice in all the considered m_0 and $m_{1/2}$ parameters ("rough plots"). Values of $\tan\beta$ are 50 for the upper plot and 55 for the lower one. With black color are represented the regions in the parameter space that are excluded either by accelerator bounds or because electroweak symmetry breaking is not achieved or because the neutralino is not the lightest supersymmetric particle, red are domains with Ωh^2 in the WMAP region $0.09 < \Omega h^2 < 0.13$, while green are the parameter space domains with $0.13 < \Omega h^2 < 0.3$. Under the line with $fd = 1$ there are no models that satisfy the both conditions.

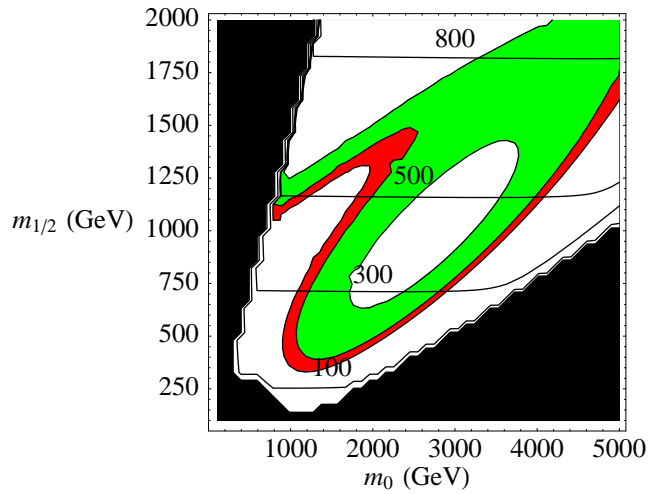
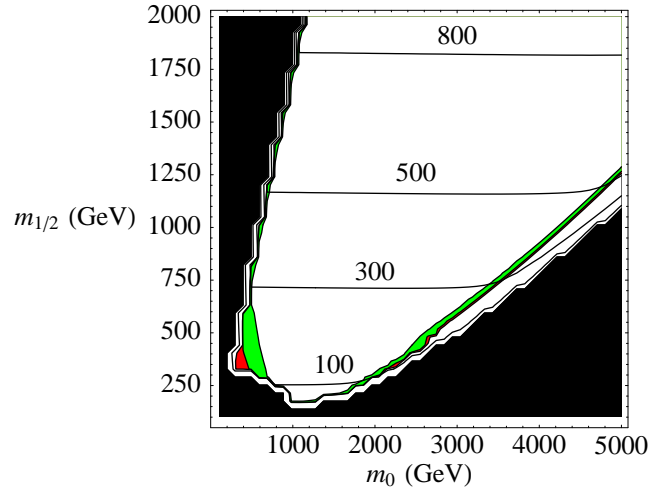


Figure 5.16: The equi-neutralino mass lines (with the values of the masses in GeV beside) as functions on 50×50 lattice in all the considered m_0 and $m_{1/2}$ parameters. Values of $\tan\beta$ are 50 for the upper plot and 55 for the lower one. With black color are represented the regions in the parameter space that are excluded either by accelerator bounds or because electroweak symmetry breaking is not achieved or because the neutralino is not the lightest supersymmetric particle, red are domains with Ωh^2 in the WMAP region $0.09 < \Omega h^2 < 0.13$, while green are the parameter space domains with $0.13 < \Omega h^2 < 0.3$.

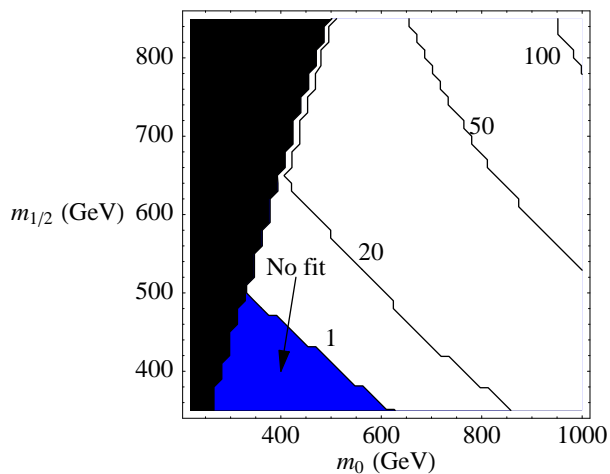
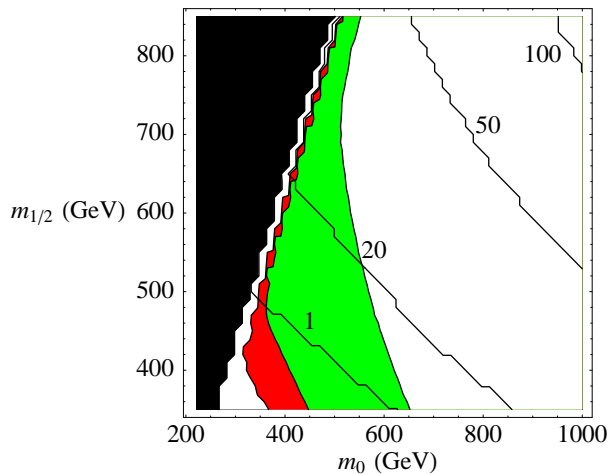


Figure 5.17: Up: The equ-clumpiness factors lines (with the values of the factors) as functions on 50×50 lattice in the most interesting part of the $(m_0, m_{1/2})$ parameter space ("zoomed" on the WMAP allowed zone) for $\tan \beta = 50$. Regions in the parameter space that are excluded either by accelerator bounds or because electroweak symmetry breaking is not achieved or because the neutralino is not the lightest supersymmetric particle are black, domains with Ωh^2 in the WMAP region $0.09 < \Omega h^2 < 0.13$ are red, while green are the regions with $0.13 < \Omega h^2 < 0.3$. Down: the same lattice as in the upper plot, but with blue colored region under the line with $fd = 1$ in which there are no models that satisfy the both conditions 5.1 and 5.2.

tended cosmologically allowed regions. This is achieved without increasing the minimal clumpiness factors needed to disentangle the supersymmetric signal.

To see better the fd factor as the function on the $(m_0, m_{1/2})$ plane (for fixed $\tan\beta$), we present here two three dimensional graphics that correspond to one "rough" plot and to one "zoomed" plot, for details see figure 5.18.

Here, we will give one more case, mass plane for $\tan\beta = 60$ (see figure 5.7.1) in which one red zone is not very big, but it is completely between the lines with $fd = 1$ and $fd = 10$.

So, to repeat one more time the conclusion we deduced in this section: simply said, even for the diffusion plus convection background models that are already fitting the data good, PAMELA will be able to disentangle the eventual supersymmetric signal – and – to do so even for the small clumpiness factors. This is one of the most important conclusions of this thesis.

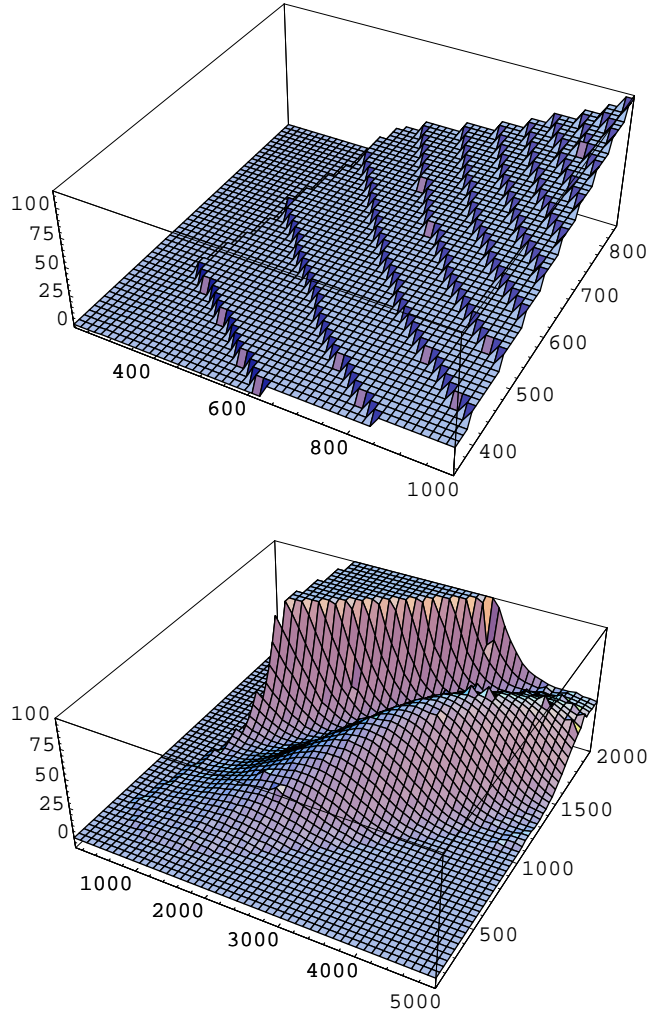


Figure 5.18: Clumpiness factor as a function on the $(m_0, m_{1/2})$ plane (masses are given in GeV) for fixed $\tan \beta = 50$ in the "zoomed" zone from the figure 5.17 (the upper graphic) and for $\tan \beta = 55$ for all the masses we considered, i.e. the hole mass zone from the lower plot from the figure 5.15 (the lower graphic).

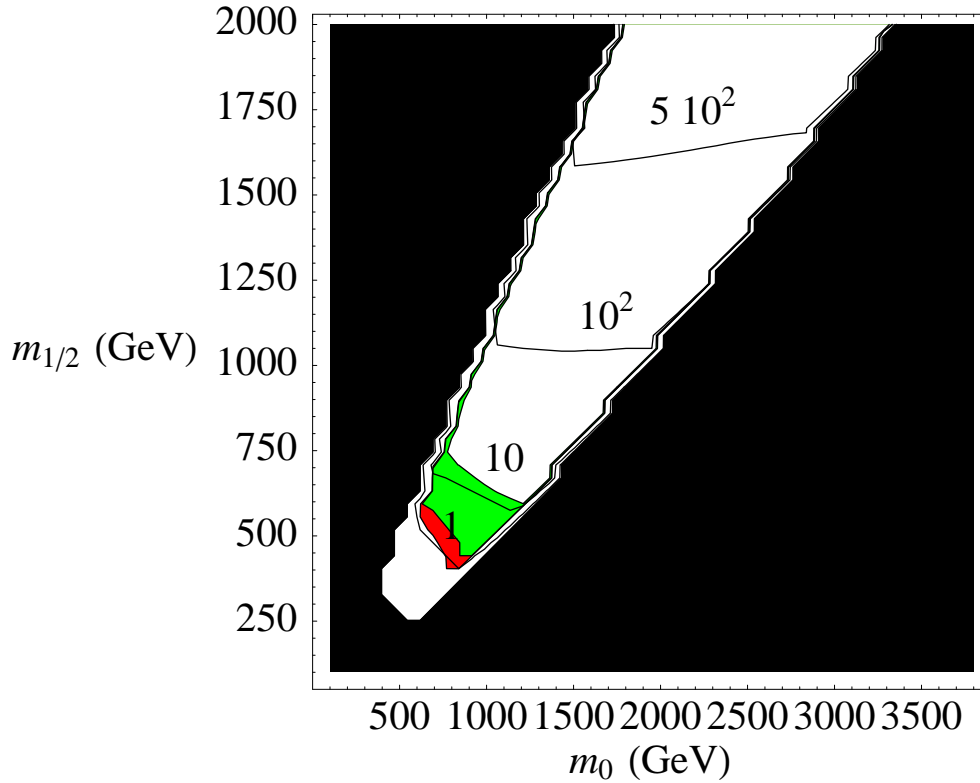


Figure 5.19: The equi-clumpiness factors lines (with the values of the factors beside) as functions on 50×50 lattice in all the considered m_0 and $m_{1/2}$ parameters. The value of $\tan \beta$ is 60. With black color are represented the regions in the parameter space that are excluded either by accelerator bounds or because electroweak symmetry breaking is not achieved or because the neutralino is not the lightest supersymmetric particle, red are domains with Ωh^2 in the WMAP region $0.09 < \Omega h^2 < 0.13$, while green are the parameter space domains with $0.13 < \Omega h^2 < 0.3$. Under the line with $fd = 1$ there are no models that satisfy the both conditions. The Cosmologically allowed (red) zone is not very big, but it is completely between the lines with $fd = 1$ and $fd = 10$.

Chapter 6

Conclusions

In this chapter we will summarize and discuss the main results achieved in this work. In the first part of the thesis we deduced systematically the uncertainties of the most important cosmic rays spectra, with an accent on positrons and antiprotons. For positrons in diffusion reacceleration model, even when the uncertainties are included, the curve of the minimal positron production still remains above the experimental results. Breaking the index of the primary spectra (DRB model) gently improves just the low energy part of the spectra below the maximum, but even the minimal predictions still remain bigger than the experimental results around the maximum (where due to the break now are produced even slightly more positrons) as well as below it. On the other side, this attempt for the improvement of the DR model results slightly affects the best B/C experimental data fit. This break is also not sufficient to match protons and helium, that are still overestimated. In the end, electrons remain largely overproduced at low energies, even more than without the break, i.e. in DR model case.

For the model with diffusion and convection all the results are in excellent agreement with the data, with only some problems with B/C data. Those problems could be, at least partially, due to some other sources of the uncertainties, like the uncertainties in the interstellar gas distribution and Solar modulation or approximations done in the cross sections calculations. As a possibility for the future considerations we would like to emphasize that it is natural to expect models that include both of the processes – convection and reacceleration, and this perhaps can be a key to solve simultaneously problems with positrons, electrons, primaries and B/C. But, we have not yet found such a kind of models using the Galprop code.

In any case, further measurements of antiproton and positron spectra, primary to secondary CR ratios and Solar effects on them, as well as the precise determination of important nuclear cross sections seem to be crucial

for answering the question of the models quality.

The upper uncertainty bands of the antiproton spectra for the models that include reacceleration touch the experimental data from below. In those cases the experimental data fits can be improved easily with many different primary components that are coming from eventual neutralino annihilations (for a large part of the parameter space) or some other exotic contributions.

In the framework of DC model, exotic contributions remain surely possible at high energies ($E > 20\text{GeV}$), and also they are not excluded at lower energies, purely due to the relatively large background uncertainties (at least for now). For the calculation of the component of the antiproton spectra induced by the annihilations of neutralinos in the framework of mSUGRA theory, we made a use of **DarkSUSY** and **ISASUGRA** public codes. As an example, we have shown how some neutralino induced components in the small clumpy halo scenario could give contributions to the total antiproton flux in the case of DC model background and we have calculated the PAMELA predictions for some of them. But, as we will see soon, the more extended treatment in the last chapter shows that also with a DC background flux that corresponds to the best B/C data fit propagation parameters, detection of the supersymmetric components of the antiproton spectra remains still possible in a large part of a parameter space, without violating the quality of the experimental data fit.

In the second part of this thesis we treated the detection of cosmic rays with upcoming PAMELA experiment, particularly antiprotons. The positron and antiproton fluxes statistical errors for various background propagation models were found as well as for some interesting total antiproton fluxes. We studied in details the possibility of detection of supersymmetric part of the antiproton spectra for a large domain in the parameter space of the minimal supergravity model: we divided it in the mass planes for some most interesting values of the $\tan\beta$ parameter. The most important conclusion that we deduced from the results obtained in this part of the thesis is that for the disentanglement with PAMELA instrument of the neutralino induced component of the antiproton spectra in the framework of the mSUGRA theory are sufficient even the relatively small clumpiness factors in the framework of minimal clumpy scenario (clumpiness factors maximally of the order of $fd \propto 10$). This is very important result, especially because we considered a DC model flux as the background. This flux alone already fits well the experimental data, in contrast with DR models for the standard propagation that systematically underestimate the data for an order of tens of percents, and like that allow almost any supersymmetric contribution – it is trivial to improve the data fits of DR models and to detect almost any reasonable signal. So, even if we used DC background, it is still possible to disentangle

the supersymmetric component for a relatively "large" (in the comparison with the WMAP allowed zones) portion of the parameter space. Said in simple words, even for the background models that are already fitting the data good, PAMELA will be capable to disentangle the eventual supersymmetric signal – and – to do so even for the small clumpiness factors. This is one of the most important conclusions of this thesis.

Bibliography

- [1] G. G. Ross, "Grand Unified Theories"
- [2] W. R. Webber and M. S. Potgieter, *ApJ*, 344, 779 (1989)
- [3] J. Kota and J. R. Jokipii, *ApJ*, 265, 573 (1983)
- [4] R. A. Burger and M. S. Potgieter, *ApJ*, 339, 501 (1989)
- [5] J. P. L. Reinecke and M. S. Potgieter, *J. Geophys. Res.*, 99, 14761 (1994)
- [6] B. Moore et al., *ApJ*, 499, L5 (1998)
- [7] G. A. Camelia, in *Frascati Phys. Series*, Vol. XXIV, p79-94 (2002), and many references inside
- [8] Reynolds, R. J. (1989) *ApJ*, 339, L29
- [9] Bronfman, L., et al. (1988) *ApJ*, 324, 248
- [10] Gordon, M. A., & Burton, W. B. 1976, *ApJ*, 208, 346
- [11] Cordes, J. M., et al., (1991) *Nature*, 354, 121
- [12] D. N. Spergel and P. Steinhardt, *Phys. Rev. Lett.*, 84, 3760 (2000)
R. Colin et al., *ApJ* 542, 622 (2000)
P. Bode et al., *ApJ* 556, 93 (2001)
- [13] Cox, P., Krügel, E., & Mezger, P. G. (1986) *A&A*, 155, 380
- [14] D. Bailin, A. Love, *Supersymmetric Gauge Field Theory and String Theory*, Institute of Physics Pub. London, 1994.
M. Blagojević, *Gravitacija i lokalne simetrije*, Institut za fiziku – Beograd, Beograd, 1997.
D. Bailin, A. Love, *Supersymmetric Gauge Field Theory and String Theory*, Institute of Physics Pub. London, 1994.

- P. G. O. Freund, Introduction to Supersymmetry, Cambridge Univ. press, Cambridge, 1985.
- J. P. Elliott, P. G. Dawber, Symmetry in Physics, The Macmillan press LTD. 1979.
- D. S. Freed, Five Lectures on Supersymmetry, Dep. of Math. Univ. of Texas at Austin, preliminary ver.
- M. F. Sonius, Supersymmetry for Beginners, Proc. of the Trieste September 1982. School, World Sc. 1982.
- J. Wess and J. Bagger, "Supersymmetry And Supergravity"
- A. Lionetto, PhD thesis, Universita degli studi Roma 3, 2003.
- A. Cesarini, PhD thesis, Universita degli studi Roma 2, 2004.
- S. J. Gates, M. T. Grisaru, M. Rocek and W. Siegel, "Superspace, Or One Thousand And One Lessons In Supersymmetry, "Front. Phys. **58** (1983) 1, hep-th/010820
- [15] R. N. Mohapatra and G. Senjanovic, Phys. Rev. Lett., 44, 912 (1980)
- [16] S. H. Hansen et al., Mon. Not. Roy. Astron. Soc. 333, 544 (2002)
- [17] J. R. Primack, M. A. K. Gross, in ed. D. O. Caldwell, Current Aspects of Neutrino Physics (Springer, Berlin 2001) p. 287
- [18] K. G. Begeman, A. H. Broelis and R. H. Sanders, Mon. Not. R. Soc. 249, 523 (1991)
- [19] F.W. Stecker, S. Rudaz and T.F. Walsh, *Phys.Rev.Lett.* **35** (1985) 1
- [20] R. Golden et al., *Phys. Rev. Lett.* **43** (1979) 1196; see also R. Golden et al., *Astophys. Journal Lett.*, **24** (1984) 75
- [21] E. Bogomolov et al., *XX Int. Cosmic Ray Conf.*, 2, 72 (1987), Moscow — *XXI Int. Cosmic Ray Conf.*, 3, 288 (1990), Adelaide
- [22] A. Buffington et al., *Astophys. Journal* **248** (1981) 1179
- [23] F.W. Stecker and A.W. Wolfendale, *XIX Int. Cosmic Ray Conf.* OG 6.1-8, 354 (1985) La Jolla
- [24] R.E. Streitmatter et al. *XXI Int. Cosmic Ray Conf.*, 3, 277 (1989), Adelaide
- [25] S.P. Ahlen et al., *Phys. Rev. Lett.* **61** (1988) 145
- [26] I. Moskalenko et al., astro-ph/0210480, to be published in *Astrophysical Journal*, **586** (2003) April 1

- [27] F. Donato et al. *Astrophysical Journal*, **536** (2001) 172
- [28] M.Simon et al. *Astrophysical Journal*, **499** (1998) 250
- [29] A. J. Tilka, *Phys. Rev. Lett.* **63** (1989) 840
- [30] R.L.Golden et al. ; *Astophys. Journal* **287** 1987 622
- [31] D. Müller and K. K. Tang, *Astophys. Journal* **312** (1987) 183
- [32] A. Buffington et al., *Astophys. Journal* **199** (1975) 669
- [33] J.K.Daugherty et al., *Astophys. Journal* **198** (1975) 493
- [34] J.L.Fanselow et al., *Astophys. Journal* **158** (1969) 771
- [35] R. Golden et al., *Nucl. Inst. and Met.* **A306** (1991) 366
- [36] G. Basini et al., *Il Nuovo Cimento* **11C** (1988) 339
- [37] R. Bellotti et al., *Astroparticle Physics* 7 (1997) 219
- [38] M. Bocciolini et al., *Nucl.Phys.* **B32** (1993) 77
— *Nucl. Inst. and Met.* **A333** (1993) 560
- [39] G. Barbiellini et al., *Nucl. Inst. and Met.* **A371** (1992) 169
- [40] D. Bergström et al., *Nucl. Inst. and Met.* **A463** (2001) 161
- [41] S. Orito et al., *Phys. Rev. Lett.* **84** (2000) 1078
- [42] R. Battiston, *Frascati Physics Series* Vol.XXIV (2002) 261
<http://www.roma2.infn.it/inf/aldo/ISSS01.html>
and reference therein
- [43] M. Aguilar et al, *Physics Reports*, **366/6** (2002), 331
- [44] A.S. Beach et al., *Phys. Rev. Lett.* **87** (2001) 271101 [astro-ph/0111094]
- [45] S. W. Barwick et al., *Astophys. Journal* **498** (1998) 779 [astro-ph/9712324]
- [46] D. Bergström et al., *Astophys. Journal* **534** (2000) L177
M. Boezio et al., *Astophys. Journal* **561** (2001) 787
- [47] G. Basini et al., *XXVI Int. Cosmic-Ray Conf.* **4**, 77 (1999) Salt Lake City,
M. Hof et al., *Astophys. Journal* **467** (1996) L33

- [48] M. Boezio et al., *Astrophys. Journal* **487** (1997) 415
- [49] J. Mitchell et al., *Phys. Rev. Lett.* **76** (1996) 3057
- [50] A. S. Beach et al., astro-ph/0111094
- [51] M. Boezio et al., *XXVI Int. Cosmic-Ray Conf.*, OG.1.1.16, (1999) Salt Lake City
- [52] J. Alcaraz et al., *Phys. Lett.* **B461** (1999) 387
- [53] M. Boezio et al., *Astrophys. Journal* **532** (2000) 653
- [54] J. M. Clem et al., *Astrophys. Journal* **464** (1996) 507
- [55] R. Golden et al., *Astrophys. Journal* **457** 1996 L103
- [56] R. Golden et al., *Astrophys. Journal* **436** (1994) 769
- [57] C. Grimani et al, *Astronomy & Astrophysics* **392**, 287-294 (2002)
- [58] S. Coutu et al., Proc. of IDM2002 4th International Workshop on the Identification of Dark Matter, St. William's College York 5 Sept. 2002
- [59] J. Edsjo, Proc. of IDM2002 4th International Workshop on the Identification of Dark Matter, St. William's College York 5 Sept. 2002
- [60] L. Bergström, J. Edsjö and P. Ullio, *Astrophys. Journal* **526** (1999) 215
- [61] T.K. Gaisser and B.G. Mauget, *Phys.Lett.* **30** (1973) 1264
T.K. Gaisser and R.K. Schaefer, *Astrophys. Journal* **394** (1992) 174
M. Simon and U. Heinbach, *Astrophys. Journal* **456** (1996) 519
T. Mitsui et al., *Phys. Lett.* **B389** (1996) 169
- [62] E. Baltz and J. Edsjö, *Phys. Rev.* **D 59** (1999) 023511
- [63] P.Picozza, A.Morselli, 2003. *J. Phys. G: Nucl. Part. Phys.*, 29, 903-911
- [64] P.Spillantini et al., *Il Nuovo Cimento* **103B** (1989) 625
- [65] G.Basini et al., *Il Nuovo Cimento* **105B** (1990) 779
- [66] Chandrasekhar, S. 1943, *Rev. Mod. Phys.*, 15, 1.
- [67] Jones, F. C. 1990, *ApJ*, 361, 162.
- [68] G. R. Blumental, S. M. Faber, J. Primack and M. J. Rees, *Nature*, 311, 517 (1984)

- [69] P. J. E. Peebles, *The Astrophysical Journal*, 263, L1 (1982)
- [70] G. Jungman, M. Kamionkowski and K. Griest, *Phys. Rep.*, 267, 195(1996)
- [71] P. J. Steinhardt, *Phys. Scripta*, 185, 177, (2000)
- [72] C. L. Bennet et al., astro-ph/0302207
D. N. Spergel et al., astro-ph/0302209
- [73] P. de Bernardis *et al.*, *Astrophys. J.* **564** (2002) 559; astro-ph/0105296
- [74] S. P. Martin, "A supersymmetry primer," hep-ph/9709356
- [75] H. E. Haber and G. L. Kane, *Phys. Rept.* **117** (1985) 75.
- [76] S. Dimopoulos and D. W. Sutter, *Nucl. Phys. B* **452** (1995) 496
- [77] F. Gabbiani, E. Gabrielli, A. Masiero and L. Silvestrini, *Nucl. Phys. B* **477** (1996) 321
- [78] G. F. Giudice and A. Masiero, *Phys. Lett. B* **206** (1988) 480.
- [79] J. A. Casas and C. Munoz, *Phys. Lett. B* **306** (1993) 288
- [80] G. R. Dvali, G. F. Giudice and A. Pomarol, *Nucl. Phys. B* **478** (1996) 31
- [81] D. Bond and G. Efstathiou, astro-ph/9807103
- [82] S. Weinberg, astro-ph/0006276
- [83] X. Griffith and A. Melchiorri, astro-ph/0011147
- [84] W. Hu and A. Dodelson, astro-ph/0110414
- [85] K. Griest and D. Seckel, *Nucl. Phys. B* **283** (1987) 681
- [86] B. S. Milić, "Osnove fizike gasne plazme", (Gradjevinska knjiga, Beograd, 1989)
- [87] J. Primack, in *Frascati Phys. Series*, Vol. XXIV, p449-474 (2002)
- [88] W. Freedman, in "David Schramm Memorial Volume", *Phys. Rep.*, astro-ph/9909076 (2000)
- [89] S. Weinberg, *Gravitation and Cosmology*, (1981)

- [90] P. de Bernardis, in Frascati Phys. Series, Vol. XXIV, p433-447 (2002)
- [91] M. S. Turner, Phys. Rep., 198, 1 (1990)
S. Weinberg, Phys. Rev. Lett., 40, 223(1978)
E. Masso, hep-ph/0209132
- [92] K. van Bibber et al. preprint UCRL-JC-118357 (1994), 198, 1 (1990)
S. J. Asztalos et al., astro-ph/0104200
- [93] Berezhinskii, V. S., Bulanov, S. V., Dogiel, V. A., Ginzburg, V. L.,
Ptuskin, V. S. 1990, Astrophysics of Cosmic Rays (North Holland,
Amsterdam)
- [94] D. N. Schramm and M. S. Turner, Rev. Mod. Phys., 70, 303 (1978)
- [95] R. A. Swaters, B. F. Madore and M. Trewhella, The Astrophysical
Journal, 531, L107 (2000)
- [96] E. W. Kolb and M. S. Turner, The Early Universe (Addison-Wesley,
1990)
- [97] Fukugita et al., The Astrophysical Journal, 503, 518 (1998)
- [98] Strong, A. W., Moskalenko, I. V., 1998, ApJ, 509, 212
- [99] Fermi, E., 1949, Phys. Rev., 75, 1169
- [100] Seo, E. S., Ptuskin, V. S., 1994, ApJ, 431, 705
- [101] Zirakashvili, V. N., Breitschwerdt, D., Ptuskin, V. S., Volk, H. J., 1996,
A&A, 311, 113
- [102] Blandford, R. D. & Ostriker, J. P. (1980) ApJ, 237, 793
- [103] Moskalenko, I. V., Strong, A. W., Ormes, J. F., Potgieter, M. S., 2002,
ApJ, 565, 280
- [104] U. Heinbach, M. Simon, 1995, ApJ, 441, 209-221
- [105] A. W. Strong and I. V. Moskalenko, "Galprop C++ v.41: Explanatory
supplement", available on the WWW
- [106] Ellison, D. C., Slane, P., Gaensler, B. M., astro-ph/0106257
- [107] Strong, A. W., Mattox, J. R., 1996, 308, L21
- [108] Gleeson, L. J., Axford, W. I., 1996, ApJ, 154, 1011

- [109] Perko, J. S., 1987, *A&A*, 184, 119
- [110] Bieber, J. W., Burger, R. A., Engel, R., Gaisser, T. K., Roesler, S., Stanev, T., 1999. *Phys. Rev. Lett.*, 83, 674
- [111] O. Adriani et al., *Nucl. Inst. and Meth. in Phys. Research A*, 478 (2002) 114-118
- [112] P. Papini, PAMELA Simulations
- [113] Picozza, P., Morselli A., 2003. *J. Phys. G: Nucl. Part. Phys.*, 29, 903-911
- [114] Tan, L. C., Ng, L. K., 1983, *J. Phys. G*, 9, 227
- [115] Tan, L. C., Ng, L. K., 1983, *J. Phys. G*, 9, 1289
- [116] Tan, L. C., Ng, L. K., 1983, *The Astrophysical Journal*, 269, 751-764
- [117] Gaisser, T. K., Schaefer, R. K., 1992, *ApJ*, 394, 174
- [118] Jokipii, J. R. 1971, *Rev. Geo. & Space Phys.*, 9, 27
- [119] P. Gondolo, J. Edsjö, P. Ullio, L. Bergström, M. Schelke and E.A. Baltz, proceedings of idm2002, York, England, September 2002, astro-ph/0211238; <http://www.physto.se/~edsjo/darksusy/>.
- [120] J. Edsjo, M. Schelke, P. Ullio and P. Gondolo, *JCAP* **0304** (2003) 001
- [121] L. Bergström and P. Ullio, *Nucl. Phys.* **B504** (1997) 27; P. Ullio and L. Bergström, *Phys. Rev.* **D57** (1998) 1962.
- [122] S. Profumo and P. Ullio, astro-ph/0406018
- [123] A. Barrau, G. Boudoul, F. Donato, D. Maurin, P. Salati, R. Taillet, astro-ph/0112486; P. Ullio, H. Zhao and M. Kamionkowski, *Phys. Rev. D* **64** (2001) 043504.
- [124] S. Bhattacharyya and Pratibha Pal, 1986, *Il Nuovo Cimento*, Vol 9C, N5, page 961
- [125] Coswik, R. and Gaisser, T. K., 1981, 1992, *Proc. of 17th International Cosmic Rays Conference (Paris)*, 2, 218
- [126] Gaisser, T. K., Ovens. A. J. and Steigman, G., 1981, —AU Symposium 94, *Origin of Cosmic Rays*, ed. G. Setti, C. Spada and A. Wolfendale (Dordrecht: Reidel), p. 257

- [127] Protheroe, R. J., 1981, *The Astrophysical Journal*, 251, 387
- [128] Stephens, S. A., Proc. of 17th International Cosmic Rays Conference (Paris), 9, 199
- [129] Gaisser, T. K., *Cosmic Rays and Particle Physics*, (Cambridge University Press, Cambridge, 1990.)
- [130] L. J. Hall, J. Lykken and S. Weinberg, *Phys. Rev. D* **27** (1983) 2359
- [131] A. Cesarini, F. Fucito, A. Lionetto, A. Morselli and P. Ullio, *Astropart. Phys.* **21** (2004) 267, astro-ph/0305075
- [132] H. Baer, F. E. Paige, S. D. Protopopescu and X. Tata, hep-ph/0001086. The source code is available at <ftp://ftp.phy.bnl.gov/pub/isajet>
- [133] L. Bergstrom, J. Edsjo, P. Gondolo and P. Ullio, *Phys. Rev. D* **59** (1999) 043506, astro-ph/9806072
- [134] L. Bergstrom, J. Edsjo and P. Ullio, astro-ph/9902012.
- [135] J.F. Navarro, C.S. Frenk and S.D.M. White, *ApJ*, **462** (1996) 563.
- [136] P. Gondolo, J. Edsjo, P. Ullio, L. Bergstrom, M. Schelke and E. A. Baltz, *JCAP* **0407** (2004) 008 [arXiv:astro-ph/0406204], “Dark-SUSY: Computing supersymmetric dark matter properties numerically”
- [137] V. L. Ginzburg and S. I. Syrovatskii, *The Origine of Cosmic Rays*, (Pergamon, Oxford, 1964.)
- [138] Rasmussen, I. L. and Peters, B., 1975, *Nature*, 258, 412
- [139] W. de Boer et al., IEKP-KA/2003-17
- [140] A. Bottino et al., astro-ph/0306207; astro-ph/9804137;
- [141] J. L. Feng, K. T. Matchev and F. Wilczek, *Phys. Rev. D* **63** (2001) 045024.
- [142] A. Bottino, F. Donato, N. Fornengo and S. Scopel, *Phys. Rev.* **D63** (2001) 125003.
- [143] J. Ellis, J. L. Feng, A. Ferstl, K. T. Matchev and K. A. Olive, *Eur. Phys. J.* **C24** (2002) 311-322

- [144] J. Ellis, A. Ferstl and K. A. Olive, Phys. Lett. **B532** (2002) 318.
- [145] V. Bertin, E. Nezri and J. Orloff, Eur. Phys. J. **C26** (2002) 111.
- [146] U. Chattopadhyay, A. Corsetti and P. Nath, hep-ph/0303201.
- [147] B/C ratio: ACE: A. J. Davis et al., 2000, AIP Conf. Proc. 528, ed. R. A. Mewaldt et al. (AIP, New York); Ulysses: Du Vernois, M. A. et al., 1996, A&A, 316, 555; Voyager: A. Lukasiak et al., 1999, Proc. 26th Int. Cosmic-Ray Conf. (Salt Lake City), 3, 41; HEAO 3: Engelmann, J. J. et al., 1990, A&A, 233, 96; Caldwell, J. H., Meyer, P., 1977, Proc. 15th Int. Cosmic-Ray Conf. (Plovdiv), 1, 243; Dwyer, R. 1978, ApJ, 224, 691; Juliusson, E. 1974, ApJ, 191, 331; Simon, M., et al. 1980, ApJ, 239, 712
- [148] Antiproton spectra: CAPRICE '98: M. Boezio et al., Astrophys. Journ. 561 (2001) 787; BESS '95 and '97: S. Orito et al., Phys. Rev. Lett. 84 (2000) 1078; BESS '98: T. Maeno et al., Astroparticle Physics 16 (2001) 121-128; CAPRICE '94: M. Boezio et al., Astrophys. Journ. 487 (1997) 415; BESS '93: A. Moiseev et al., Astrophys. Journ. 474 (1997) 479; IMAX '92: J.W. Mitchell et al., Phys. Rev. Lett. 76 (1996) 3057; MASS '91: G. Basini et al., Proc. 26th ICRC (1999) OG.1.1.21
- [149] Positron and Electron spectra: CAPRICE '94: Boezio M. et al. 2000, ApJ 532, 653; HEAT '94: Barwick S. et al. 1997, ApJ 498, 779; MASS 91: C. Grimani et al. 2002, A&A 392, 287-294; MASS '89: R. L. Golden 1994, ApJ 436, 769-775
- [150] Proton and helium spectra: CAPRICE '98: M. Boezio et al., Astroparticle Physics, 19, (2003) 583-604; CAPRICE '94: M. Boezio et al., ApJ, 518:457-472 (1999); BESS: T. Sanuki et al. (2000) ApJ, 545, 1135
- [151] subFe/Fe ratio: ACE: A. J. Davis et al. (2000) On the low energy decrease in Galactic cosmic ray Proc ACE-2000 Symp., editors R. A. Mewald et al. (NY: AIP), AIP Conf. Proc. 528, 421-424, 2000; HEAO-3: W. R. Binns et al., ApJ 324, 1106-1117, 1988 and J. J. Engelmann et al., A&A 233, 96-111, 1990; Sanriku experiment: M. Hareyama et al., 26th ICRC (Salt Lake City) 3, 105-108, 1999
- [152] Lukasiak, A., Ferrando, P., McDonald F. B., & Webber, W. R. 1994a, ApJ, 423, 426
- [153] Lukasiak, A., Ferrando, P., McDonald F. B., & Webber, W. R. 1994b, ApJ, 426, 366

- [154] Phillipps, S., et al. 1981, A&A, 103, 405
- [155] Longair M. S., (1992) High Energy Astrophysics, voll1,2, Cambridge University Press, Cambridge, 1997, revised edition
- [156] Case, G., & Bhattacharya, D. 1996, A&AS, 120C, 437
- [157] Press, W. H. et al. 1992, Numerical Recipes in FORTRAN, 2nd Edition (Cambridge: Cambridge University Press)
- [158] Grevesse, N., Noels, A. & Sauval A. J. 1996, in ASP Conf. Ser 99, Cosmic Abundances, ed. S. S. Holt & G. Sonneborn (San Francisco: ASP), 117
- [159] Hernandez, F. P., & Christensen-Dalsgaard, J. 1994, MNRAS, 269, 475
- [160] K. Hagiwara et al., Phys. Rev. **D66** (2002) 010001.
- [161] G. Boella et al., Modulated Antiproton Fluxes for Interstellar Production Models
- [162] V. L. Ginzburg and V. S. Ptuskin, 1976, Rev. Mod. Phys., 48, 161
- [163] Protheroe, R. J. and Ormes, J. F., 1981, The Astrophysical Journal, 2, 362
- [164] Protheroe, R. J., Ormes, J. F. and Comstock, G. M., 1983, The Astrophysical Journal, 272, 756
- [165] Webbe, W. R. and Potgieter, M. S., 1989, The Astrophysical Journal, 344, 779
- [166] Garcia-Munoz, M., Simpson, M., Guzik, J. A., Wefel, J. P. and Mag-nolis, S. H., 1987, ApJS, 64, 269
- [167] Maurin, D., Taillet, R., & Donato, F. 2002, A&A, 394, 1039 astro-ph/0206286
- [168] Maurin, D., Taillet, R., Donato, F., Salati, P., Barrau, A. and Boudoul, G., astro-ph/0212111 v1
- [169] G. L. Case and S. Bhattacharyya, 1998, The Astrophysical Journal, 504, 761
- [170] M. Simon, U. Heinbach and C. Koch, 1987, ApJ, 320, 699

- [171] T. K. Geisser and E. H. Levy, 1974, Phys. Rev. D, 10, 1731
- [172] D. B. Melrose, Plasma Astrophysics, vol 2, Gordon and Breach Science Publishers, London
- [173] L. A. Fisk, J. Geophys. Res., 76, 221 (1971); L. A. Fisk et al., J. Geophys. Res., 74, 4973 (1969)
- [174] R. D. Zwickl and W. R. Webber, Sol. Phys., 54, 457 (1977)